

**EVALUATION OF IMPULSE RESPONSE &  
GROUND-PENETRATING RADAR AS A  
MEANS OF NON-DESTRUCTIVE TESTING  
OF CONCRETE BRIDGE DECKS**

by

Daniel Jay Clem

A thesis submitted to the Faculty of the University of Delaware in partial  
fulfillment of the requirements for the degree of Master of Civil Engineering

Winter 2013

© 2013 Daniel Jay Clem  
All Rights Reserved

**EVALUATION OF IMPULSE RESPONSE &  
GROUND-PENETRATING RADAR AS A  
MEANS OF NON-DESTRUCTIVE TESTING  
OF CONCRETE BRIDGE DECKS**

by

Daniel Jay Clem

Approved: \_\_\_\_\_  
Thomas Schumacher, Ph.D., P.E.  
Professor in charge of thesis on behalf of the Advisory Committee

Approved: \_\_\_\_\_  
Harry W. Shenton III, Ph.D.  
Chair of the Department of Civil and Environmental Engineering

Approved: \_\_\_\_\_  
Babatunde A. Ogunnaike, Ph.D.  
Interim Dean of the College of Engineering

Approved: \_\_\_\_\_  
Charles G. Riordan, Ph.D.  
Vice Provost for Graduate and Professional Education

## **ACKNOWLEDGMENTS**

There are many people who deserve acknowledgement for their valuable assistance. I would first like to personally thank my advisor, Dr. Thomas Schumacher for bringing me to the University of Delaware. His support and generosity have made this wonderful experience possible.

Dr. John Popovics and his students also deserves acknowledgement for their contributions involving the Impulse Response simulations.

I would like to thank Cherry, Weber & Associates and Advanced Infrastructure Design Inc., who granted the University of Delaware research group access to the Branchport Bridge deck through a full bridge closure. I would also like to thank the following students assisted with collecting of field and laboratory data: Benjamin Berwick, Lassaad Mhamdi, Kaitlyn Gisona, and Tayler Wennick.

The financial support for this research work by the Delaware Department of Transportation (DelDOT) and the University of Delaware is also greatly appreciated.

## TABLE OF CONTENTS

LIST OF TABLES .....	vii
LIST OF FIGURES .....	viii
ABSTRACT .....	xi

### Chapter

1	INTRODUCTION .....	1
2	IMPULSE RESPONSE .....	5
2.1	Background .....	5
2.1.1	Current Practice .....	8
2.1.2	Equipment .....	9
2.1.2.1	Response Transducer .....	11
2.2	Field Tests .....	13
2.2.1	Branchport Bridge .....	13
2.2.2	Del-DOT Bridge 1-245 .....	18
2.3	Numerical Simulations .....	22
2.4	New Procedure .....	27
2.5	Discussion .....	34
3	GROUND-PENETRATING RADAR .....	35
3.1	Background .....	35
3.1.1	Current Practice .....	37
3.1.1.1	Issues .....	42
3.2	Equipment .....	43
3.2.1	Surface Wave .....	44
3.2.2	Scan Angle .....	45



3.2.3	Pulse Wave .....	48
3.3	Isolated Parameter Tests.....	51
3.3.1	Reinforcing Bar Size .....	51
3.3.2	Reinforcing Bar Depth .....	54
3.3.3	Delamination Identification.....	57
3.4	Proposed Additional Post-Processing Procedures.....	59
3.4.1	Non-Linear Time-to-Depth Relationship .....	60
3.4.2	Migration Algorithm .....	62
3.4.3	Cross-Correlation Algorithm.....	64
3.5	Bridge Deck Specimen Tests.....	66
3.5.1	Delaminations.....	66
3.5.2	Slab Thickness.....	69
3.6	Discussion.....	74
4	CONCLUSION .....	76
	REFERENCES .....	78
Appendix		
A	IMPULSE RESPONSE FIELD TEST CONTOUR PLOTS.....	80
A.1	Branchport Bridge .....	80
A.1.1	Deck #1.....	80
A.1.2	Deck #2.....	84
A.1.3	Deck #3.....	88
A.1.4	Deck #5.....	92
A.2	Del-DOT Bridge 1-245.....	96
A.2.1	Section #1 (0'-60') .....	96
A.2.2	Section #3 (120'-208') .....	98
B	MATLAB SCRIPTS .....	100
B.1	Impulse Response Scripts.....	100

B.1.1	Acceleration.....	100
B.1.2	Force .....	102
B.1.3	Mobility at a Specific Test Point .....	104
B.1.4	System Response at Specific Test Point.....	105
B.1.5	Mobility Over the Entire Bridge.....	106
B.1.6	System Response Over the Entire Bridge .....	107
B.1.7	Average Mobility.....	108
B.1.8	Dynamic Stiffness .....	109
B.1.9	Mobility Slope .....	111
B.1.10	Peak Mean Mobility .....	112
B.1.11	Maximum System Response .....	113
B.1.12	Peak Finder .....	114
B.1.13	System Response Damping .....	115
B.2	Ground-Penetrating Radar Scripts.....	116
B.2.1	Data Extraction.....	116
B.2.2	Attenuation .....	117
B.2.3	Cross-correlation Algorithm.....	118
B.2.4	Migration Algorithm .....	119
C	PERMISSION LETTER FOR FIGURE 1.1 .....	120

## **LIST OF TABLES**

Table 3.1	Relative Dielectric Constants of Civil Materials.....	36
Table 3.2	Actual, Linearly Calculated, and Non-Linearly Calculated Clear Cover. ....	62

## LIST OF FIGURES

Figure 1.1:	Sounding and Chain-drag Equipment (photo by Ralf Arndt).....	2
Figure 2.1	Impulse Response Testing Procedure.....	6
Figure 2.2	Example Mobility Spectrum (black line) and Analysis Parameters According to ASTM Standard C1740-10.....	8
Figure 2.3	Example of IR Equipment Being Used in the Field.....	10
Figure 2.4	Mobility of Laboratory Specimen with the Response Measured by an Accelerometer and a Geophone, simultaneously. ....	11
Figure 2.5	Cross-section of the Branchport Bridge. ....	13
Figure 2.6	Plan View of Branchport Bridge; Decks 1 through 6 (left to right).....	14
Figure 2.7	IR Parameters of the Branchport Bridge, Deck 4; ASTM Standard C1740-10 (a) Average Mobility, (b) Dynamic Stiffness, (c) Mobility Slope, (d) Peak Mean Ratio.....	15
Figure 2.8	Cross-section of Del-DOT Bridge 1-245 .....	19
Figure 2.9	IR Parameters of the Del-DOT 1-245 Bridge; ASTM Standard C1740- 10 (a) Average Mobility, (b) Dynamic Stiffness, (c) Mobility Slope, (d) Peak Mean Ratio.....	20
Figure 2.10	Illustration of ABAQUS FE Model: (a) Delamination Centered Above a Girder, (b) Delamination Centered Between Two Girders. IR Testing Point, Indicated by Green Arrow, is Applied at Center of Delamination Width. ....	22
Figure 2.11	Force Recorded in Field Experiment and Forcing Function used in FE Simulation: (a) Time Domain, (b) Frequency Domain. ....	23
Figure 2.12	Mobility of FE Simulated Solid Sections and Sections with Delaminations of $a = 300$ mm, 400 mm, 600 mm, and 1,200 mm Width (directly above the girder) .....	24

Figure 2.13	Mobility of a FE Simulated Solid, and $a = 600$ mm and 1,200 mm Wide Delamination, Both Above Girder and Mid-span Between Girders. ....	25
Figure 2.14	ASTM Standard Parameters Plotted as a Function of the Delamination Width, a (a) <i>Average Mobility</i> , (b) <i>Dynamic Stiffness</i> , (c) <i>Mobility Slope</i> , (d) <i>Peak Mean Mobility Ratio</i> . ....	27
Figure 2.15	New Suggested Impulse Response Testing Procedure.....	28
Figure 2.16	Possible Parameters for the New IR Procedure.....	30
Figure 2.17	New IR Parameters of the Branchport Bridge, Deck 4: (a) Maximum System Response, (b) System Response Damping. ....	32
Figure 3.1	Typical Post-Processing Procedure for GPR Data. ....	38
Figure 3.2	Sketch of a Lab Specimen Tested with GPR. ....	40
Figure 3.3	Typical GPR A-Scan. ....	41
Figure 3.4	Typical GPR B-Scan. ....	41
Figure 3.5	Device used in this Study. ....	43
Figure 3.6	Average Concrete Surface Wave Signal. ....	45
Figure 3.7	Sketch of Scan Angle both Parallel ( $\alpha$ ) and Perpendicular ( $\beta$ ) to the Path. ....	46
Figure 3.8	B-Scan for Parallel Scan Angle ( $\alpha$ ) Test (Case A). ....	46
Figure 3.9	Average A-Scan for Perpendicular Scan Angle ( $\beta$ ) with Varying Distance from Bar (Case B). ....	48
Figure 3.10	Setup for Pulse Test.....	49
Figure 3.11	Recorded Pulse Reflection and Assumed Pulse Waveform. ....	50
Figure 3.12	Reinforced Concrete Specimen. ....	51
Figure 3.13	B-Scan of Reinforcing Bars with Varying Diameters. ....	52
Figure 3.14	Sketch of the Travel Path of the Pulse. ....	53

Figure 3.15	Idealized B-Scan of Reinforcing Bar and Bar Diameter. ....	54
Figure 3.16	B-Scan of Reinforcing Bars with Varying Clear Covers. ....	55
Figure 3.17	Percent Error with Varying Depths. ....	56
Figure 3.18	B-Scans for Delamination Tests 1 through 6. ....	58
Figure 3.19	Post-Processing Procedures for GPR Data Developed in this Study (red). ....	59
Figure 3.20	Sketch of Assumed Pulse Wave Path for Linear (dotted line) and non- linear (solid line) Relationship. ....	60
Figure 3.21	Sketch of Migration Algorithm. ....	64
Figure 3.22	Delaminated Section (a) Sketch and (b) Traditionally Processed B- Scan Using the Linear Time-Depth Relationship. ....	67
Figure 3.23	B-Scan Data Post-Processed with Cross-Correlation Procedure Using the Non-Linear Time-Depth Relationship. ....	68
Figure 3.24	Plan View of Specimen Scanned. ....	69
Figure 3.25	Traditional B-Scan of Slabs with Linearly Varying Thickness (top) and Thickness Varying in Steps (bottom). ....	70
Figure 3.26	Cross-Correlation Procedure of B-Scan Data of Slabs with Linearly Varying Thickness (top) and Thickness Varying in Steps (bottom). ....	72

## **ABSTRACT**

Nationwide, a significant percentage of decks of reinforced and prestressed concrete bridges are exposed, not only to a growing traffic volume, but also to an increasingly aggressive environment. These conditions can lead to shallow delamination within the deck. Once large portions of the deck are delaminated, the function of the deck as integral part of the structure may become questionable. So far, transportation agencies have used simple visual inspection methods, which are often subjective and qualitative, to locate deteriorated areas for repair. These methods give only a rough estimate of the location of the actual deterioration and give no information about the depth of the delamination. In this thesis the effectiveness of two methods of non-destructive testing and their ability to predict the depth and extent of shallow delaminations in concrete bridge decks are discussed. Current practice of Impulse Response and Ground-Penetrating Radar testing is reviewed, performed (either in the field or in the lab), and evaluated. Modifications to these practices are suggested to customize each method specifically to delamination testing. If used properly, these new test procedures may help bridge owners to more accurately estimate delaminations and their depths which will help to better predict rehabilitation costs.

## **Chapter 1**

### **INTRODUCTION**

As our infrastructure continues to age we are becoming more dependent on rapid non-invasive in-situ evaluation and rehabilitation<sup>1</sup>. This holds especially true for reinforced concrete bridge decks, which are exposed, not only to a growing traffic volume, but also to an increasingly aggressive environment. Inaccurate or missing as-built drawings can make evaluating these decks difficult. In addition to that, deicing chemicals, used to keep the roads free of ice in the winter, can combine with rain and penetrate the concrete through micro-cracks where they can reach the reinforcing steel<sup>2</sup>. Once that has occurred, the reinforcing steel starts corroding which leads to an expansion of the steel, which in turn can lead to extensive concrete cracking and eventually spalling. The coalescence and formation of a crack parallel to the surface is known as delamination<sup>3</sup>. Additionally, fatigue of concrete has been found to lead to delaminations without steel rebar corrosion<sup>4</sup>. Once large portions of the deck are delaminated, the function of the deck as integral part of the structure may become questionable.

Delaminations occur beneath the surface, and often give no indication to outside observers of their presence. This makes locating the areas with these flaws difficult. There are two visual methods typically used by departments of transportation to identify and locate delaminations. These are illustrated in Figure 1.1.

One is a method called ‘sounding’. This method involves an experienced operator striking the surface of the bridge deck with a hammer. Based on experience



the operator can distinguish between the sound of a solid section and a delaminated section. The other method is chain drag. In this method a set of standard steel chains are dragged across the surface of the deck. Again an experienced operator can distinguish between the sound of a solid section and a delaminated section. Both of these methods are time intensive and require relative silence to be able to perform. These methods are also subjective and their effectiveness is dependent on the operator. These methods also only evaluate the extents of the damage, but they give no indication of the depth of the cracking.



Figure 1.1: Sounding and Chain-drag Equipment (photo by Ralf Arndt).

A more effective, non-destructive method of quickly, objectively, and effectively evaluating as-built conditions and deterioration in concrete bridge decks is desired. Estimating the area and depth of delaminations are of particular interest. There are many methods of Non-destructive Testing (NDT) for concrete structures and they vary in effectiveness and commercial availability.

One method of NDT of concrete bridge decks discussed is Impulse Response (IR). This method was developed in the aviation industry<sup>5</sup>, then was applied to deep piles, and now is used on concrete plate like structures<sup>6</sup>. IR analyzes the response of the deck to a hammer strike to determine extents of the delaminations.

The other method evaluated is Ground-Penetrating Radar (GPR). This method uses the time-of-flight of electric-magnetic waves as they penetrate and reflect within the deck. This allows the user a 'look' at the sub-surface conditions, and can be performed very quickly. There are some applications where scans of bridge decks can be made at near highway speeds<sup>1</sup>. This avoids the need to close the bridge to traffic for inspection. However, compromises in resolution and sensitivity to certain defects have to be accepted<sup>6</sup>.

A few other methods were preliminarily evaluated. Impact Echo (IE) was briefly tested<sup>6, 7</sup>. This method uses frequency analysis of stress wave propagation through the deck to estimate the thickness and depth of defects. In preliminary lab tests IE was found to be a feasible means of estimating deck thicknesses, but shallow delaminations were more difficult to identify. A literary review shows that other researchers have had similar issues identifying depths of shallow delaminations<sup>8</sup>. Because delaminations are the focus of this research, the IE method is not discussed further.

Ultrasonic testing was also preliminarily considered<sup>6</sup>. This method uses the time-of-flight of stress waves as they propagate and reflect within the deck to determine defect depths and extents. While performing lab tests difficulties were found in coupling the sensors available for this research to the concrete specimens. Because the lab specimens can be expected to be much smoother than concrete bridge deck surfaces found in the field, this method was determined to be unfeasible and further evaluation of this method is not discussed. A new tool that employs an array of point contact ultrasonic shear transducers shows promise to aid in this problem<sup>1</sup>. However, this tool is expensive and requires extensive experience.

Ultimately, IR and GPR were chosen for further investigation because of their potential ability to identify delamination extents and depths, and their commercial availability. The goal was to use the two methods in combination: First, IR is used to locate the delaminations. GPR is then used to provide a more detailed view of the exact extent and depth of the delamination. The current practice both methods are described and evaluated. Modifications to the standard practice, in order to enhance the methods abilities to locate the extents and depths of delaminations, are also presented and evaluated.

## **Chapter 2**

### **IMPULSE RESPONSE**

#### **2.1 Background**

The Impulse Response (IR) method is a form of non-destructive testing (NDT) where the dynamic response of an element resulting from an impact event (hammer blow) is measured with a geophone or accelerometer to make conclusions about the element's integrity, stiffness, and/or support conditions. It is derived from the forced vibration method originally developed for, and used in, the aviation industry<sup>5</sup>. In this original method, a swept-frequency mechanical excitation is applied to the element and the maximum velocity response and the maximum force are recorded and divided at each applied frequency<sup>9</sup>. The first application of this method to civil infrastructure occurred in the 1960s when it was used to test the integrity of cast-in-place concrete piles<sup>10</sup>.

In the 1970s it was realized that a wide range of frequencies could be excited simultaneously using a short hammer strike in place of the swept-frequency excitation<sup>11</sup>, which reduces time, effort and required equipment needed for tests. This new approach has been referred to by many names including: shock method<sup>11</sup>, transient dynamic response method<sup>11, 12, 13</sup>, sonic mobility method<sup>5, 10, 11, 12, 13</sup> and most commonly Impulse Response (IR) method. IR first transforms both the received transient response (usually the velocity response obtained from a geophone sensor) and input forcing function response (usually obtained from an hammer instrumented with a load cell) into the frequency domain using a Fast Fourier Transform (FFT)

algorithm, and then divides the two signals at each frequency . The absolute value of this division is termed the “mobility” spectrum. This process can be seen in Figure 2.1 and Equation 2.1. The division in the frequency domain deconvolves the forcing function from the response signal. This leaves only the response from the system, in this case the concrete deck, which is isolated from variation in the forcing function (assuming the response is linear). From this spectrum, parameters can be calculated to give a quantitative assessment of the concrete structure.

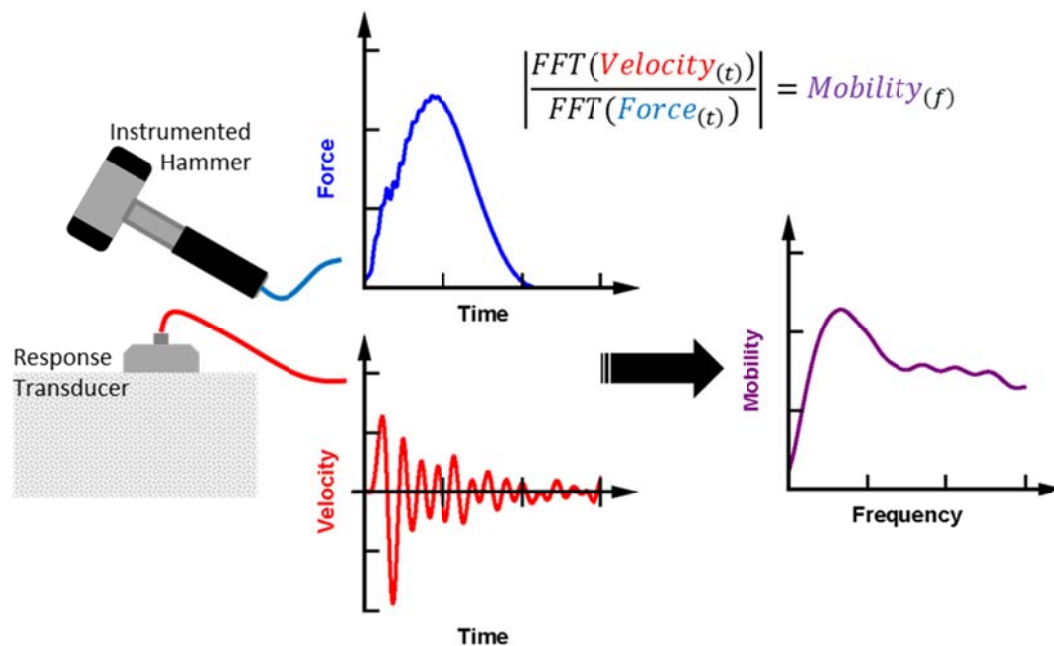


Figure 2.1 Impulse Response Testing Procedure.

$$Mobility_{(f)} = \left| \frac{FFT(Velocity_{(t)})}{FFT(Force_{(t)})} \right| \quad (2.1)$$

where:

$Mobility_{(f)}$  = *Mobility in the frequency domain* ( $m * s^{-1}/N$ )

$FFT()$  = *Fast Fourier Transform algorithm*

$Velocity_{(t)}$  = *Recorded velocity signal* ( $m/s$ )

$Force_{(t)}$  = *Recorded force signal* ( $N$ )

With advances in personal computers and data acquisition systems in the 1980s, the IR method was applied to other civil infrastructure elements beyond piles<sup>5</sup>. Hertlein and Davis documented the first application of this method to concrete plate-like structures in 1987<sup>12</sup>.

Because of the duration of the impact and the amount of energy in the hammer strike, a plate-like structure's response is dominated by bending or “drum” modes, where the structure behaves similarly to the skin of a drum after it has been struck. These responses have a much lower frequency than other typical forms of NDT (e.g. Impact Echo and Ultrasonic Testing), which rely on stress wave propagation to interrogate the structure.

In 2004, Ottosen et al. presented the first, and as far as the author is aware, the only attempt to explain the IR method on concrete plate-like structure, where an analytical solution was derived to identify the mobility of a concrete beam resting on a bed of sand<sup>13</sup>. The effects of loss of support and concrete honeycombing on the mobility were derived and presented. This study showed that voids in the otherwise continuous support of the beam increase the mobility in low frequencies, while

honeycombing increases the mobility in higher frequencies. This study only investigated slabs on grade, and did not address bridge decks.

### 2.1.1 Current Practice

ASTM Standard C1740-10<sup>14</sup> entitled *Standard Practice for Evaluating the Condition of Concrete Plates Using the Impulse-Response Method* is the current test standard used in practice for condition assessment of all concrete plates-like structures using the IR method, including bridge decks. This standard recommends performing IR tests on a grid across the element of interest and estimating the mobility at each grid point. Four different parameters are then obtained from the mobility spectrum as illustrated in Figure 2.2 and plotted as contours over the investigated area to indicate anomalies.

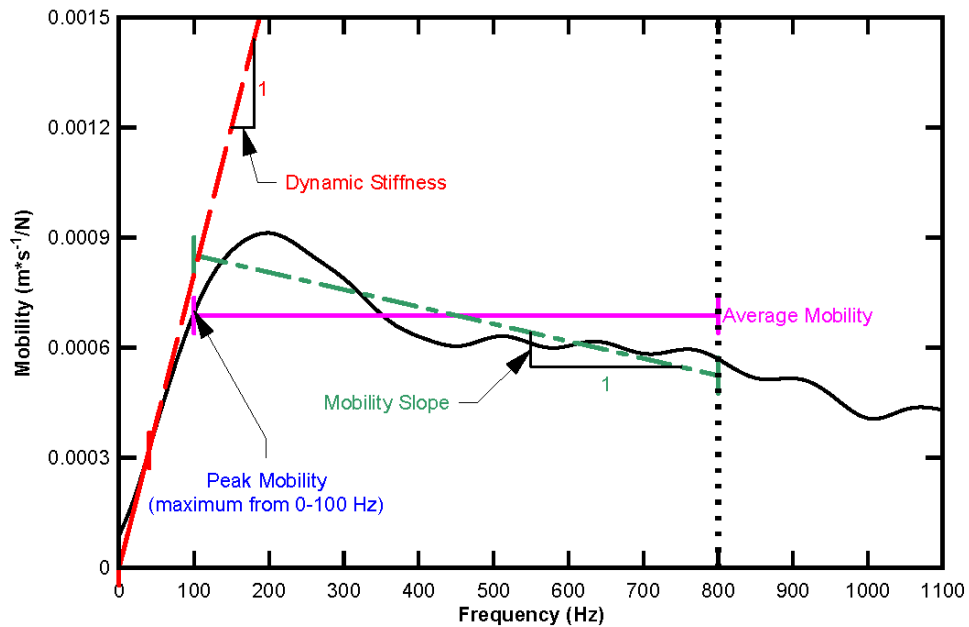


Figure 2.2 Example Mobility Spectrum (black line) and Analysis Parameters According to ASTM Standard C1740-10.

**Average Mobility** is calculated as the mean value of mobility within the frequency range of 100 to 800 Hz. This value is related to the elastic modulus, thickness, density, and indicates internal defects according to the standard.

**Dynamic Stiffness** is the inverse of the slope in mobility from 0 to 40 Hz. The standard correlates this parameter to the elastic modulus, thickness, support conditions, and presence of internal defects.

**Mobility Slope** is determined by the slope of a best-fit line to fit the mobility within the frequency range of 100 to 800 Hz. This parameter is used mainly to detect areas of poorly consolidated concrete.

**Peak-Mean Mobility Ratio** is the ratio of the maximum value of mobility below 100 Hz, and the Average Mobility. High values of Peak-Mean Mobility Ratios indicate debonding or loss of support beneath a slab on ground.

Typically, estimated parameters are compared relative to each other within one test area of comparable boundary conditions. It is unreasonable to compare these values from one bridge deck to another due to the different boundary conditions.

### **2.1.2 Equipment**

As specified in the standard, the equipment used in this evaluation included a 1.5 lb. instrumented hammer, a response transducer, and a multiple channel data acquisition system. The hammer is a PCB Impact hammer, model 086D20. It is commercially available with an integrated piezo-electric load cell. The signal from this load cell was amplified with a signal conditioner unit. It comes with interchangeable rubber tips of varying hardness, however only the hardest tip excites the required frequency range for IR testing (up to 1,500 Hz).



A capacitive broadband-type accelerometer was used to measure the surface motion response. This varies from the standard suggested geophone. Justification for this change is given in the section 2.1.2.1. The sensor was mounted to an aluminum disc to assist in coupling it to the surface, and prevent wear and tear on the sensor itself.

Both signal from the hammer and the accelerometer were recorded using a high-speed data acquisition system with a 1,500 Hz anti-aliasing filter. A PC was also used to store and later process the data. In the field, all of the equipment was powered by a battery and was placed on a cart as shown in Figure 2.3.



Figure 2.3 Example of IR Equipment Being Used in the Field.

All the processing was performed using the Matlab software package, and specific processing scripts developed for this research can be seen in Appendix B.1.

#### 2.1.2.1 Response Transducer

A comparative study was performed to justify the use of the accelerometer compared to the suggested geophone. IR testing was performed on a laboratory mock-up specimen with the same procedure as was performed on the bridge, except both an accelerometer and a geophone were used to record the response, simultaneously. Figure 2.4 shows the normalized mobility determined from both types of sensors as well as the ASTM Standard limit, above which the response does not affect the ASTM parameters.

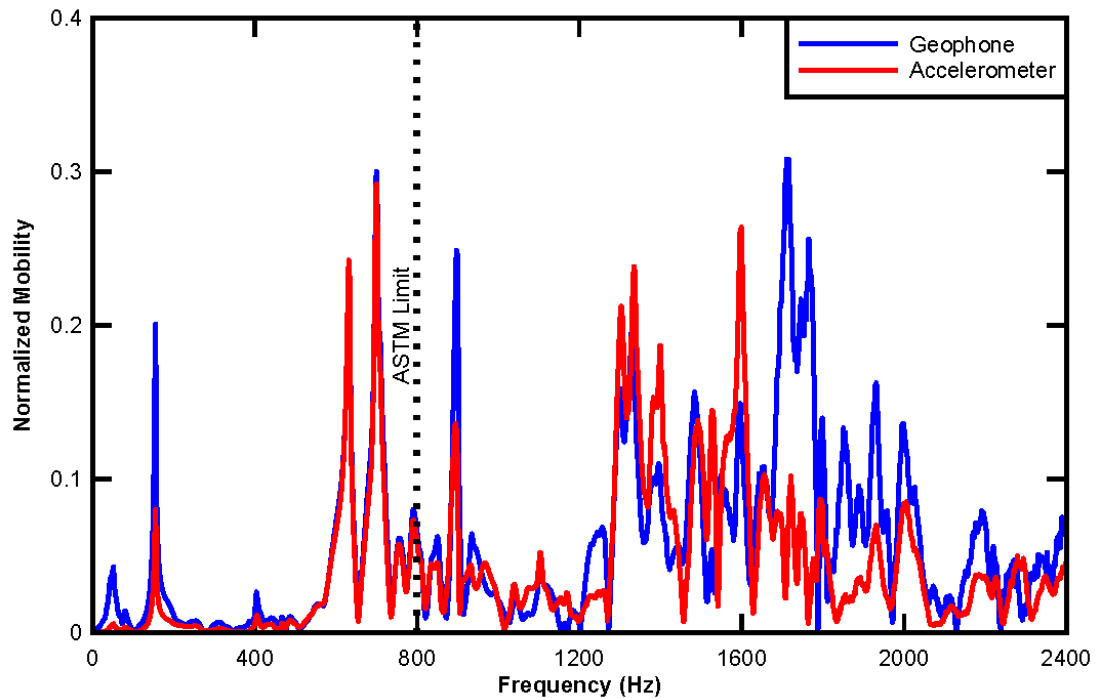


Figure 2.4 Mobility of Laboratory Specimen with the Response Measured by an Accelerometer and a Geophone, simultaneously.

The only significant difference is in the frequencies below 20 Hz, which is likely a product of the numerical integration required to convert the acceleration data to velocity. The frequencies higher than 1,500 Hz have different magnitudes, but show similar trends. This is due to the fact the accelerometer has a flat response up to 4,000 Hz whereas the geophone only to about 1,000 Hz. Because these differences are above the ASTM limit of 800 Hz, it has been concluded that both the geophone and accelerometer are equally effective for IR testing.

## 2.2 Field Tests

To evaluate this methods effectiveness IR testing was performed on two bridge decks with known delamination issues.

### 2.2.1 Branchport Bridge

The IR method was applied in the field on the deck of the Branchport Bridge, in New Branch, NJ, on July 26, 2011 during a full bridge closure. The Branchport Bridge is a 216 ft. long concrete-steel-composite bridge consisting of six adjacent non-prestressed reinforced concrete decks. Each deck represents a two-span continuous system with span lengths of 18 ft. Figure 2.5 shows the cross-section plans of this bridge.

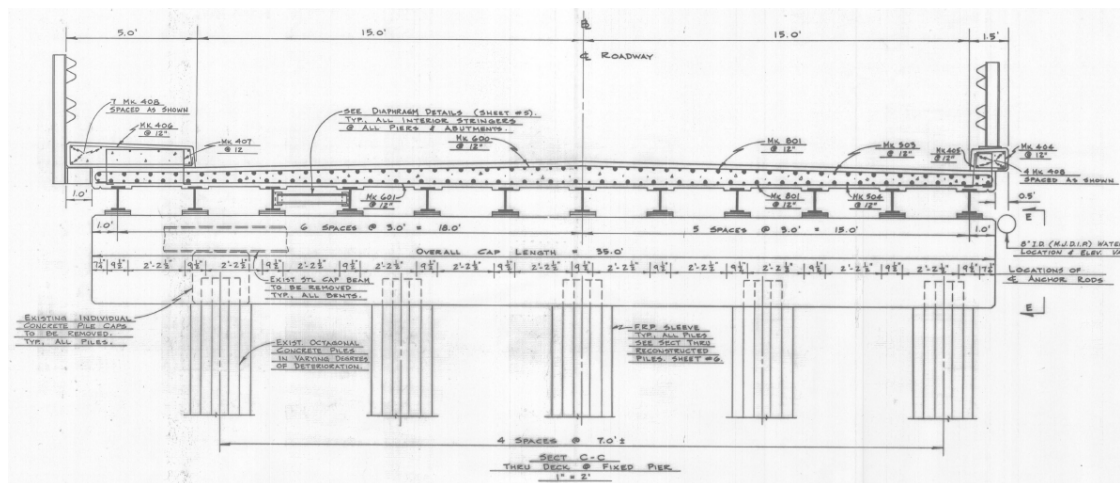


Figure 2.5 Cross-section of the Branchport Bridge.

The deck of this 25 year old bridge shows severe visual deterioration in form of spalling and pot holes which resulted, in some locations, in the exposure of the steel reinforcing bars. Conventional sounding had revealed that large areas having potential

shallow delaminations. Figure 2.6 shows a plan view of each deck measured. Note that the areas of delamination indicated by sounding have been outlined in white.



Figure 2.6 Plan View of Branchport Bridge; Decks 1 through 6 (left to right).

Testing was performed on five of six deck spans according to the ASTM C1740-10 Standard<sup>14</sup>. The sixth deck span was not tested due to time constraints. Testing was performed on a 2 ft. by 2 ft. grid. Both the force and acceleration signal were recorded at a sampling rate of 500,000 samples a second (= 500 kHz) for a total duration of 500 ms. Those signals were later trimmed to 200 ms.

The grid points on the first two decks were recorded four times each, with varying force. The first impact was relatively soft, proceeded by a medium-soft impact, then a medium-strong, then a strong impact. Deck number 3 was tested similarly, but with only three impacts per test point. Decks 4 and 5 were tested only once per grid point, with a medium impact at each point.

All four ASTM parameters were determined at each grid point and plotted as contour lines over the top of a rectified photo of the deck itself. The limits of the contours were determined qualitatively to best highlight areas in which the parameter differed significantly from the average. Because deck number 4 has areas of delamination and areas that appear solid, each of the four parameters for this deck are shown in Figure 2.7 as an example. Plots of the other decks can be seen in the

Appendix A.1. In this figure the colored lines are the contours of the calculated parameter, with warmer colors indicating anomalies. Again, the white lines on the underlying photo are the results from sounding and visual inspection. They can be used as a guide for possible delaminations, but the exact locations of internal flaws are, to this point, unknown.

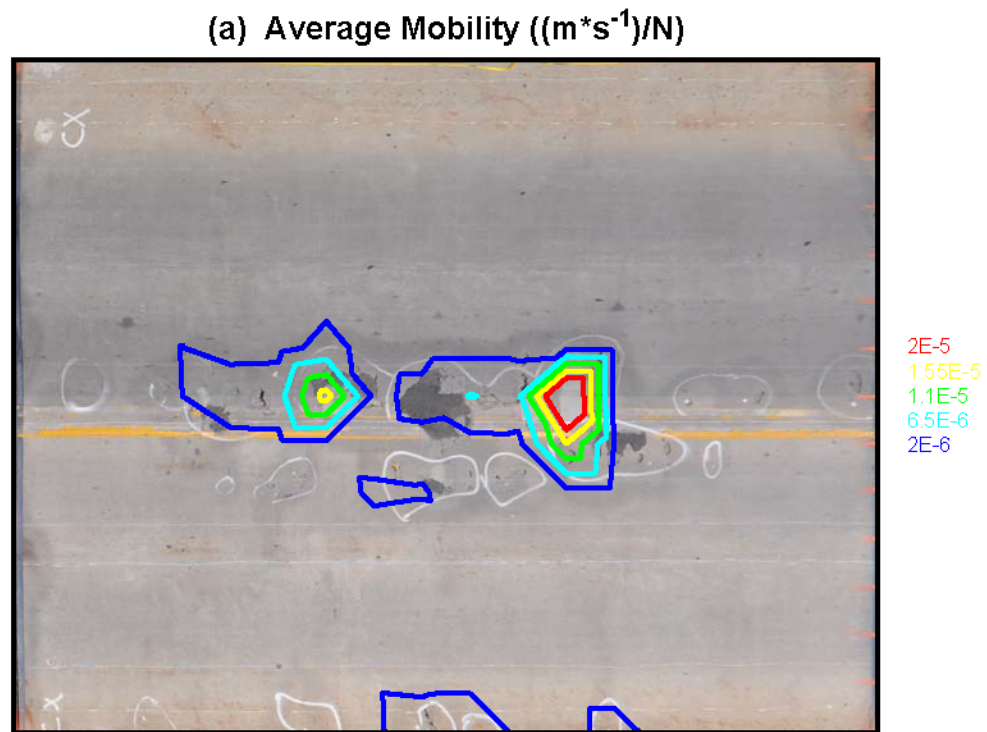
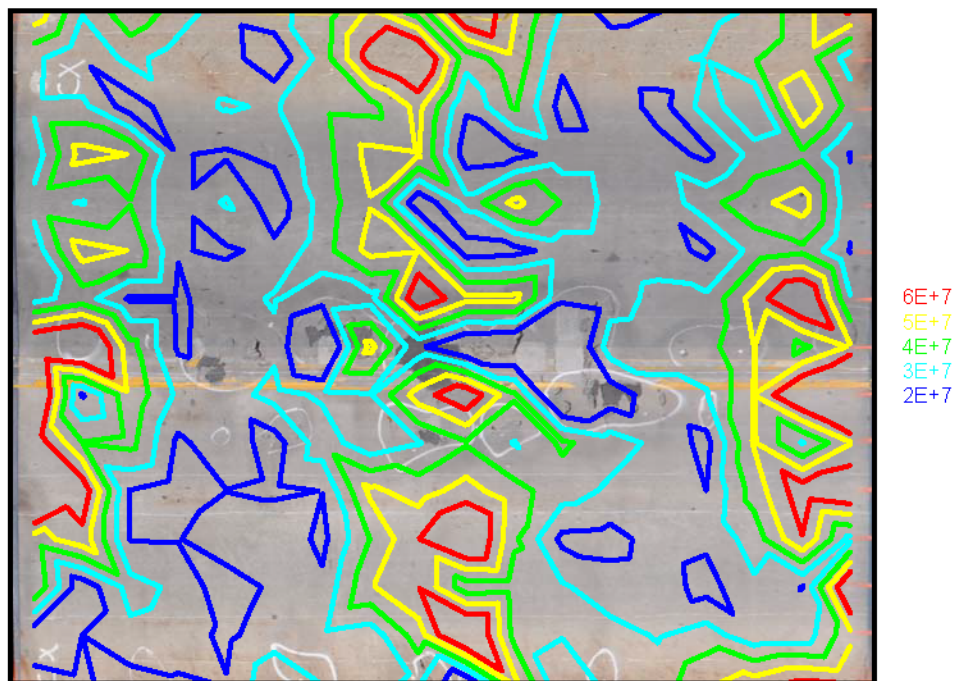


Figure 2.7 IR Parameters of the Branchport Bridge, Deck 4; ASTM Standard C1740-10 (a) Average Mobility, (b) Dynamic Stiffness, (c) Mobility Slope, (d) Peak Mean Ratio.

(b) Dynamic Stiffness (N/m)



(c) Mobility Slope (m/N)

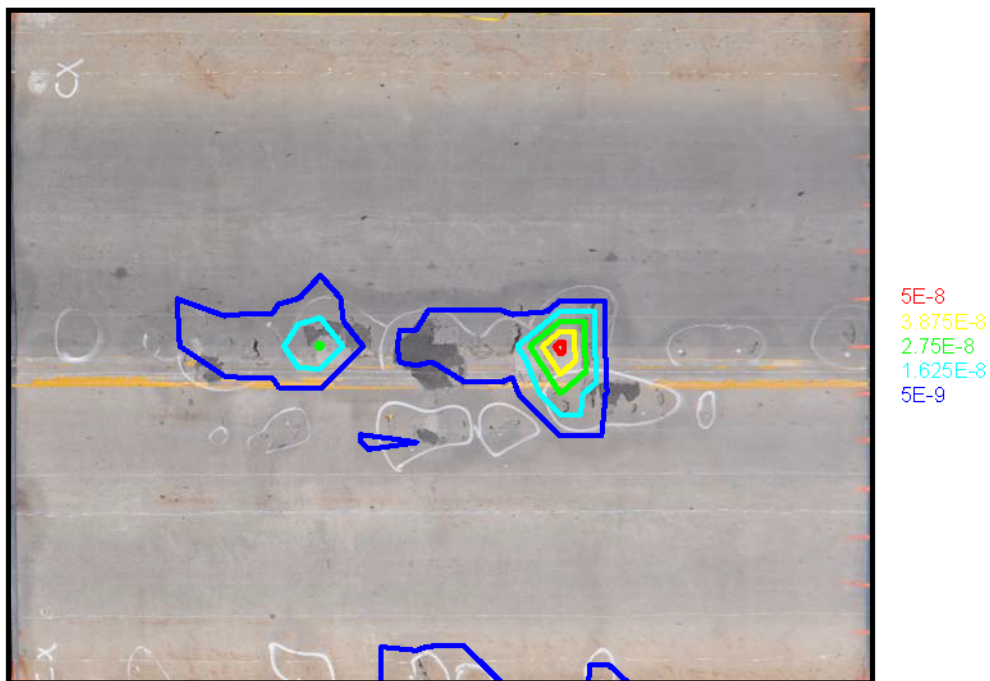


Figure 2.7 Continued



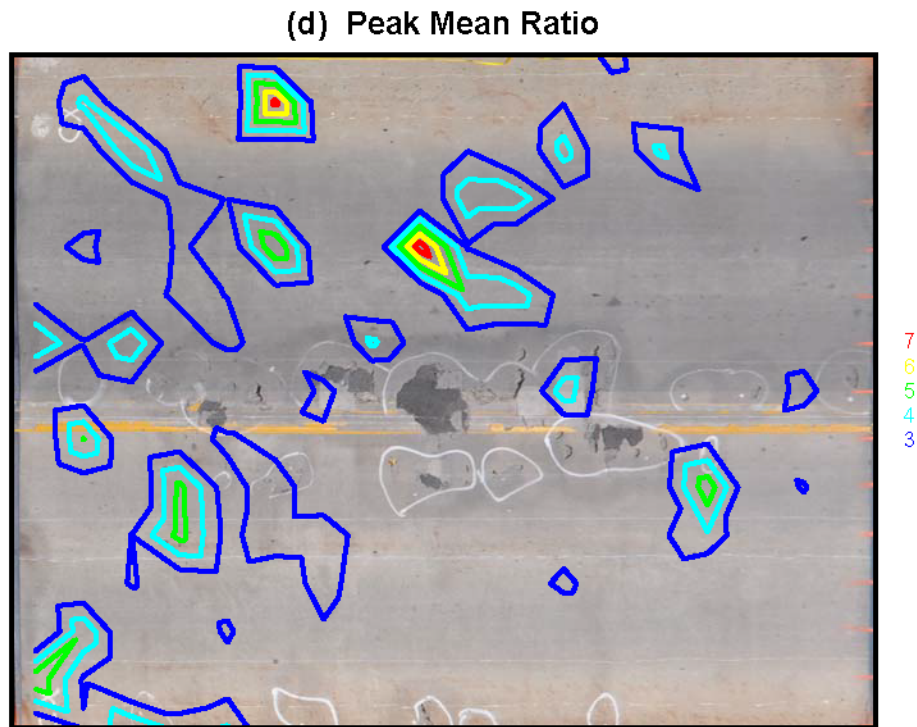


Figure 2.7 Continued

It appears as though both average mobility and mobility slope are good indicators of delaminations as they seem to strongly correlate with the sounding results. According to the standard this should be expected for the average mobility as it specifically mentions internal flaws influencing this parameter. However the mobility slope is only said to indicate honeycombing, not delaminations, and its correlation to the visual inspection were thus not expected.

The dynamic stiffness seems to vary independently from expected delaminations. Actually it seems to be strongly influenced by support conditions. Remember that this deck is integrated with steel girders, and this composite creates a two-span system. Notice that the values of dynamic stiffness are higher at the center



and the two edges where the three supporting bents are located. This instinctively makes sense; the deck is stiffest directly above the supports. This can also be explained by the fact that the frequencies used to compute this parameter are too low to be influenced by small local defects.

The peak mean mobility ratio also doesn't correlate with expected delaminations.

From investigating this deck, and the others tested, it is clear that using the one of parameters outlined in the ASTM standard alone gives very little confidence in delamination predictions. These parameters can be strongly influenced by other factors such as support conditions. Looking for trends in the contours of multiple parameters may give more confidence in the results. But even then these results must be calibrated by other means, such as coring.

### **2.2.2 Del-DOT Bridge 1-245**

The IR method was again applied in the field on the deck of the Delaware Department of Transportation (DelDOT) bridge 1-245 in Newark, Delaware. This test was conducted only on the North-bound lane during a partial road closure. DelDOT Bridge 1-245 carries Harmony Road over the AMTRAK railway. It is a 215 ft. long, 46 ft. wide, skewed steel-concrete composite bridge, and has an 8 inch thick concrete deck cast with stay-in-place formwork, as seen in Figure 2.8.



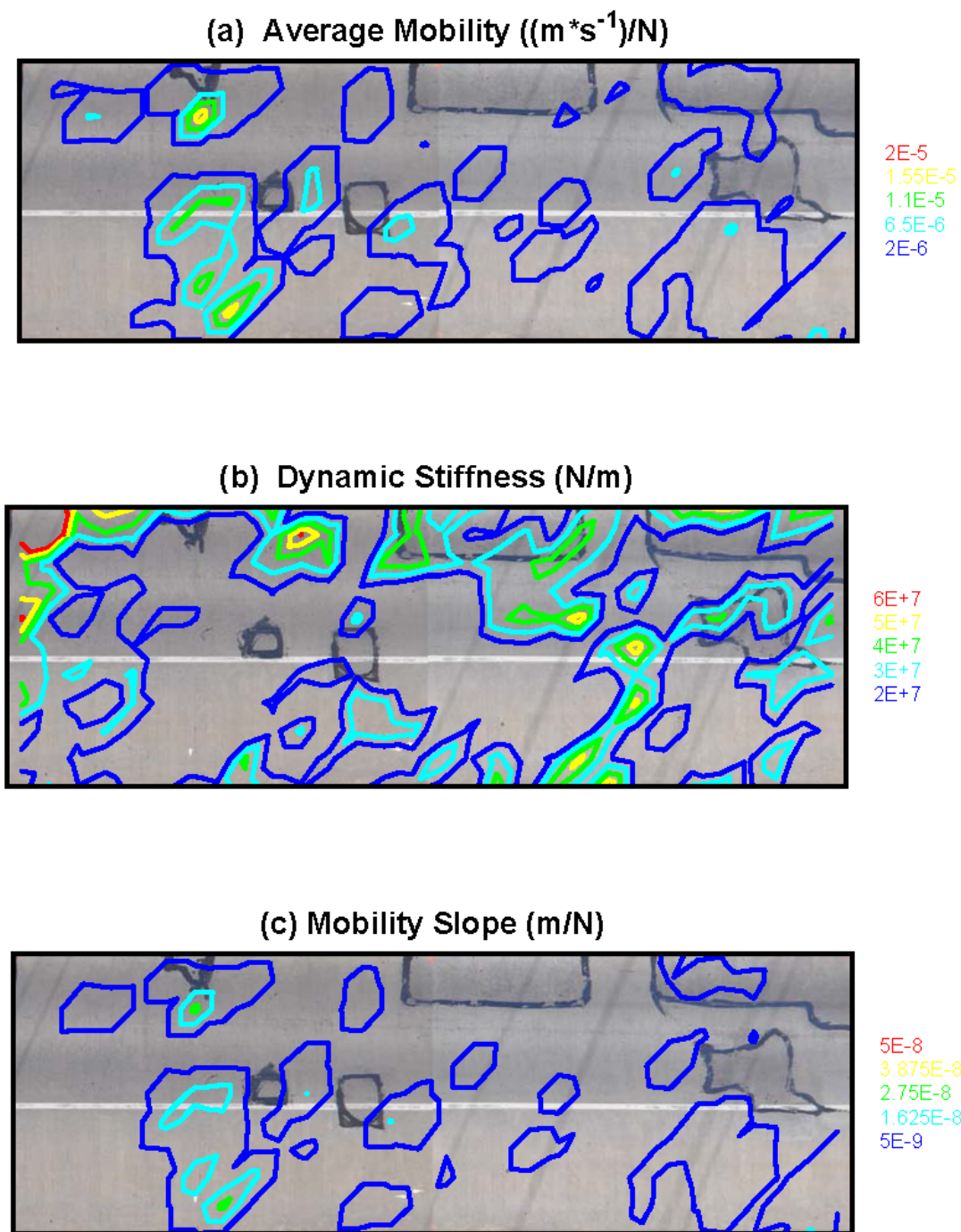


Figure 2.9 IR Parameters of the Del-DOT 1-245 Bridge; ASTM Standard C1740-10  
(a) Average Mobility, (b) Dynamic Stiffness, (c) Mobility Slope, (d) Peak Mean Ratio.

(d) Peak Mean Ratio

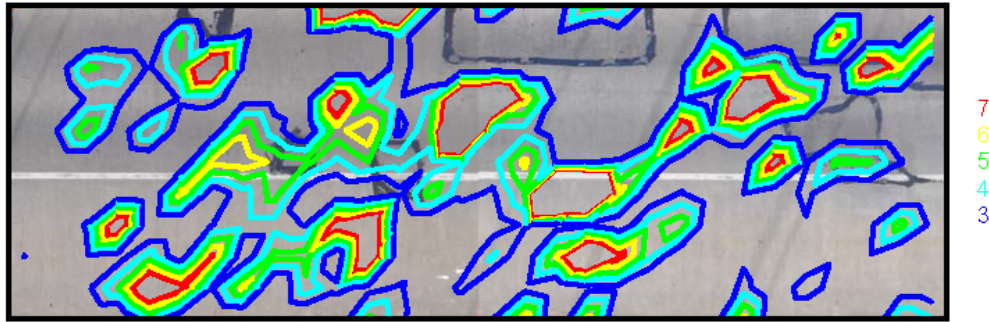


Figure 2.9 Continued

Unlike the Branchport Bridge we do not have visual inspection markings to base conclusions on, which is more typical. It seems as though the average mobility and the mobility slope confirm each other as they each indicate anomalies near the same places. But without confirmation these results are vague at best.

### 2.3 Numerical Simulations

In order to develop a better understanding of the underlying physics of IR testing of concrete bridge decks, a plane strain Finite Element (FE) model was created in ABAQUS using 2-D quadrilateral elements as illustrated in Figure 2.10. This model was originally developed by Dr. John Popovics, et.al for simulating Impact Echo testing. The author worked with them to modify their model to simulate a section of the Branchport Bridge presented in section 2.2.1 tested with IR. The following is the results of their study as presented in *Understanding The Impulse Response Method Applied To Concrete Bridge Deck*<sup>15</sup>.

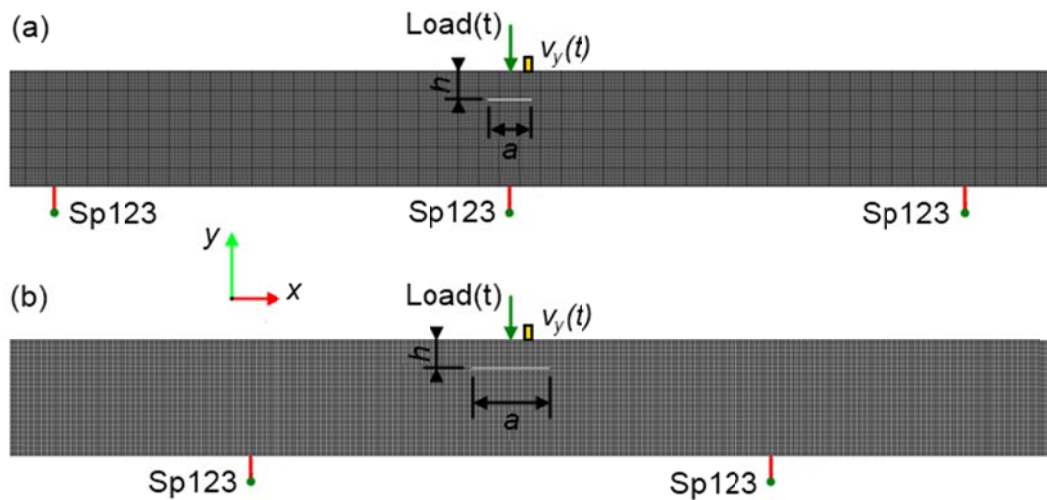


Figure 2.10 Illustration of ABAQUS FE Model: (a) Delamination Centered Above a Girder, (b) Delamination Centered Between Two Girders. IR Testing Point, Indicated by Green Arrow, is Applied at Center of Delamination Width.

The simulated deck thickness was 250 mm ( $\sim 10$  in.) and the girder spacing 1000 mm ( $\sim 40$  in.). The width of the delaminations,  $a$  was varied between 100 mm and 1200 mm and the depth,  $h$  was 60 mm for all cases. A solid deck having no delamination was created for reference. The girders were modeled with springs (indicated by ‘Sp123’) having a spring constant of 109 N/m.

The forcing function imposed on the FE models was modeled after measurements from the Branchport Bridge test where the contact time was found to be approximately 1.8 ms. Both the forcing function used in the simulation and the force found in field experiments are shown in Figure 2.11. The FE model was run at 100 kHz for a total length of 100 ms. which complies with the ASTM Standard<sup>14</sup>. The velocity response was recorded 100 mm away from the applied load, mimicking the placement of the sensor in field experiments.

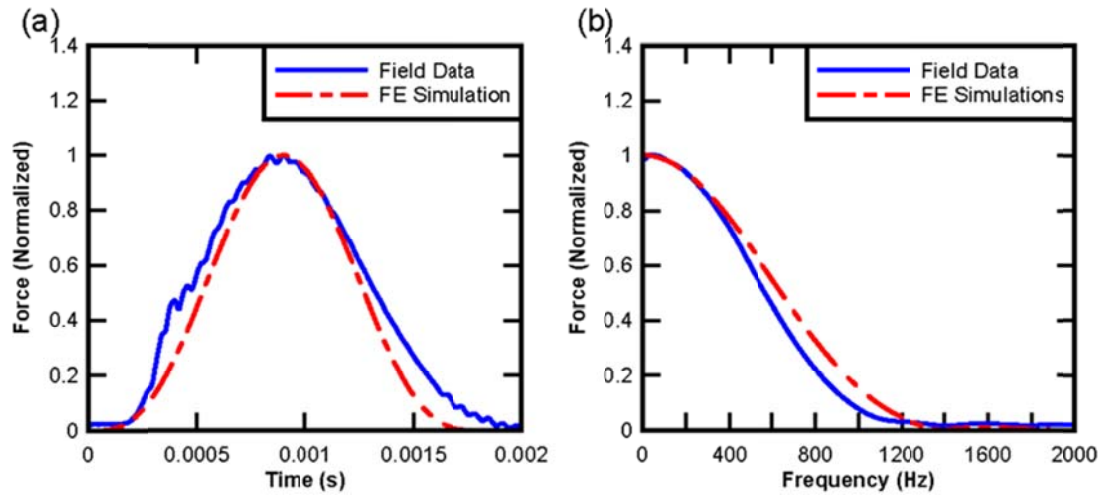


Figure 2.11 Force Recorded in Field Experiment and Forcing Function used in FE Simulation: (a) Time Domain, (b) Frequency Domain.

Figure 2.12 shows the mobility, calculated for a variety of delamination widths at a section mid-span between two girders. Interestingly, the apparent resonance of the delamination (observed as a large spectral peak in the response) does not lie within the frequency range that the ASTM Standard specifies until the delamination is at least 300 mm wide. The FE results suggest that all delaminations smaller than 300 mm are undistinguishable from the solid section within the ASTM limits.

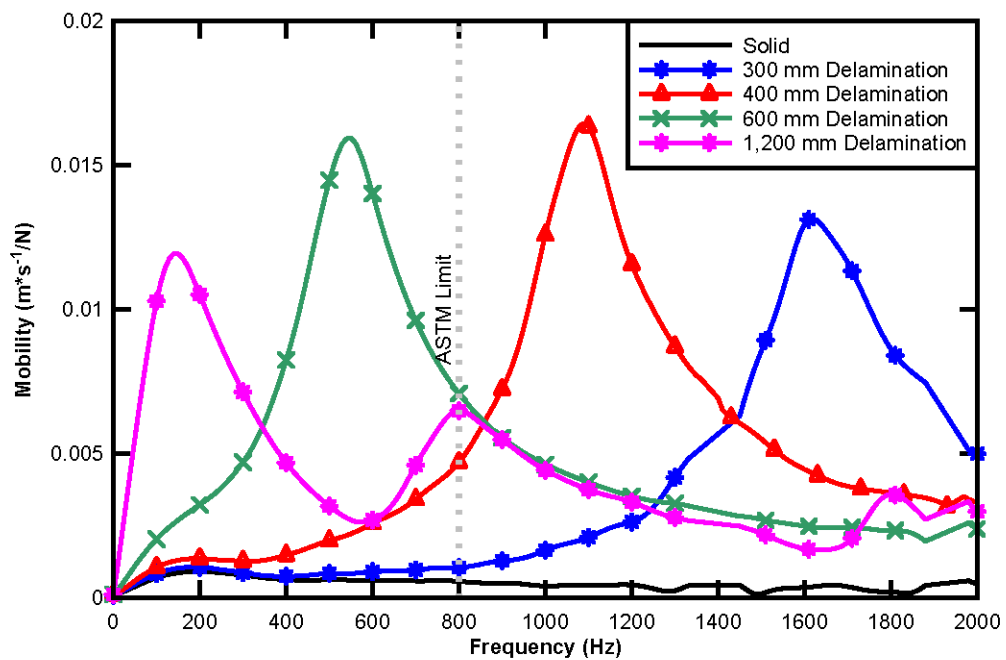


Figure 2.12 Mobility of FE Simulated Solid Sections and Sections with Delaminations of  $a = 300$  mm, 400 mm, 600 mm, and 1,200 mm Width (directly above the girder)

Figure 2.13 shows the effects of the location of the delamination relative to the girders for a solid section and a 600 mm wide delamination. For small delaminations, the location has a larger relative effect on the mobility than the delamination itself.

Although there is some difference in the mobility of the larger delaminations, the size of the delamination controls the response.

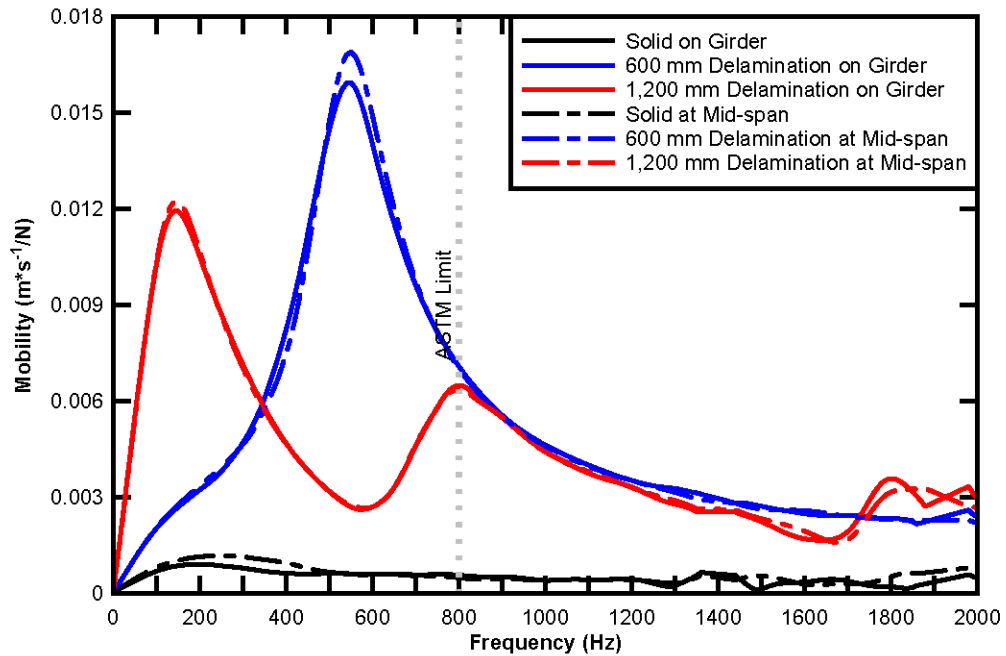


Figure 2.13 Mobility of a FE Simulated Solid, and a = 600 mm and 1,200 mm Wide Delamination, Both Above Girder and Mid-span Between Girders.

The parameters specified in the ASTM Standard are reported to be controlled in part by internal defects, debonding, or shallow delaminations. All four of the parameters were estimated using the FE results and are plotted in Figure 2.14 as a function of the delamination width, for both the case with the delamination above the girder and in between girders. The location of the delamination with respect to the girder affects each of these parameters, especially for small (< 300mm wide) delaminations. This means that without knowing the location of the girder, it would be



difficult to accurately predict the presence of a delamination in the deck. Only the Dynamic Stiffness parameter monotonically changes, i.e. decreases with respect to delamination size; the other parameters show varying (non-unique) responses. For example, a value for the Peak Mean Ratio, the parameter specified by the standard to detect debonding and delaminations, calculated as approximately 1 would simultaneously predict a solid section, a 300 mm delamination, and a 900 mm delamination for both support conditions, i.e. the prediction is not unique. This is due to the way the parameters are defined using fix frequency limits. The support condition (above or at mid-span between girder) has little or no effect on the estimated parameters except for Dynamic Stiffness for delaminations smaller than 600 mm.

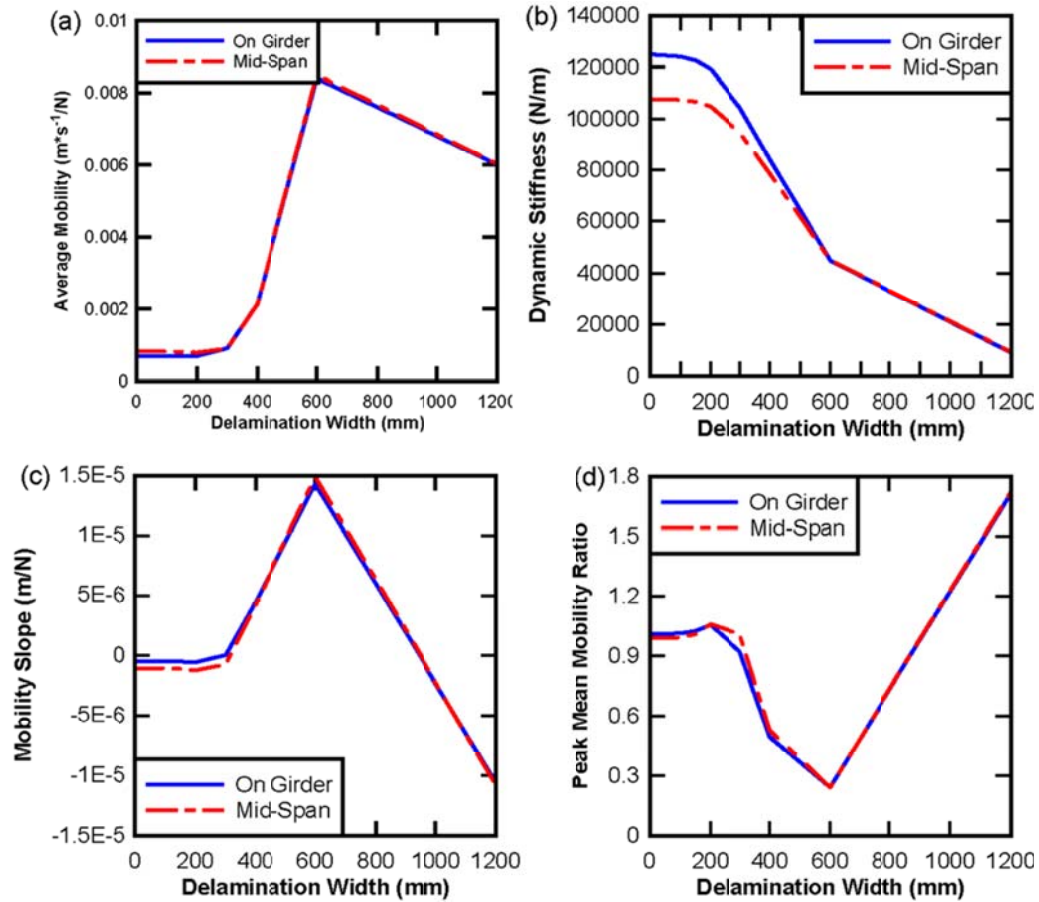


Figure 2.14 ASTM Standard Parameters Plotted as a Function of the Delamination Width, a (a) *Average Mobility*, (b) *Dynamic Stiffness*, (c) *Mobility Slope*, (d) *Peak Mean Mobility Ratio*.

## 2.4 New Procedure

As shown in the field results, the four parameters specified in the ASTM standard can be used to preliminarily estimate areas of possible delamination. However, very little confidence can be put into any one parameter if it stands alone. The simulated model results show that these parameters can also be dependent on the support conditions that inevitably vary over a bridge deck. These parameters can also be difficult to conceptualize and have shown little theoretical meaning.

To attempt to resolve these issues a new post-processing procedure has been developed. This procedure does not change the way the data is collected, simply how it is processed after collection. In this procedure the mobility is calculated in the same fashion as the standard procedure. A Fast Fourier Transform (FFT) algorithm is applied to both the velocity (in this case the integrated acceleration) and the force signals. These two signals are divided to determine the mobility in the frequency domain. In the old procedure, parameters are pulled directly from this mobility spectrum. However, in the new procedure an inverse FFT algorithm then is applied to the mobility, transforming the signal back into the time domain. This new procedure can be seen in Figure 2.15 and Equation 2.2.

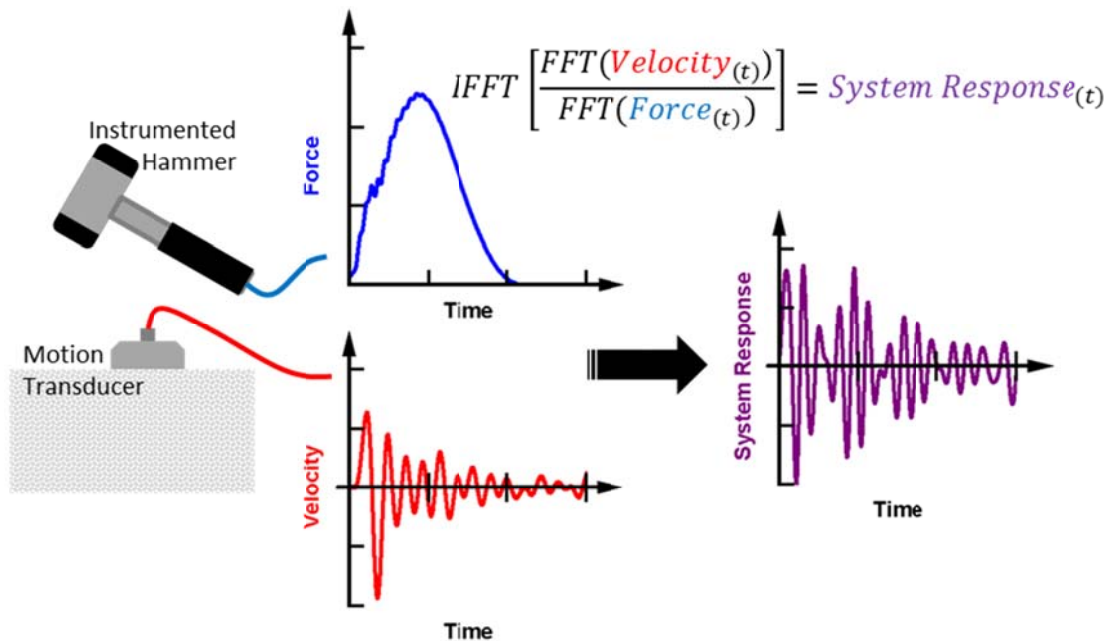


Figure 2.15 New Suggested Impulse Response Testing Procedure.

$$\text{System Response} = \text{Mobility}_{(t)} = \text{IFFT} \left[ \frac{\text{FFT}(\text{Velocity}_{(t)})}{\text{FFT}(\text{Force}_{(t)})} \right] \quad (2.2)$$

where:

$\text{System Response} = \text{Mobility}_{(t)}$

$\text{Mobility}_{(t)} = \text{Mobility in the time domain } (m * s^{-1}/N)$

$\text{IFFT}() = \text{Inverse Fast Fourier Transform algorithm}$

$\text{FFT}() = \text{Fast Fourier Transform algorithm}$

$\text{Velocity}_{(t)} = \text{Recorded velocity signal } (m/s)$

$\text{Force}_{(t)} = \text{Recorded force signal } (N)$

The complex division in the frequency domain deconvolves the forcing function from the response signal. This leaves only the response from the system, in this case the concrete deck, which is isolated from variation in the forcing function (assuming the response is linear). But responses in the frequency domain can be difficult to interpret, so this system response is transformed back into the time domain where its significance is easier to understand. Because deconvolution of two signals with some inherent noise can magnify the noise, a smoothing algorithm must be applied to this signal to achieve interpretable results (i.e. moving average filtering). This smoothing algorithm should be set in such a way that the lower bound is at least set above the anti-aliasing filter used during recording to ensure it does not adversely affect the data.

The mobility in the time domain calculated in this fashion will be referred to as the ‘system response’. The resulting units of the system response are velocity per force, compared to the arbitrary units in the frequency domain. Parameters from the

system response can be determined that may be more meaningful and easier to interpret than those determined from the mobility spectrum. Two possible parameters are evaluated and can be seen in Figure 2.16.

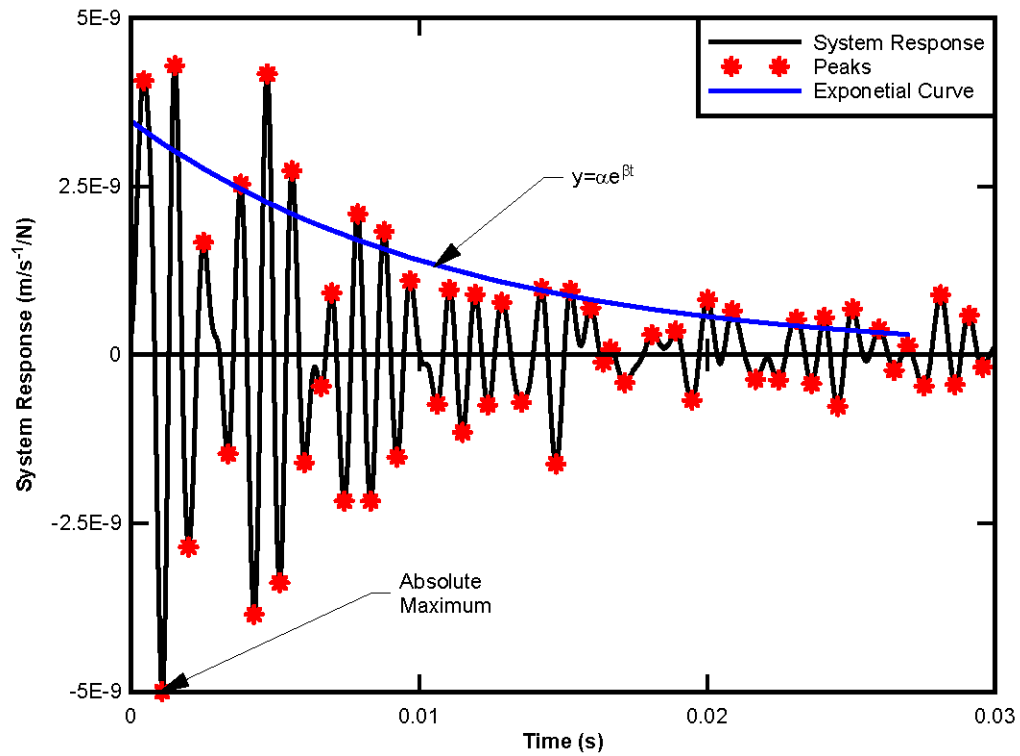


Figure 2.16 Possible Parameters for the New IR Procedure.

**Maximum System Response** is the absolute largest value in the system response. The higher the system response is, the faster the deck moves per unit force. It is easy to conceptualize that a weak, flawed section of a concrete deck will move much faster than a strong solid section due to a unit force.

**System Response Damping** represents how quickly the deck vibrations attenuate. This parameter is calculated by first finding the absolute magnitude of the peaks of each

oscillation in the system response. An exponential equation is then fitted to these peaks following Equation 2.3. The rate, at which the fitted equation decays,  $\beta$ , is determined to be the System Response Damping parameter. It is hypothesized that the more damping in the system, the more likely the system has some type of non-linearity (flaw).

$$Y = \alpha * e^{\beta t} \quad (2.3)$$

where:

$\beta$  = The decay rate and prediction parameter

To compare these new parameters to the standard parameters both the maximum system response and the damping for the fourth deck on the Branchport Bridge have been plotted in Figure 2.17. These figures can be compared to Figure 2.7 which shows the plots of the standard parameters.

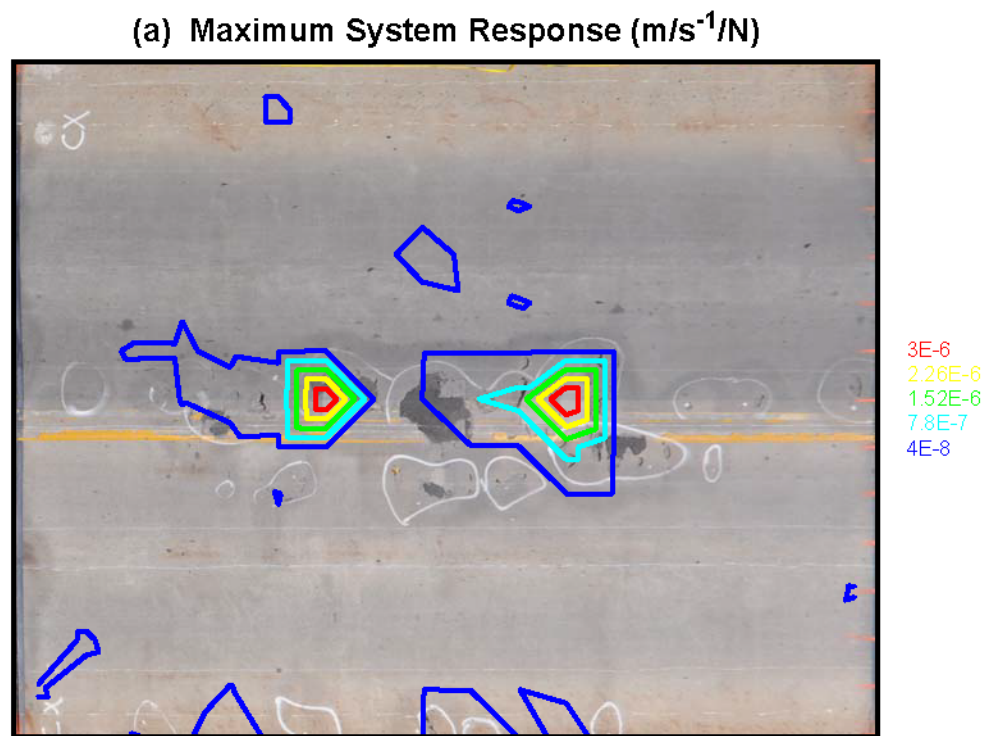


Figure 2.17 New IR Parameters of the Branchport Bridge, Deck 4: (a) Maximum System Response, (b) System Response Damping.

(b) System Response Damping

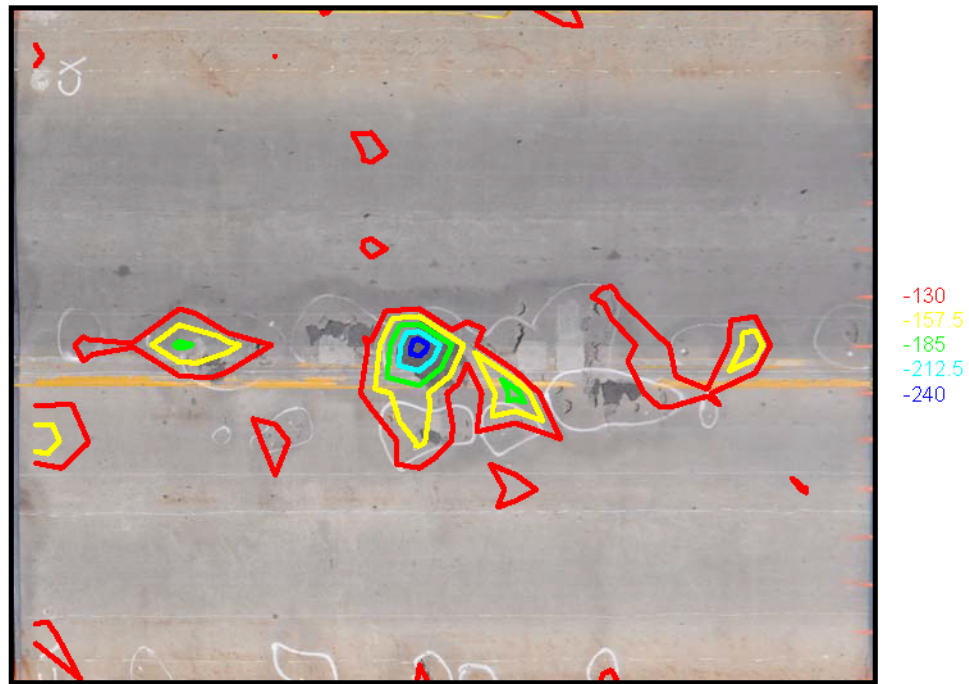


Figure 2.17 Continued

Both of these new parameters seem to compare closely to both the average mobility and the mobility slope parameters outlined in the ASTM Standard. Without more work to theoretically, analytically, and empirically support these parameters little confidence can be put in them when they stand alone. However in combination with the ASTM parameters and other forms of testing, they can be helpful in estimating areas of deck delaminations.



## 2.5 Discussion

The Impulse Response (IR) method for detecting delaminations on concrete bridge decks is investigated. The standard method (ASTM C1740-10) and its limitations that have been observed while applying the method to detect delaminations have been discussed. A Finite Element (FE) model was constructed to simulate a range of shallow delaminations on a concrete bridge deck. And a new procedure for post-processing has been developed in attempt to identify the limitations of the current standard. The following can be concluded:

- The ASTM standard set of parameters, when used in combination, can be used to estimate locations of large delaminations.
- Little confidence can be put into one single parameter as indicator of delaminations as compared to visual inspection.
- Flexural resonance of some delaminations can occur outside of the frequency range of 0 to 800 Hz that is defined by the ASTM Standard.
- The position of test relative to the girders appears to have a larger effect on standard parameters than the size itself for small delaminations ( $a < 300$  mm for  $h = 60$  mm).
- The position of test relative to supporting bent may also have an effect on the standard parameters.
- Most Standard parameters do not monotonically change with the delaminations size. As a result, even if the location of a delamination is known, its size cannot be uniquely determined.
- The newly proposed parameters can be used in addition to confirm the standard ASTM parameters.

## Chapter 3

### GROUND-PENETRATING RADAR

#### 3.1 Background

Ground-Penetrating Radar (GPR) is a method of Non-Destructive Testing (NDT) commonly used to determine sub-surface conditions of a number of civil engineering infrastructures<sup>16</sup>. Originally it was developed to evaluate soil conditions in a geotechnical application<sup>17</sup>. Recently it has been applied to assess structural concrete<sup>17</sup>. ASTM Standard D6087-08 gives guidance on how to perform surveys for concrete bridge decks<sup>18</sup>.

The principal behind GPR testing is relatively simple: A short electro-magnetic pulse is transmitted from an internal antenna in to the material of interest. This pulse has a center frequency typically ranging anywhere from 500 MHz to 1 GHz<sup>17</sup> or higher for concrete applications. Lower frequencies can penetrate deeper into the concrete, but do not have as high of a resolution as higher frequency pulses.

This pulse travels from the antenna, through the material at a speed inversely proportional to the materials relative dielectric constant, as shown in Equation 3.1. The relative dielectric constants of different materials can be seen in Table 3.1.

Table 3.1 Relative Dielectric Constants of Civil Materials

Material	Relative Dielectric Constant
Air	1
Soil	2 to 10
Asphalt	2 to 4
Concrete	4 to 10
Water	81
Steel	$\infty$

$$C_{material} = \frac{C_{air}}{\sqrt{\epsilon_{material}}} \quad (3.1)$$

where:

$C_{material}$  = Wave speed through material

$C_{air}$  = Speed of light ( $0.3 \frac{m}{ns}$  (11.8 in./ns))

$\epsilon_{material}$  = Relative Dielectric Constant (Table 3.1)

When the pulse reaches an interface with a different dielectric constant, a portion of the pulse is reflected back towards the antenna following Equation 3.2<sup>17</sup>. The antenna records the magnitudes of the pulse's reflections and creates an output signal.

$$\frac{A_r}{A_i} = \frac{\sqrt{\varepsilon_2} - \sqrt{\varepsilon_1}}{\sqrt{\varepsilon_2} + \sqrt{\varepsilon_1}} \quad (3.2)$$

where:

$A_i$  = Amplitude of the incident wave

$A_r$  = Amplitude of the reflected wave

$\varepsilon_1$  = Relative Dielectric Constant of the first material

$\varepsilon_2$  = Relative Dielectric Constant of the second material

The large difference in the dielectric constants between concrete and steel makes reinforcing bars excellent reflectors, redirecting most of the pulse's energy back towards the antenna. This allows the bars to be easily detected. As a result however, a shielding effect is created that makes it practically impossible to 'see' behind steel reinforcing bars.

The difference in dielectric constants of concrete and air are less significant. This makes cracks, voids, and other defects more difficult to detect. This is especially true in the presence of steel. But because less of the pulse is reflected, energy can penetrate beyond such deteriorations. This allows deteriorations to be indicated by the relative attenuation of the energy from a known reflector below the deterioration, rather than a weak reflection from the deterioration itself.

### 3.1.1 Current Practice

A variety of GPR devices exist depending on the application: from larger vehicle mounted antennas to small light hand held units<sup>6</sup>. Independent of the device, some type of encoding device has to be used so that the data recorded can be designated to a specific location on the bridge deck. The device is then moved across

the surface of the deck recording signals at some given interval. After that, the data can be post-processed. The post-processing typically follows the procedure outlined in Figure 3.1.

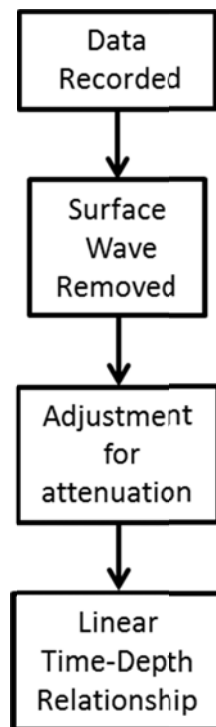


Figure 3.1 Typical Post-Processing Procedure for GPR Data.

Typically the surface wave is removed from each signal first. A surface wave consists of the first reflection of the pulse off of the surface of the deck. Because this portion of the signal does not penetrate into the material, it gives no information about the sub-surface conditions and as such is an artifact. The typical surface wave of a specific device maybe available through the device's manufacturer and can be subtracted from each output signal. Or the portion of the signal affected by the surface

wave can be neglected all together; however this will also neglect any reflections that are near the surface of the material.

Signal damping is another concern for GPR data. As the pulse penetrates into the material, the energy is geometrically attenuated. Signal energy is also absorbed by water above the surface and within the material<sup>18</sup>. Both the geometric and water related attenuation reduce the amount of energy reflected the deeper the pulse penetrates into the material. This causes reflectors deeper in the material to appear faint relative to the same reflector closer to the surface. The most basic way this is adjusted for by magnifying the data later in the time signal where each signal amplitude value is magnified by a specified factor that linearly increases with time.

Once the surface wave is removed and the signal is magnified to adjust for attenuation, time is transformed into depth. To do this, a linear relationship is assumed between depth and time as shown in Equation 3.3.

$$D = \frac{C_{conc} * t}{2} \quad (3.3)$$

where:

$D = \text{Depth to reflector}$

$C_{conc} = \text{Wave speed through concrete (Eqn. 3.1)}$

A single output signal recorded at a specific location is termed ‘A-scan’. Typically these A-scans will be recorded at a set interval along a straight path. When the path of A-scans are shown together with the magnitude represented in gray-scale, the time (or depth) shown on the y-axis, and the distance along the line shown on the x-axis, it is referred to as a ‘B-scan’. A typically processed A-scan and a B-scan of lab

specimen replicating a typical bridge deck is shown in Figure 3.2-4, as well as a sketch of its known section.

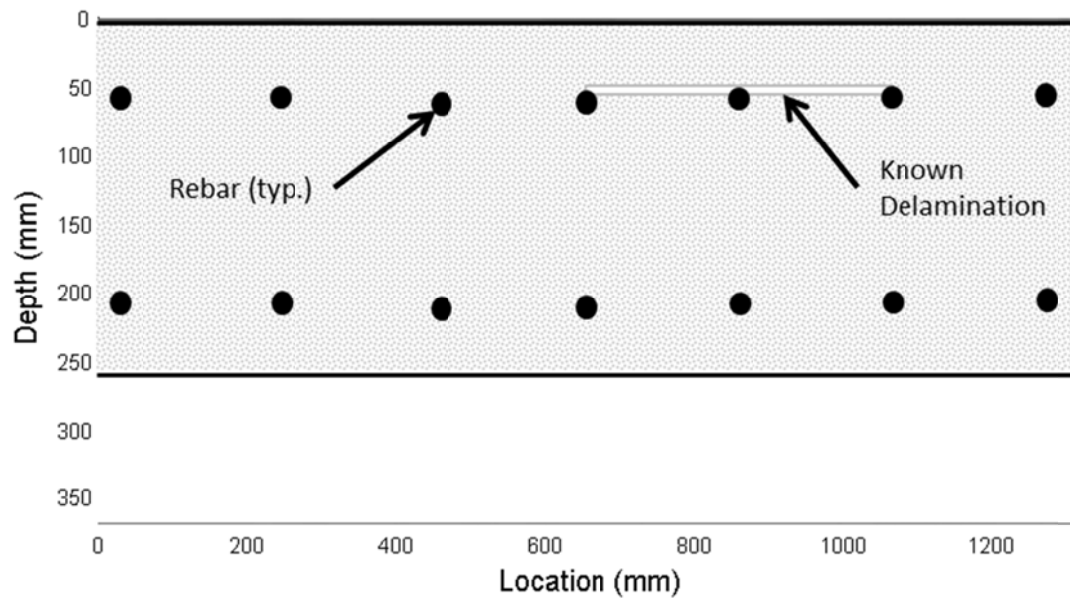


Figure 3.2 Sketch of a Lab Specimen Tested with GPR.

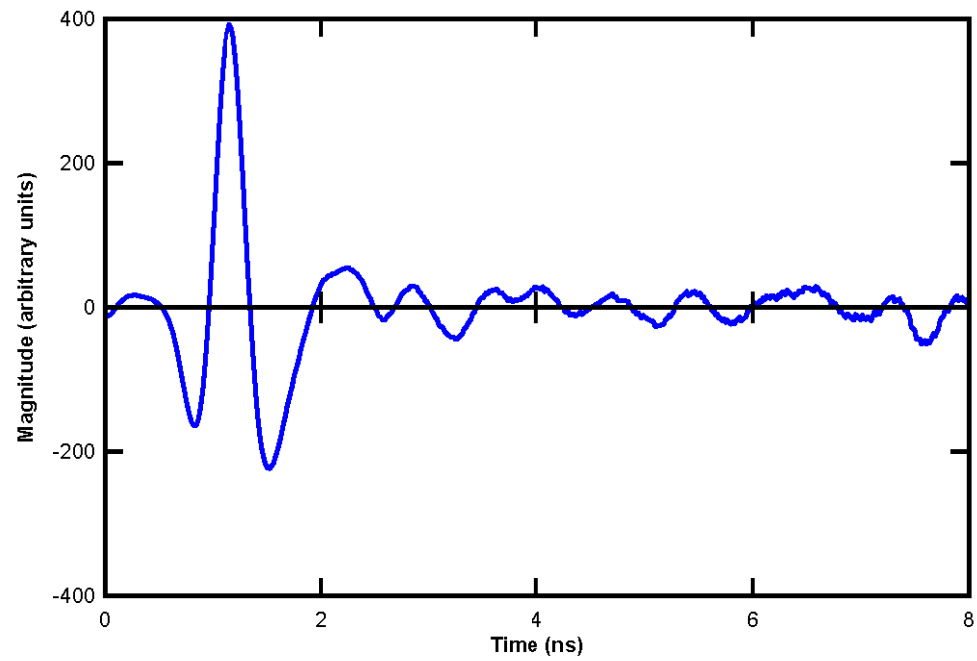


Figure 3.3 Typical GPR A-Scan.

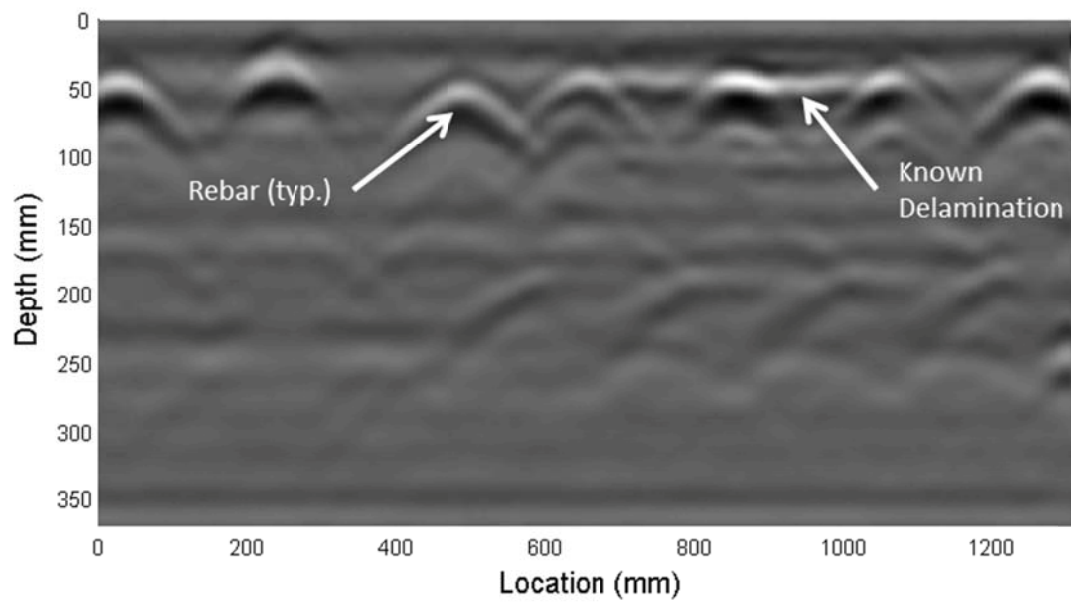


Figure 3.4 Typical GPR B-Scan.



In order to visualize GPR data collected from a bridge deck survey effectively, often the only information extracted from the recorded signals is the maximum amplitude from each A-scan. This value is then plotted as a contour map over the surveyed area<sup>18</sup>. By doing so, only very little information contained in the signal is used. Again, Matlab is used to process all of the data, and specific scripts can be seen in Appendix B.2.

#### **3.1.1.1 Issues**

The current procedure for post-processing makes B-scans (as shown in Figure 3.4) difficult to interpret.

First, reinforcing bars appear as multiple parabolic bands making the exact location, depth, and size of a rebar difficult to discern. Also, delaminations are very difficult to identify as they often don't cause a strong reflection and get lost in the signal. This is especially true when the delamination has a small width and/or it is located next to strong reflectors such as steel reinforcing bar. Also, in the next section we will show that the linear time to depth relationship shown in Equation 3.3 is not accurate when the reflectors are near the surface.

To conclude, GPR offers many advantages. However, simple B-scans are difficult to interpret since the reflections consist of several pulses each having a finite width, point reflectors are shown as parabolic shapes and smaller reflections can get lost among larger reflections. A set of post-processing procedures that lessens the difficulty of GPR interpretation is desired.

### 3.2 Equipment

The GPR device that was used in this study is the Handy Search NJJ-95B manufactured by JRC. It is a small hand-held unit shown in Figure 3.5 and is available commercially. It has a dipole antenna, with a receiver independent from the transmitter. The transmitting and receiving antenna are spaced at a horizontal distance of 39 mm (1.54 in.). The device rolls on two axles each with two wheels, of which one axle has an encoder. This encoder triggers the device to record an A-scan time signal every time the device rolls 2.5 mm (0.0984 in.). According to the manufacturer, the transmitted pulse has a center frequency at 1.3 GHz with significant amplitude content from 0.3 to 2.3 GHz. The receiver has a sampling frequency of 64 samples per nanosecond (or 64 GHz) and each signal is recorded over a total length of 8 ns.



Figure 3.5 Device used in this Study.

In order to fully understand the data gathered in the field, first more had to be understood about how and what the GPR device records. Because this device is sold commercially, much of this information is proprietary and as such not made available. In order to operate around this issue a series of lab tests have been set up to empirically determine needed information.

### **3.2.1 Surface Wave**

If the portion of the signal that is affected by the surface wave is of interest, then its effect on the signal must be estimated so that it can be removed. To estimate this affect a simple test has been performed. The device is used to scan a section of solid, unreinforced concrete that has a known thickness significantly larger than the range of the device. For this setup, it is assumed the material below the surface has no reflectors, and as such the only received signal should be the surface wave. Each A-scan along this section is averaged together creating the averaged A-scan shown in Figure 3.6. Note that not the entire transmitted signal is shown, i.e. the received signal is truncated in time at the maximum amplitude value.

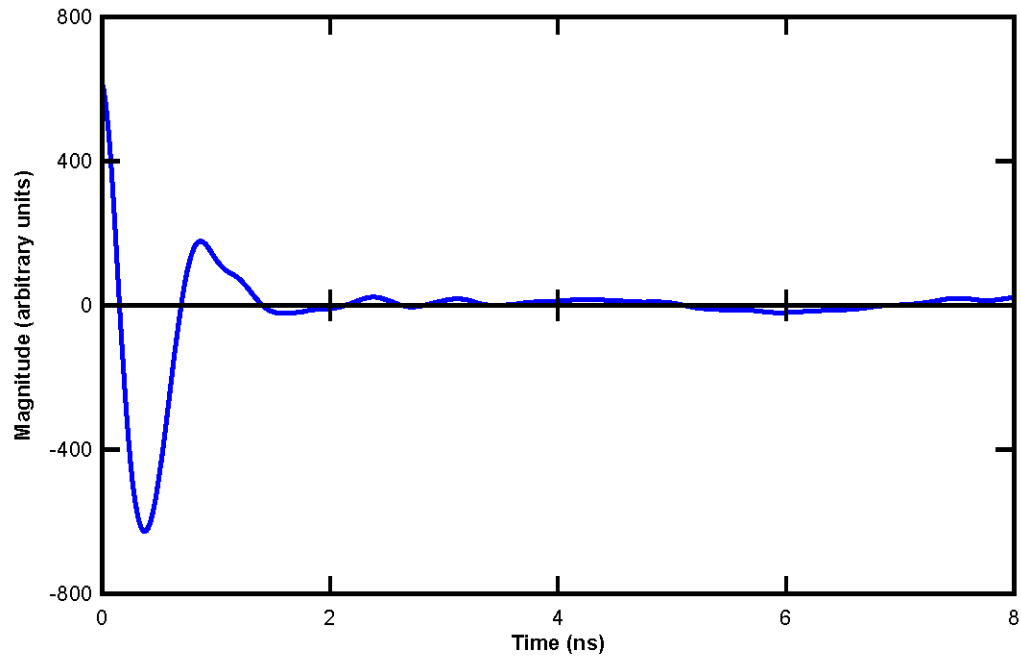


Figure 3.6 Average Concrete Surface Wave Signal.

The averaged A-scan is used to minimize the effect of noise resulting from small anomalies in the concrete section scanned. This signal is subtracted from all the data collected on concrete specimens in the lab to remove the surface wave.

### 3.2.2 Scan Angle

It is also important to know the focus of the transmitted wave of this device. Or in other words, at what angle from its center this device no longer records a reflection, both parallel and perpendicular to the scan path as shown in Figure 3.7.

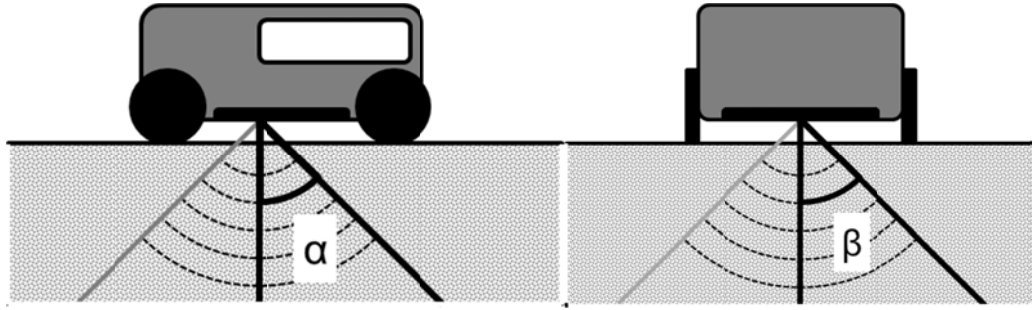


Figure 3.7 Sketch of Scan Angle both Parallel ( $\alpha$ ) and Perpendicular ( $\beta$ ) to the Path.

To determine this we setup a test with a piece of 6 mm (0.236 in.) thick plywood is elevated 133 mm (5.24 in.) above the top of a  $\varnothing$  19 mm (#6) reinforcing bar, and the rebar more than 750 mm (30 in.) above the lab floor.

To estimate the focus angle of the wave perpendicular to the scan path, one scan was recorded along the center of the plywood, perpendicular to the bar. This scan is shown in in Figure 3.8.

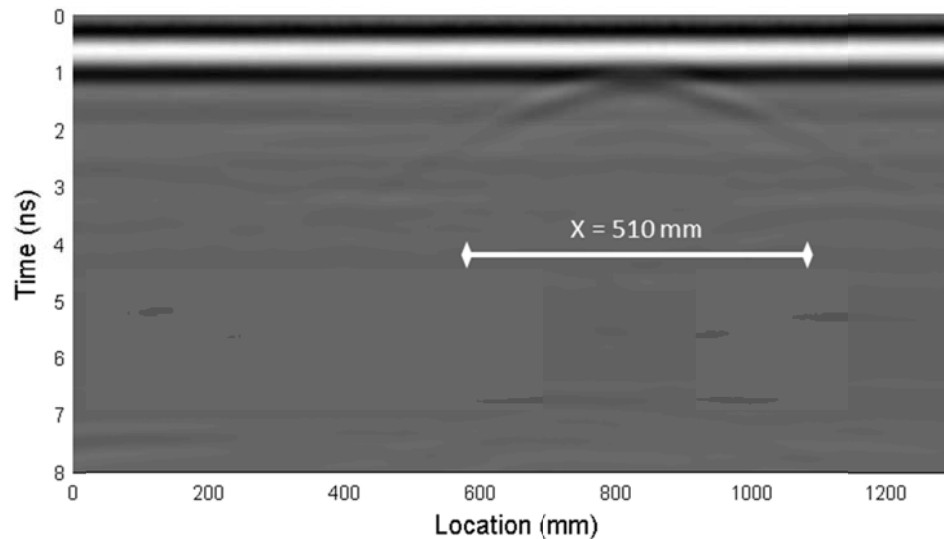


Figure 3.8 B-Scan for Parallel Scan Angle ( $\alpha$ ) Test (Case A).

Finding the distance from where the device first records a reflection from the rebar, to where the device no longer records a reflection (x). And knowing the distance from device to the top of the rebar (y), the effective focus angle is determined using Equation 3.4 to be 62 Degrees.

$$\alpha = \tan^{-1} \frac{X}{2*Y} \quad (3.4)$$

Where:

$\alpha$  = Scan angle from center of device

$X$  = Distance between first and last reflection recorded (510 mm(20 in.))

$Y$  = Distance from device to top of bar (13 mm (0.5 in.))

To estimate the focus angle of the wave perpendicular to the scan path, four scans were recorded parallel to the bar. The first scan line was located directly above the bar. The second scan was located 25 mm (1 in.) to one side of the bar; the next was 50 mm (2 in.) from the bar; and finally 75 mm (3 in.). Because this setup is symmetrically about the bar, only scans on one side were recorded. Each scan was averaged along the length of the scan, allowing the data to be shown as a simple 2-D time plot. And each averaged scan is shown in Figure 3.9.

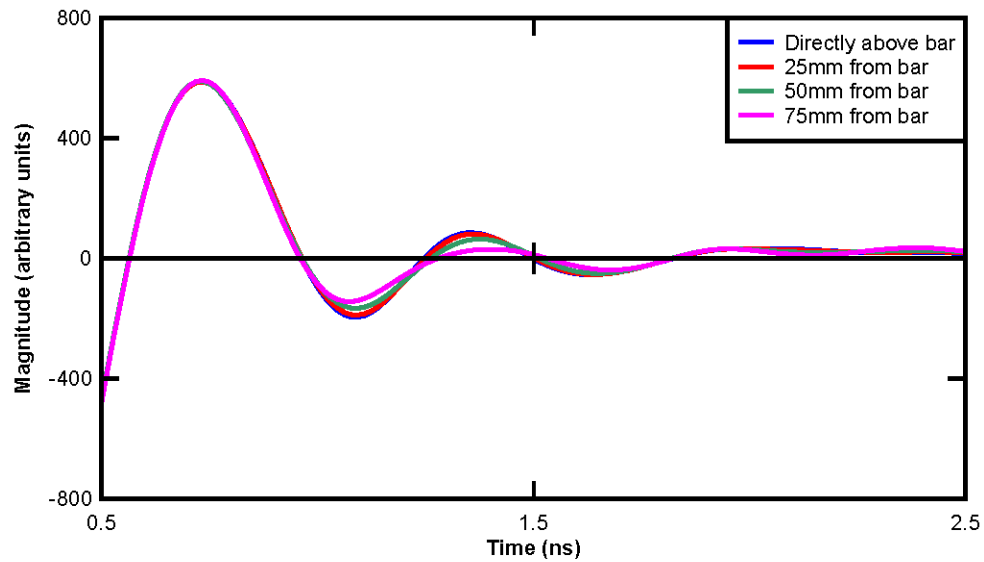


Figure 3.9 Average A-Scan for Perpendicular Scan Angle ( $\beta$ ) with Varying Distance from Bar (Case B).

Notice there is a very small difference between the scan directly over the bar and the scan 75 mm (3 in.) to the side. This means that a small amount of the pulse is actually reflected even when the device is directly above the bar. It is likely that this is because of the polarization of the transmitted pulse. It is assumed from this result that the pulse wave is polarized parallel to the scan path of the device, and thus the scan angle  $\beta$  is essentially 0.

### 3.2.3 Pulse Wave

The shape of the electro-magnetic pulse that the device transmits is also very important. Each reflection has the same shape as the originally transmitted signal, so knowing this shape is important to fully understand the recorded data. In order to determine the transmitted pulse, the following experiment has been developed. The

device is set 610 mm (24 in.) above a large steel plate, as shown in Figure 3.10. Knowing that the focus angle of the device perpendicular to the scan path,  $\beta$ , is very small the device is supported on either side, ensuring the height is consistent throughout the experiment without creating unexpected reflections. A signal is then recorded.



Figure 3.10 Setup for Pulse Test.

The only reflection recorded from this setup should be from the steel plate; and because steel reflects nearly all the energy this signal has a relatively low noise to signal ratio. It is assumed that this reflection has the same form as the originally transmitted signal.

This signal seems to match up well with the derivative of a wave known as the Ricker wave or Mexican hat wave<sup>19</sup> expressed in Equation 3.5.



$$R = \frac{d}{dt} \left( \frac{2}{\sqrt{3}\sigma\pi^{1/4}} \left( 1 - \frac{t^2}{\sigma^2} \right) e^{-\frac{t^2}{\sigma^2}} \right) \quad (3.5)$$

where:

$R$  = Derivative of the Ricker wavelet, the assumed input waveform

$t$  = Time

$\sigma$  = Variable controlling spread of the wave(determined empirically)

The reflected wave and the derivative of the Ricker wave are shown together in Figure 3.11 to show their similarity. Knowing the transmitted wave is not a simple single pulse, but in fact has multiple peaks, both positive and negative, makes pinpointing the exact location of reflections more difficult.

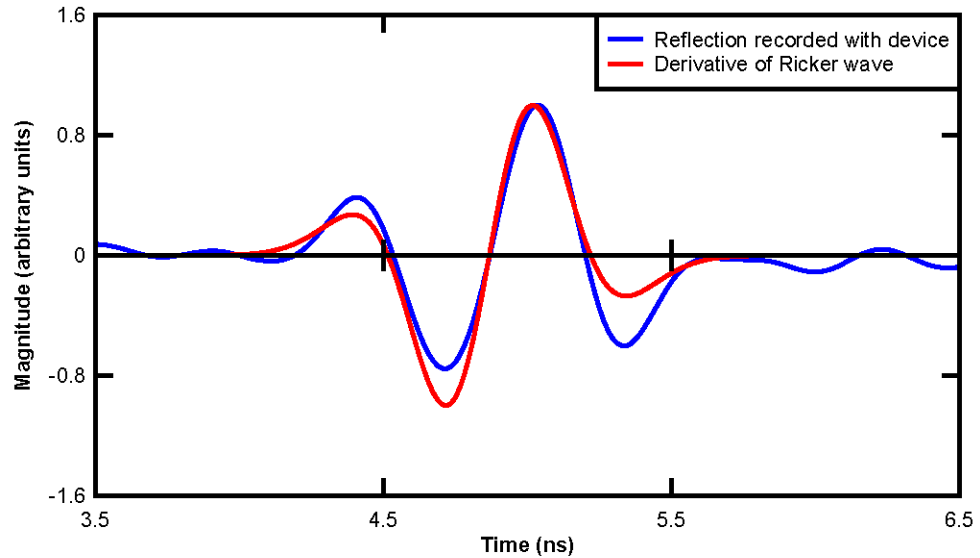


Figure 3.11 Recorded Pulse Reflection and Assumed Pulse Waveform.

### 3.3 Isolated Parameter Tests

The effectiveness of GPR to determine common bridge deck parameters were evaluated next. In order to accurately determine the effectiveness of GPR on each parameter, the presence of the other parameter must be controlled.

To isolate parameters associated with reinforcing bars, a specimen was created. This specimen is a 2.29 x 0.914 x 0.305 m (90 x 36 x 12 in. concrete block. It has 18 reinforcing bars of different sizes and clear covers and two post tensioning ducts going through the height of it. A photo of the specimen is shown in Figure 3.12.



Figure 3.12 Reinforced Concrete Specimen.

#### 3.3.1 Reinforcing Bar Size

One aspect of GPR tested, was its effectiveness to determine the diameter of an embedded bar. Because the specimen has reinforcing bars varying from (#4 to #11)

with the same spacing and clear cover, the bar diameter is an isolated parameter and should be easily evaluated by a simple scan perpendicular to the bars. Such a scan is shown in Figure 3.13.

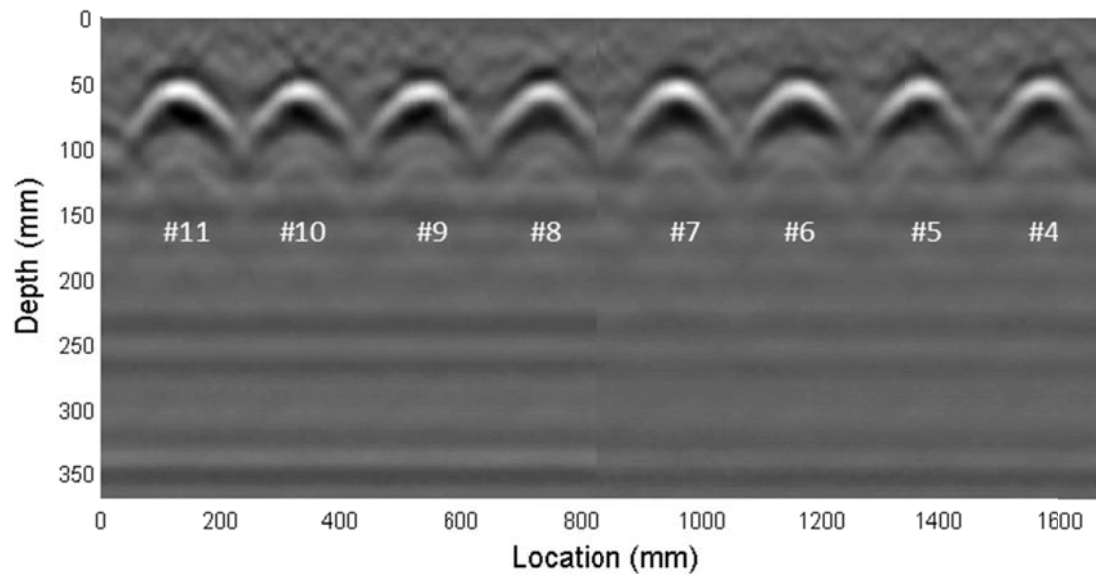


Figure 3.13 B-Scan of Reinforcing Bars with Varying Diameters.

It appears as though the parabolic shapes created by the bars are consistent for all bar diameters. This comes slightly counter-intuitively, as instinctively it would seem that a larger bar would result in a larger parabola. To clarify these results, a simple theoretical parameter study was performed. For each location of the transmitter ( $x_1$ ) shown in Figure 3.14, the distance from the transmitter to the rebar and back to the receiver was calculated geometrically.

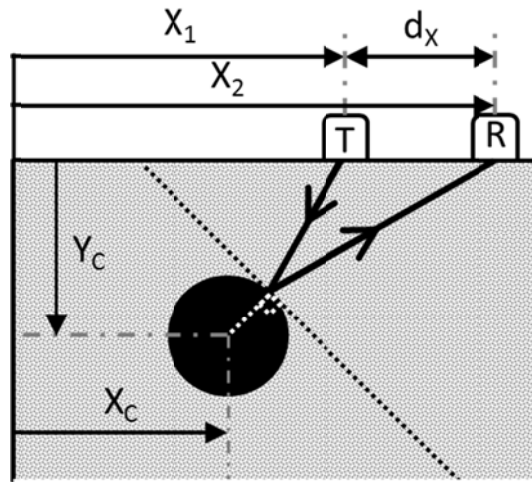


Figure 3.14 Sketch of the Travel Path of the Pulse.

This distance is equal to the distance the electro-magnetic wave travels when the bar reflection is recorded. Plotting this travel distance as a function of the location of the transmitter is an idealized case of the B-scan data that is recorded as the device is rolled perpendicular to the bar (Figure 3.14). This idealized plot is shown for an  $\varnothing$  13 mm (#4) and an  $\varnothing$  35 mm (#11) rebar with a 50 mm (2 in.) clear cover in Figure 3.15. Notice that even though the  $\varnothing$  35 mm (#11) rebar has a diameter 2.5 times larger than the  $\varnothing$  13 mm (#4) rebar, the idealized B-scans are nearly identical. Once the naturally present variability of material parameters and geometry are considered, they would be virtually indistinguishable. It should also be noted that the idealized plot shows the top of the rebar being slightly more deep than the bar itself. This is not a mistake and is due to the non-linear relationship between depth and time to be discussed later.

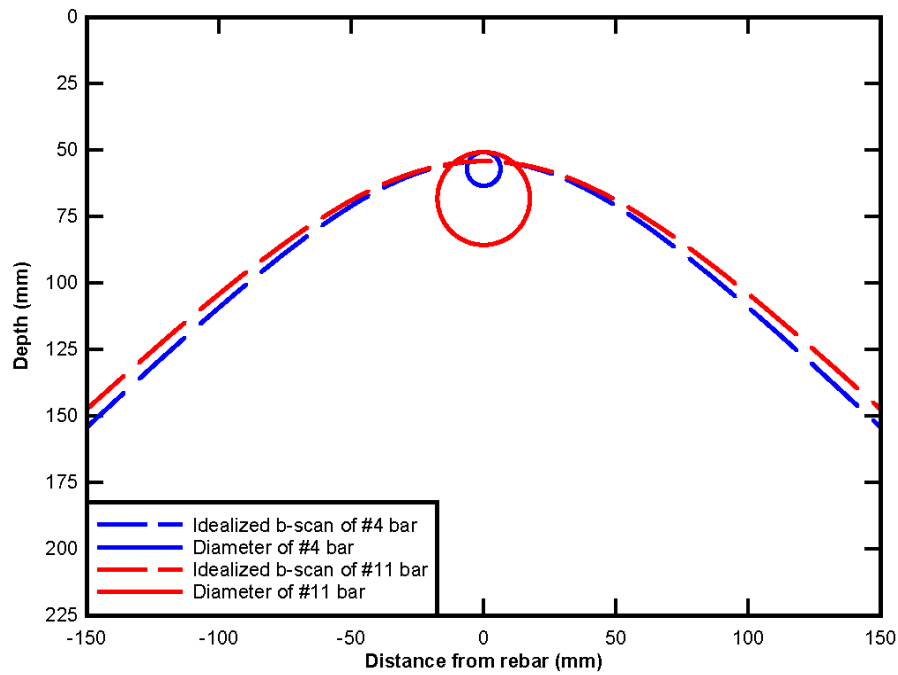


Figure 3.15 Idealized B-Scan of Reinforcing Bar and Bar Diameter.

Based on these idealized scan and results shown from the lab specimens we have concluded that simple B-scan GPR data cannot be used to predict the diameter of an embedded reinforcing bar.

### 3.3.2 Reinforcing Bar Depth

The effectiveness of GPR to determine the depth or clear cover of an embedded rebar was next evaluated. The same test specimen was again used because it also has five Ø 19 mm (#6) rebars with clear covers varying from 25 mm (1 in.) to 76 mm (3 in.). Again a simple B-scan perpendicular to the bars is all that was needed, and is shown in Figure 3.16.

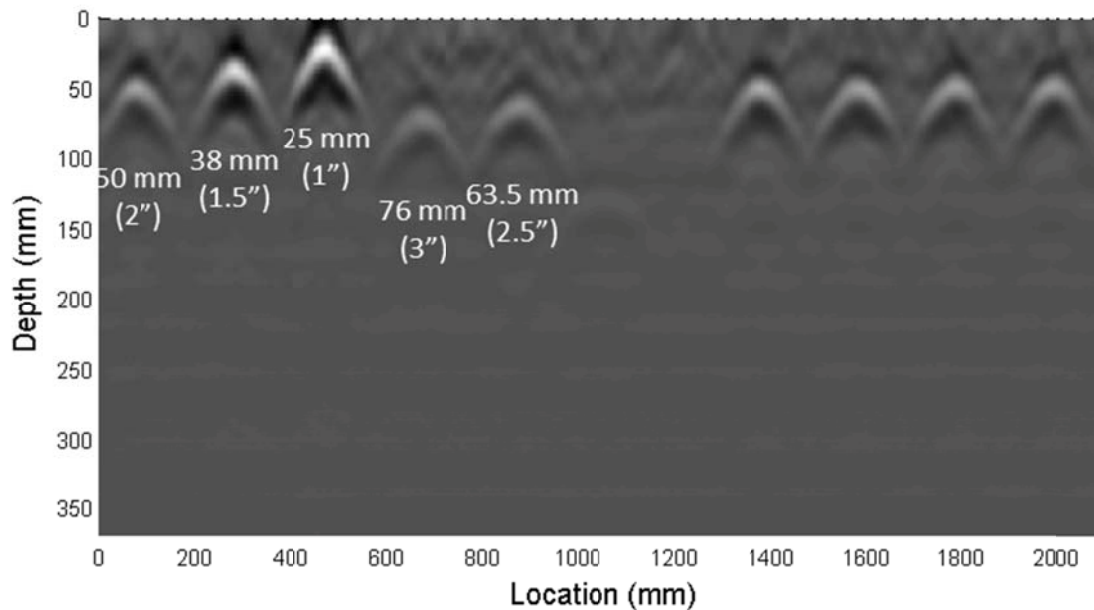


Figure 3.16 B-Scan of Reinforcing Bars with Varying Clear Covers.

If the dielectric constant of the concrete is known, then the distance to the top of the reinforcing bar can be calculated from the time associated with the peak magnitude in the scan.

In this case, the actual depths are known, so the dielectric constant can be back-calculated. To produce the smallest errors in depth prediction according to Equation 3.2, a dielectric constant of 10.5 was used. Even though this value is at the higher end of accepted values for concrete, it is not completely unexpected; the concrete was tested while it was relatively fresh. This means the concrete was still relatively moist, increasing its expected dielectric constant. Using this constant in Equation 3.3, a wave speed of 93 mm/ns (3.66 in/ns) is estimated and used for the following calculations. The depth of the rebar calculated with Equation 3.2 show

significant error. The percent error of each depth prediction compared to its known depth seems to be inversely related to the depth, as shown in Figure 3.17.

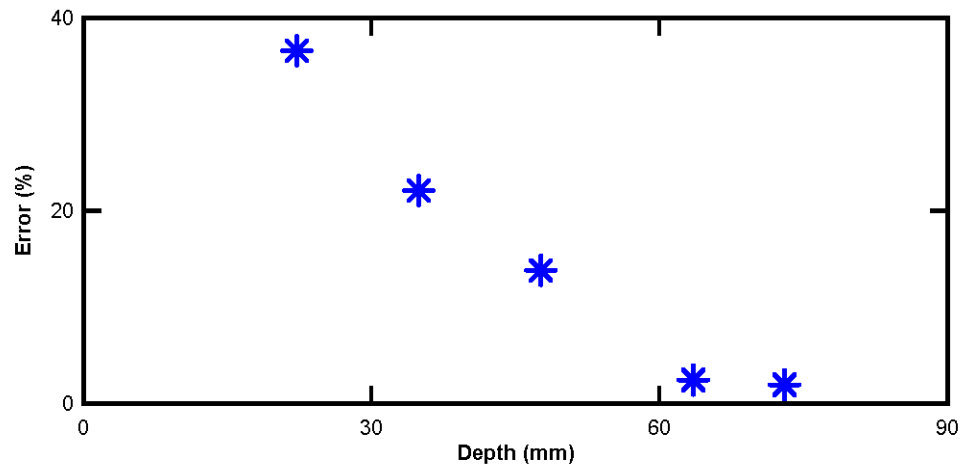


Figure 3.17 Percent Error with Varying Depths.

This suggests that the relationship between time and depth is not truly linear likely due to two factors not included in this simple analysis. One is the linear relationship assumes that the transmitter and receiver are at the same location, i.e. the total travel distance is simply two times the depth of the reflector. An adjustment must be made to account for the distance between the transmitter and the receiver. The other assumption in this analysis is that the transmitter and receiver are truly coupled directly to the surface. In reality there is a small offset ( $\sim 2\text{mm}$  ( $\sim 0.0787\text{ in.}$ )) between the device and the concrete that allows the device to roll, not slide, over the surface. Because air and concrete have different wave speeds, this alters this linear relationship. As the reflector moves farther away from the surface, both these effects

become less significant. After a depth of 60 mm (2.36 in.) the error in predicting the clear cover drops to under 5%.

### **3.3.3 Delamination Identification**

To evaluate the effectiveness of GPR to identify delaminations, a different setup was used. A 152 x 152 x 533 mm (6 x 6 x 21 in.) unreinforced, concrete beam was elevated more than one meter (40 in.) above the floor. Another identical beam was placed directly on top of it. The natural variation in the smoothness between the two adjacent surfaces leaves a very small gap ( $< 1\text{ mm}$  ( $< 0.04\text{ in.}$ )) between the bottom and top beam. This gap closely approximates the crack in a delaminated section. Test 1 takes a scan along the top of the stack of beams, and closely approximates a delamination at a 152 mm (6 in.) depth. This scan can be seen in Figure 3.18, Test 1. Test 2 is the same setup, but the gap is set to 3 mm (0.118 in.) instead of the small gap from the natural variation in the surface smoothness in Test 1. Test 3 sets the gap to 13 mm (0.5 in.) and Test 4 has a 25 mm (1 in.) gap. Test 5 removes the bottom beam creating an infinite gap. Test 6 is set up similar to Test 1 but the surfaces were wetted to simulate a saturated delamination.



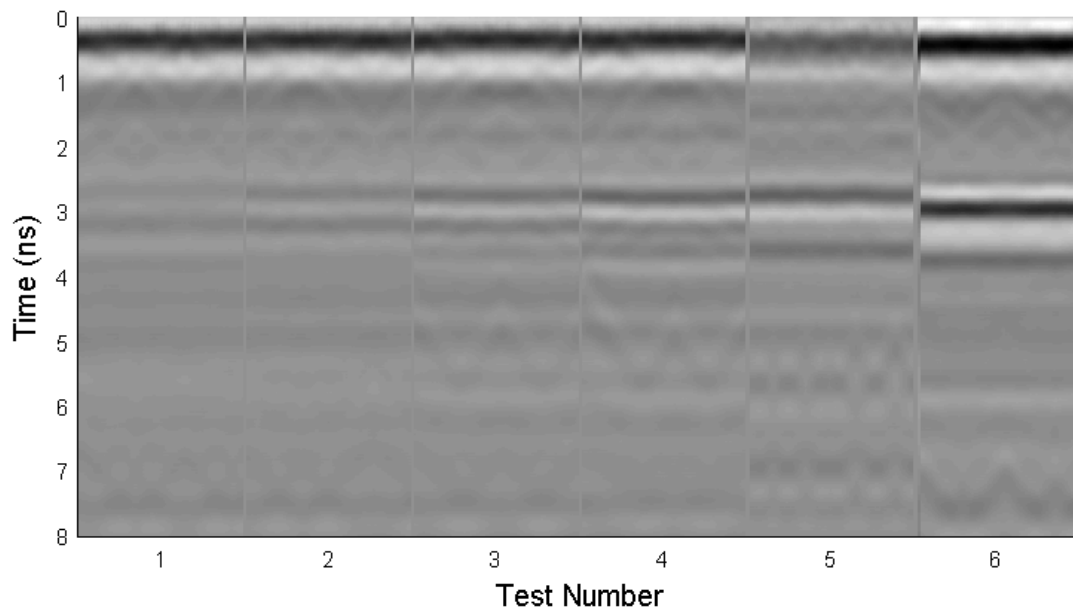


Figure 3.18 B-Scans for Delamination Tests 1 through 6.

Notice the larger the gap, the easier it is to see the reflection (near 3 ns). The reflection from the air gap in Test 1 is nearly unidentifiable. This suggests that using a B-scan to identify delaminations will be difficult unless the delamination is very significant (Tests 3 to 5) or saturated with water (Test 6).

### 3.4 Proposed Additional Post-Processing Procedures

Three new post-processing procedures have been developed for GPR data to increase its effectiveness. First, due to the use of separate antennas for transmitting and receiving pulses, the off-set which introduces a non-linear relationship between time and actual depth was considered (discussed in Section 3.3.2). The second procedure attempts to reduce the multiple peaks recorded for each reflector into one peak by using the cross-correlation function. The third procedure attempts to condense the parabolic shapes in the B-scan into a single point by employing a migration algorithm. These new procedures are highlighted in Figure 3.19.

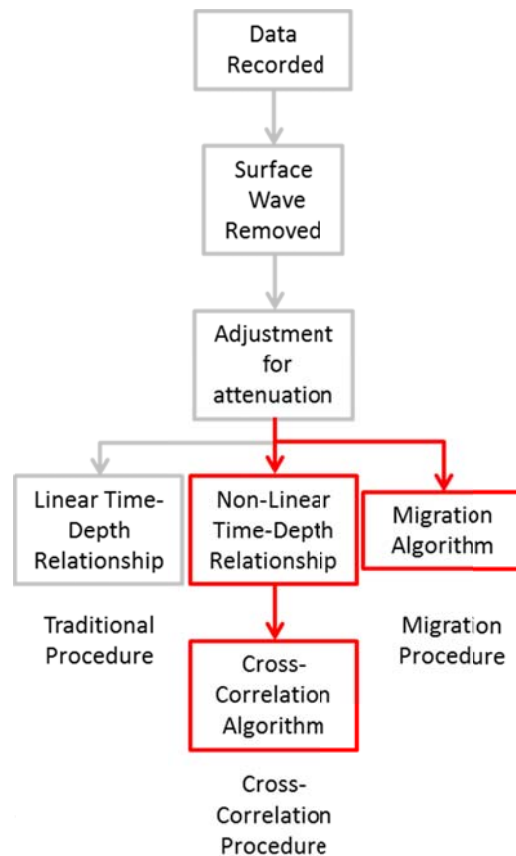


Figure 3.19 Post-Processing Procedures for GPR Data Developed in this Study (red).

### 3.4.1 Non-Linear Time-to-Depth Relationship

It was shown earlier (Section 3.3.2) that it is not always accurate to simply assume a linear relationship between the depth of the reflector and the time of flight as described in Equation 3.3. Although this assumption might work for deep reflectors, the depth prediction of reflectors near the surface will be altered (see Figure 3.17). Figure 3.20 shows the differences in assumed wave paths for the linear relationship and one that includes the device offset and transmitter to receiver distance.

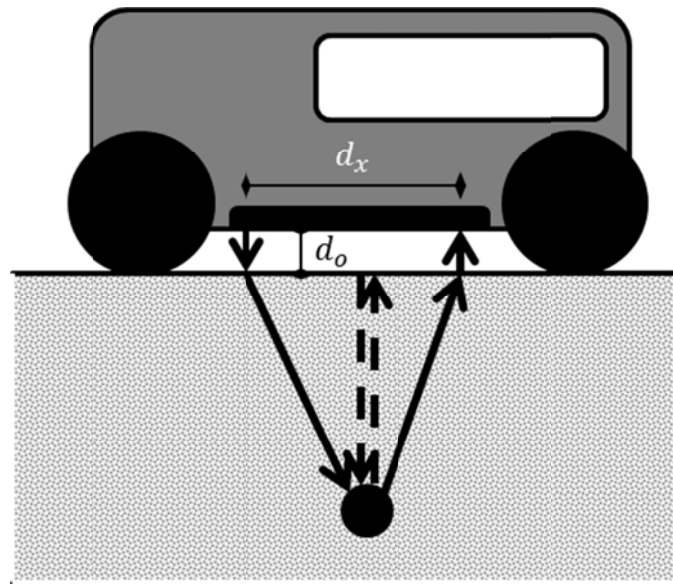


Figure 3.20 Sketch of Assumed Pulse Wave Path for Linear (dotted line) and non-linear (solid line) Relationship.

This means it is inaccurate to linearly transform the time axis of B-scans to depth by simply multiplying the time by half the wave speed (Equation 3.3). A more accurate relationship between time and depth should be assumed by accounting for the

distance between the transmitter and receiver, and the offset from device to the concrete. This relationship is shown in Equation 3.6.

$$D = \sqrt{\left[\left(\frac{t}{2} + \frac{d_o}{2 \cdot c_o}\right) C_{conc}\right]^2 - \left(\frac{d_x}{2}\right)^2} \quad (3.6)$$

where:

$D$  = Depth to reflector

$C_{conc}$  = Wave speed through concrete (Eqn. 3.1)

$t$  = Time of flight from transmitter to reflector and back

$d_o$  = Distance from transmitter surface (2 mm (0.0787 in.))

$d_x$  = Distance from transmitter to reciever (this device) (39 mm (1.54 in.))

$C_{air}$  = Speed of light ( $0.3 \frac{m}{ns}$  (11.8 in/ns))

Although this geometry still does not exactly match the wave path, it gives a closer approximation. Its effectiveness can be seen when the percent error of the bar depths calculated with the two methods are compared as shown in Table 3.2. Notice the nonlinear relationship from Equation 3.6 has significantly smaller errors, especially at shallow depths. These are solely due to the fact that the small air gap is neglected and the travel path in the air is assumed vertical as shown in Figure 3.20. Also, the magnitudes of the errors are relatively consistent for all depths.

Table 3.2 Actual, Linearly Calculated, and Non-Linearly Calculated Clear Cover.

Actual Cover (in)	Calculated Cover (in)			
	Traditional Linear Relationship	(% Error)	Proposed Non-Linear Relationship	(% Error)
0.875	1.20	(37%)	0.87	(1%)
1.375	1.68	(22%)	1.46	(6%)
1.875	2.13	(14%)	1.96	(4%)
2.5	2.56	(2%)	2.41	(4%)
2.875	2.93	(2%)	2.80	(3%)

### 3.4.2 Migration Algorithm

Another issue with traditional GPR analysis is that single point reflectors like reinforcing bars are shown in B-scans as parabolas as discussed earlier. This can be misleading, especially to an untrained eye. This is not new, and many algorithms have been developed to handle this issue<sup>17</sup>. One common technique used to consolidate these parabolas is known as Hagedoorn Migration<sup>20</sup>. An algorithm similar to Hagedoorn Migration has been developed within this study to post process the GPR data. This algorithm assigns each location in the scanned material to a matrix. Each row in the matrix represents the depth into the material, and each column represents the location of each A-scan performed. For each A-scan, the distance from the transmitter to each point represented in the matrix and back to the receiver is calculated. That distance is transformed, using an assumed wave speed and adjusting for the distance traveled between the device and the surface, into a time. The magnitude of the A-scan at that calculated time is then assigned to the value at that location in the matrix. This is repeated for each A-scan, with every new magnitude being added to the previous value in the matrix. The equation used for a given location in the matrix is expressed in Equation 3.7.

$$M_{i,j} = \sum_{k=1}^n f_k \left[ \left( \sqrt{\left[ (i * x_s) - (k * x_s - \frac{dx}{2}) \right]^2 \left[ j * \frac{C_{conc}}{S} \right]^2} + \sqrt{\left[ (i * x_s) - (k * x_s + \frac{dx}{2}) \right]^2 + \left[ j * \frac{C_{conc}}{S} \right]^2} \right) \left( \frac{1}{C_{conc}} \right) - \left( 2 \frac{d_o}{C_o} \right) \right] \quad (3.7)$$

where:

$M_{i,j}$  = Value at location  $i, j$

$i$  = Pixel index indicating its location along the scan path

$j$  = Pixel index indicating its depth below the surface

$f_k(t)$  = The value of the  $k^{th}$  A – Scan at time,  $t$

$x_s$  = Spacing between A – Scan signals (2.5 mm (0.0984 in.))

$C_{conc}$  = Wave speed through concrete (Eqn. 3.1)

$S$  = Number of samples recorded per nanosecond (64 Samples/ns)

$d_x$  = Distance from transmitter to receiver (39 mm (1.54 in.))

$C_{air}$  = Speed of light ( $0.3 \frac{m}{ns}$  (11.8 in./ns))

This algorithm essentially transforms peaks in each A-scan into 2 dimensional semi-circles. Each set of semi-circles ends up being averaged over the entire B-scan. This allows constructive interference between semi-circles to focus on the point reflector, while destructive interference to remove noise. An illustration of this procedure is shown in Figure 3.21 where each A-scan consists of a single reflection

from the rebar shown in the solid black line, and the dotted black line shows the semi-circle created with the algorithm.

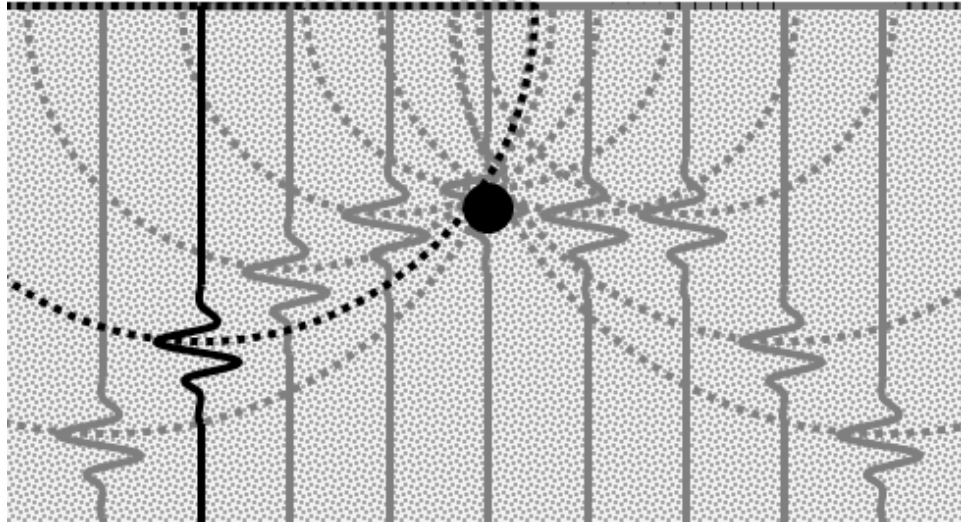


Figure 3.21 Sketch of Migration Algorithm.

### 3.4.3 Cross-Correlation Algorithm

The transmitted pulse has multiple peaks that penetrate the material. This causes each reflector to produce multiple peaks that even the migration algorithm does not reduce. In order to isolate each reflection into one peak a specialized algorithm has been developed. In this algorithm each A-scan signal is cross-correlated with the transmitted pulse. Cross-correlation gives a measure of how similar two time series are to each other at any given time lag and is shown in Equation 3.8<sup>21</sup>.

$$R_{xy}(n) = \sum_{m=-\infty}^{\infty} X(n+m) * Y^*(m) \quad (3.8)$$

where:

$R_{xy}$  = Cross – correlation of  $X$  and  $Y$

$X$  = Recorded GPR signal

$Y^*$  = Complex conjugate of the estimated input function

Cross-correlating the pulse signal with the A-scan signal gives a maximum value where the A-scan is most similar to the pulse signal. The location of the maximum cross-correlation value is found in the A-scan signal, and that value and location is stored. The pulse signal normalized to that point is subtracted from the A-scan signal. This process is repeated with this new A-scan signal and the value with its location is stored as the next point. It is repeated for a total of 10 times for each A-scan. The 10 points stored are plotted according to their stored location, with all other locations set to zero. Now instead of having a signal with multiple peaks per reflection, there is a signal with 10 points that are most similar to the input signal and thus the 10 most likely reflections.



### **3.5 Bridge Deck Specimen Tests**

Now that there is a more robust post-processing procedure in place to maximize GPR's abilities, it can be applied to more complicated structures for evaluation. Subsequently, GPR testing was performed in two experiments using reinforced concrete lab specimens as described in the following sections. Finally, the abilities of these post-processing techniques are discussed.

#### **3.5.1 Delaminations**

The first experiment scans a section of a specimen created to mimic a typical bridge deck. The first half of the scan was over a solid reinforced section. The second half of the scan has a known delamination just above the top layer of reinforcing bars. This B-scan is shown in Figure 3.22, along with a sketch of the specimen scanned showing the reinforcing bars and known delamination.

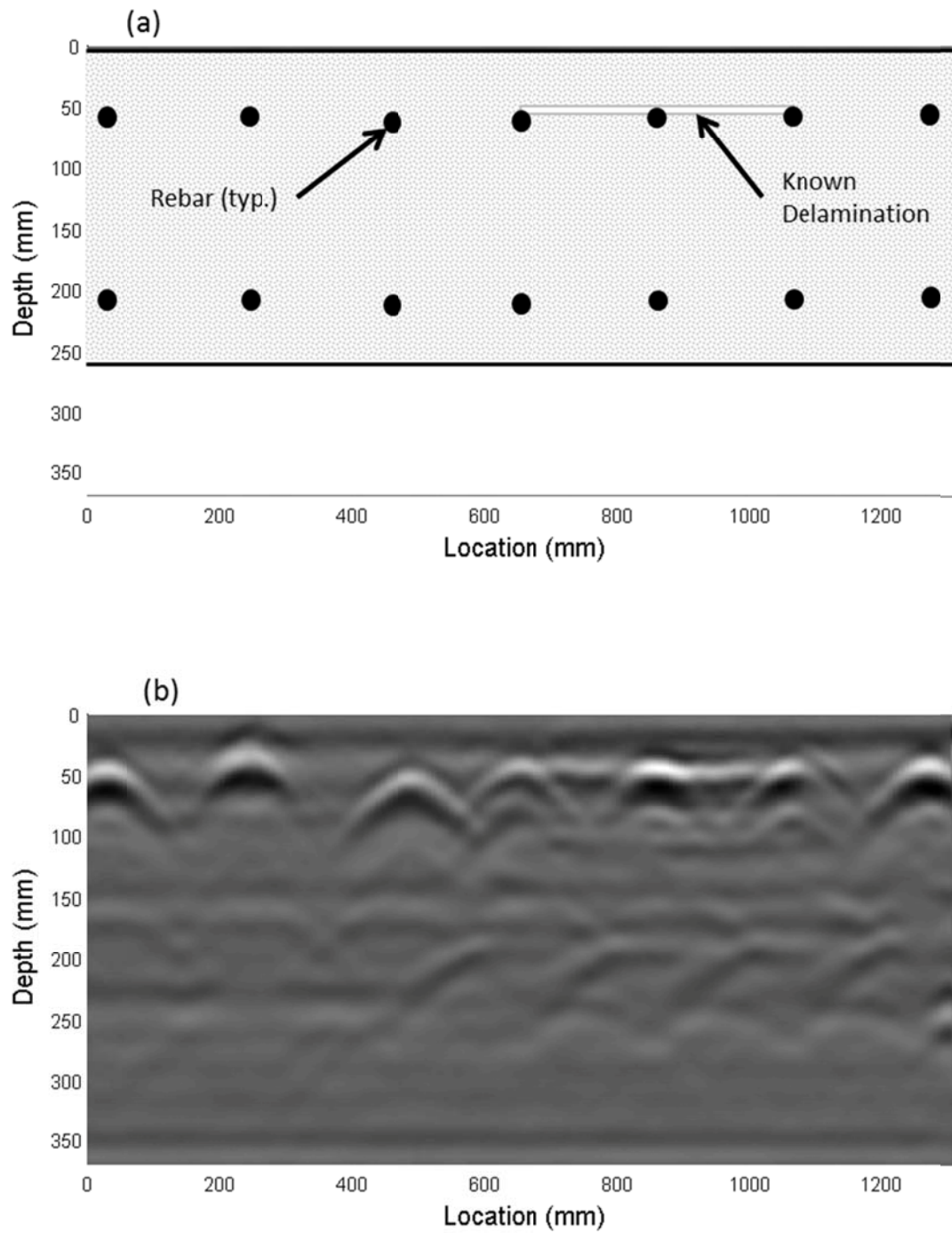


Figure 3.22 Delaminated Section (a) Sketch and (b) Traditionally Processed B-Scan Using the Linear Time-Depth Relationship.

From the B-scan alone it is difficult to identify the delamination, although there is a visible reflection connecting the reinforcing bars at the correct location.

When this data is post-processed with the cross-correlation procedure, the delamination is easier to observe. This can be seen in Figure 3.23. The first (left) half of the figure shows the outline of three parabolic shapes we would expect from steel rebars within a solid section. The second (right) half, however, shows a solid line at the expected location of the delamination, showing there is something other than just the reinforcing bars.

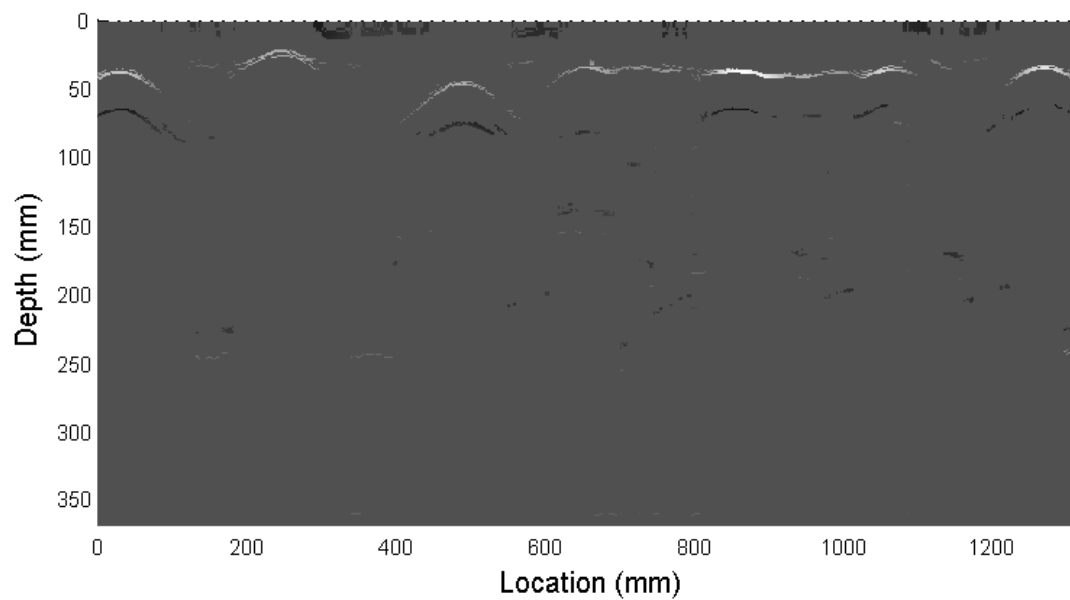


Figure 3.23 B-Scan Data Post-Processed with Cross-Correlation Procedure Using the Non-Linear Time-Depth Relationship.

### 3.5.2 Slab Thickness

An evaluation of GPR's ability to predict the thickness of bridge decks was performed. For this, two halves of the specimen shown in Figure 3.24 were scanned. Each half has a reinforcing mesh at the top, but one has a thickness that varies linearly from 51 mm (2 in.) to 279 mm (11 in.) and the other one has a thickness that varies in four, 76 mm (3 in.) steps.



Figure 3.24 Plan View of Specimen Scanned.

To evaluate the limits of GPR thickness predictions, a B-scan was performed along the length of the linearly varying and the stepped section of this specimen. These scans can be seen in Figure 3.25.

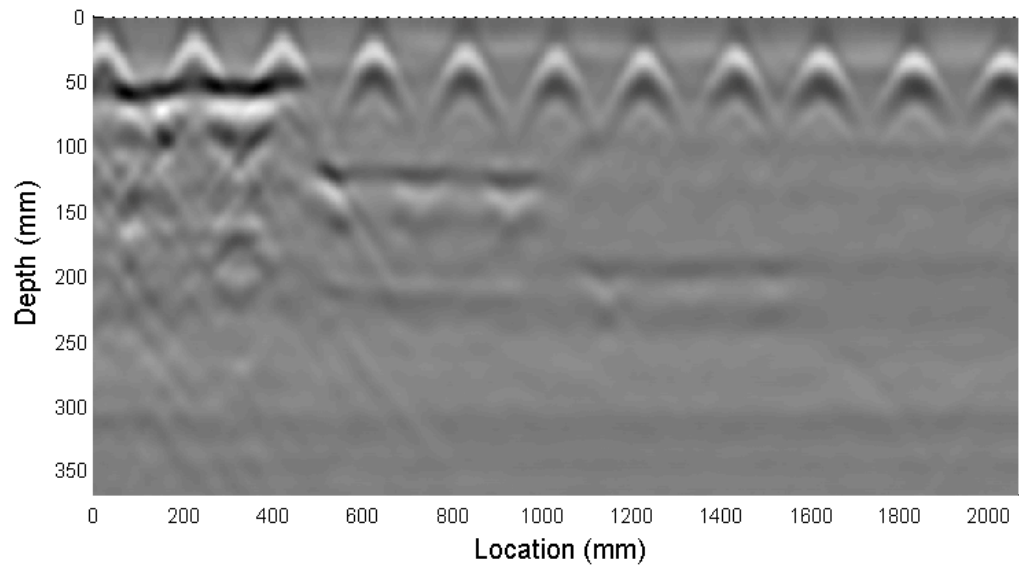
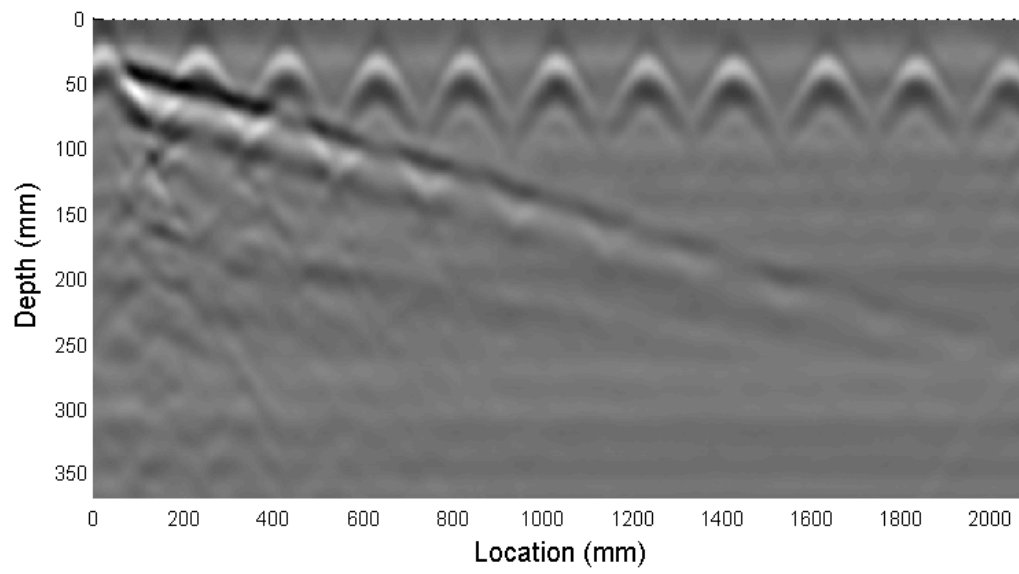


Figure 3.25 Traditional B-Scan of Slabs with Linearly Varying Thickness (top) and Thickness Varying in Steps (bottom).

Notice the back wall reflection is clearly present when the thickness is shallow, to the left of the scan, but as the thickness increases the reflection becomes weaker. This is due to the attenuation of the signal. The back wall reflection becomes indistinguishable near 4.5 ns, which correlates to about 220 mm (8.7 in.). The step thickness shows a similar trend. The 76 mm (3 in.) and 152 mm (6 in.) reflection can clearly be seen on the left of the scan. The 229 mm (9 in.) thickness reflection is barely noticeable, and the 305 mm (12 in.) reflection is not visible.

It is also clear that the back wall reflection is shadowed by the reinforcing bars, which is the main reason why the deeper reflections are not visible. The closer the bars are spaced the more the back wall will be shadowed. Based on these results it can be concluded that the thickness of bridge decks can be accurately predicted up to a thickness of approximately 203 mm (8 in.) for reinforcing bars spaced at 203 mm (8 in.) using a simple B-scan. Because typical bridge deck thicknesses range from 152 mm (6 in.) to 305 mm or more, and bar spacing could be smaller than 203 mm (8 in.) this method of GPR is not an effective means for bridge thickness predictions.

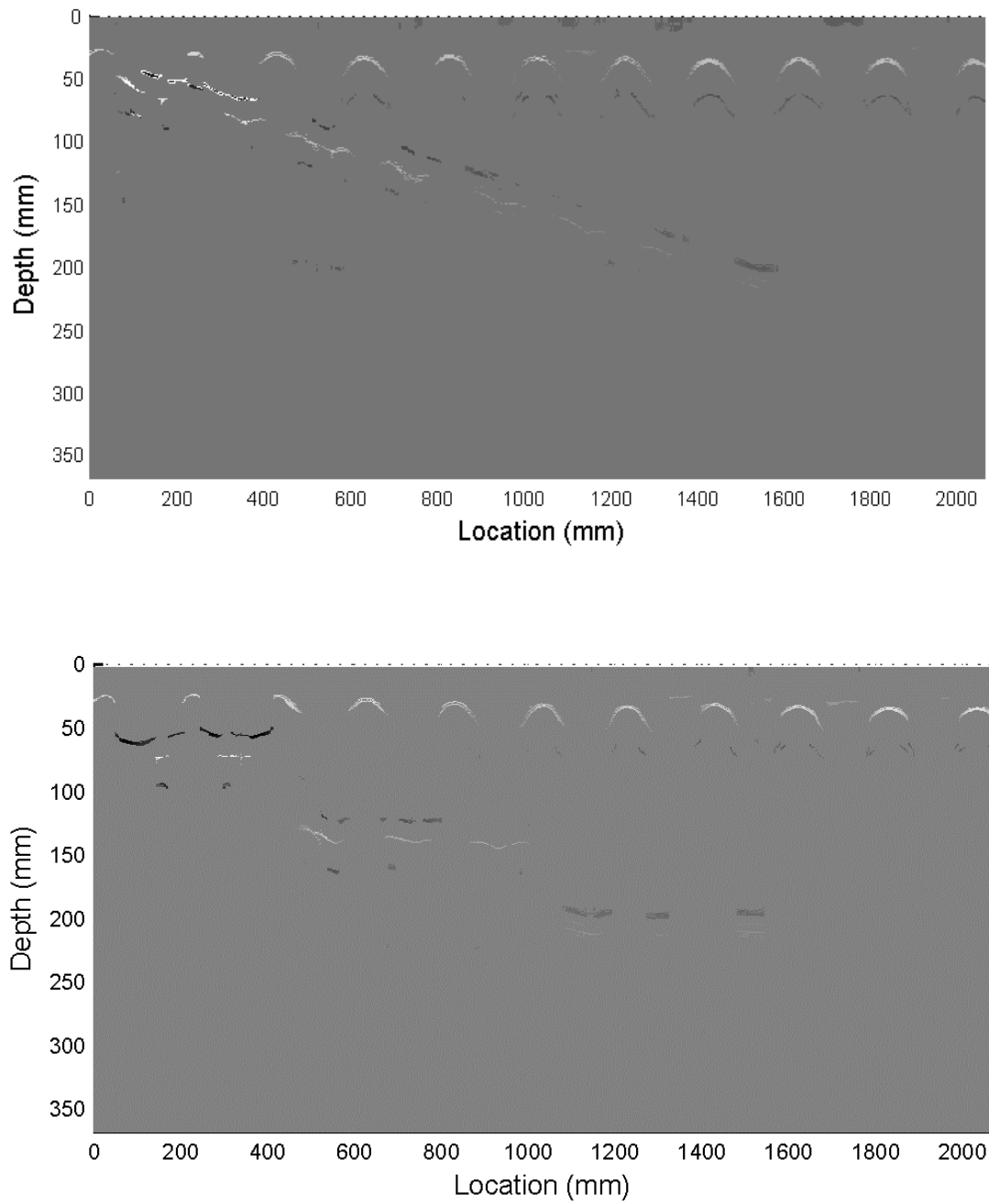


Figure 3.26 Cross-Correlation Procedure of B-Scan Data of Slabs with Linearly Varying Thickness (top) and Thickness Varying in Steps (bottom).

However when the cross-correlation algorithm is applied, things become a little clearer as shown in Figure 3.26. Although the reinforcing bars still shadow the thickness reflection.



### 3.6 Discussion

From the theoretical and laboratory results of this study the following conclusions can be made about using this GPR device as a form of NDT to characterize typical concrete bridge decks:

- It has been theoretically shown that reinforcing bar diameters cannot directly be estimated from data single B-scan.
- Using a linear relationship between time and depth is not appropriate for shallow reflectors ( $< 60\text{mm}$  (2.4 in.)). For these depths the distance from the device to the surface, and the distance between transmitter and receiver must be accounted for using the proposed non-linear relationship.
- Using the correct non-linear time to depth relationship and wave speed, clear cover of reinforcing bars can be accurately picked from the B-scan data.
- Section thicknesses can be estimated up to 200 mm (6 in.), anything thicker than that is difficult to predict due to the shadowing effect of typical reinforcing configurations in bridge decks.
- Estimation of depths or thicknesses below the reinforcing mesh is directly influenced by the spacing of the reinforcing bars.
- It may be difficult to detect delaminations with small separations without any other information.
- Use of post-processing algorithms can greatly simplify the interpretation of GPR data.

It is important to note that these conclusions are only valid for this specific device. There is still work to be done studying how different devices with different properties might affect these conclusions. Also, more work fine tuning the post-processing algorithms needs to be done. The exact input wave form (or a better estimate) would help the cross-correlation algorithm. A looking to some combination of algorithms might also be beneficial to making these results are clear as possible. A theoretical study, including model simulations, to confirm these results would also be important. Finally, the proposed procedures should be evaluated in the field.

## **Chapter 4**

### **CONCLUSION**

From the discussion of Impulse Response (IR) and Ground Penetrating Radar (GPR), it can be concluded that both methods have their strengths and weaknesses. IR is a method that can quickly give a rough estimate of delamination presence and extents. In order to test a bridge deck within a reasonable time frame, a 2 foot gird must be used. This means that flaws smaller than 2 feet might not be picked up with this method. After looking at contour plots of all four parameters specified in the ASTM Standard (and possibly some new parameters developed in this research), a good estimate of deteriorated areas can be achieved. It should be kept in mind however, that support conditions may skew the results collected with IR. Also, these results will only show the extents of the delaminations, and give no indication of the depth.

Conversely, GPR data collected by a small commercially available hand-held device, like the one used for this evaluation, will give much more precision. However, it takes time to achieve this precision. GPR works very well for detecting reinforcing bars and quantifying their clear covers, but delaminations are more difficult to identify. Even with the proposed additional post-processing techniques, it is not feasible for GPR to clearly indicate a delamination, without first having an idea of its location and extents. Though, once a delamination is located, its depth can be estimated using GPR.

Because these two methods have different strengths, it seems logical to combine them. It is recommended to first survey the entire bridge deck with IR testing, identify areas of concern, and then revisit those areas with GPR. Because there is already some idea of where the delaminations lie, it becomes easier to interpret the GPR data to pinpoint the extents and depths of these defects.

More research needs to be performed to evaluate exactly how effective this combination of methods would work on actual bridge decks. But this discussion concludes that this could be a great alternative to the subjective techniques used today.

## REFERENCES

1. Arndt, R.W., et al., Strategies for maintenance of highway bridges in the U.S. - with the support of non-destructive testing and structural health monitoring. Bautechnik, 2011. **88**(11): p. 793-804.
2. Neville, A.M., *Properties of Concrete*. 1996: Wiley.
3. Manning, David G., and Frank B. Holt. "Detecting delamination in concrete bridge decks." Concrete International 2.11 (1980): 34-41.
4. Discussion; ACI Convention, Spring 2012.
5. Davis, A.G., The nondestructive impulse response test in North America: 1985-2001. NDT & E International, 2003. 36(4): p. 185-193.
6. ACI, ACI 228.2R-98: Nondestructive Test Methods for Evaluation of Concrete in Structures. 2004, American Concrete Institute: Farmington Hills, MI.
7. Sansalone, M.J. and W.B. Streett, Impact-Echo - Nondestructive Evaluation of Concrete and Masonry. 1997, Ithaca, NY: Bullbrier Press.
8. Zhu, J. and Popovics, J., "Imaging Concrete Structures Using Air-Coupled Impact-Echo," Journal of Engineering Mechanics 2007 133:6, 628-640
9. C. C. Kennedy and C. D. P. Pancu, "Use of vectors in vibration measurement and analysis." J. Aeronaut. Sci. 14, pp. 603-625 (1947).
10. R. T. Stain, "Integrity Testing" Civil Engineering, pp. 53-59 (1982)
11. J. S. Higgs and S. A. Roberston, "Integrity of Concrete Piles by Shock Method", Concrete, 13, pp. 31-33 (1979).
12. B. H. E. Hertlein and A. G. Davis, "Non-destructive Testing of Concrete Pavement Slabs and Floors with the Transient Dynamic Response Method." Proc. Int. Conf. Struct. Faults Repair (1987)

13. N. S. Ottosen, M. Ristinmaa, and A. G. Davis, "Theoretical Interpretation of Impulse Response Tests of Embedded Concrete Structures." J. Engineering Mechanics 130, pp.1062-1071 (2004).
14. ASTM, C1740-10: Standard Practice for Evaluating the Condition of Concrete Plates Using the Impulse-Response Method, ASTM International: West Conshohocken, PA.
15. D. J. Clem, J. S. Popovics, T. Schumacher, T. Oh, S. Ham and D. Wu, "Understanding the Impulse Response Method Applied to Concrete Bridge Decks" Conference Proceedings QNDE, 2012.
16. Clemeña, G. "Nondestructive Inspection of Overlaid Bridge Decks with Ground Probing Radar," Transportation Research Record No. 899, Transportation Research Board, Washington, D.C., 1983, pp. 21-32.
17. Bungey, J. H., and Millard, S. G. "Radar Inspection of Structures," Proceedings, Institute of Civil Engineers, Structures and Buildings Journal (London), V. 99, May, 1993, pp. 173-186.
18. ASTM, D6087-08: Standard Test Method for Evaluating Asphalt-Covered Concrete Bridge Decks Using Ground Penetrating Radar, ASTM International: West Conshohocken, PA.
19. Brinks, Ralph. "On the convergence of derivatives of B-splines to derivatives of the Gaussian function." Comp. Appl. Math 27.1 (2008): 79-92.
20. Hagedoorn, J. G. "A process of seismic reflection interpretation," Geophysical Prospecting, 06, 1954, pp.449-453.
21. Orfanidis, S.J., Optimum Signal Processing. An Introduction. 2nd Edition, Prentice-Hall, Englewood Cliffs, NJ, 1996.

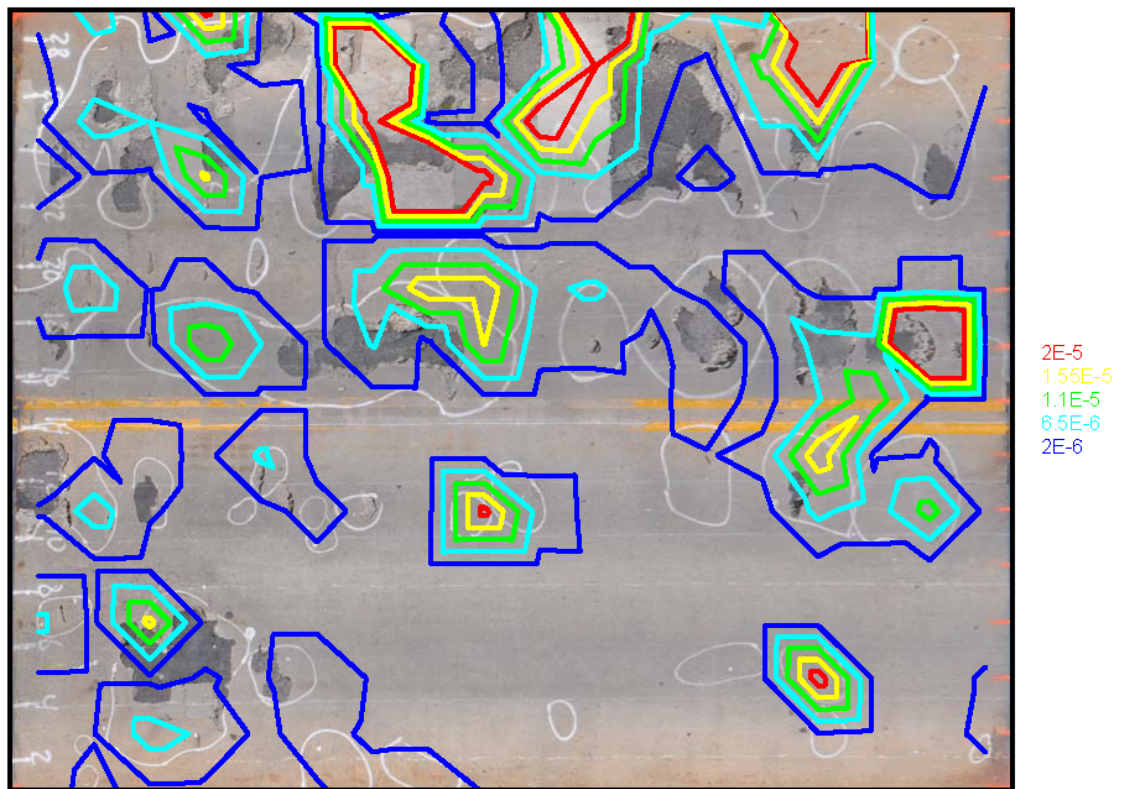
## Appendix A

### IMPULSE RESPONSE FIELD TEST CONTOUR PLOTS

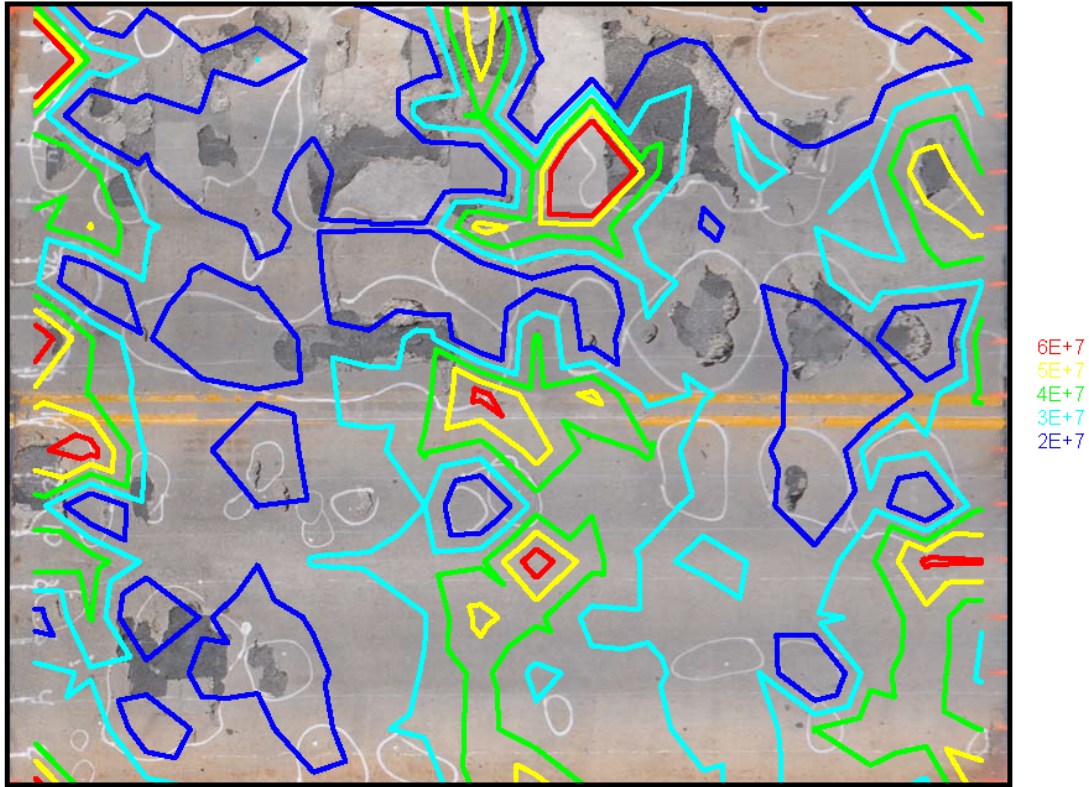
#### A.1 Branchport Bridge

##### A.1.1 Deck #1

Branchport Bridge; Deck #1  
Average Mobility  $((m \cdot s^{-1})/N)$

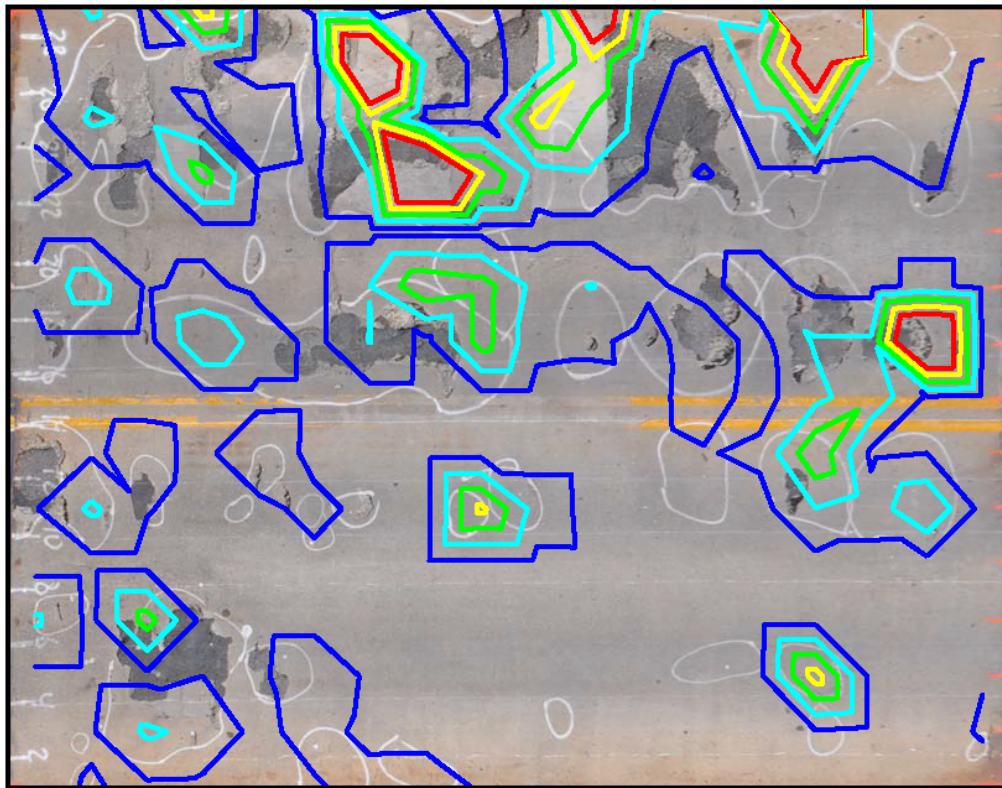


Branchport Bridge; Deck #1  
Dynamic Stiffness (N/m)



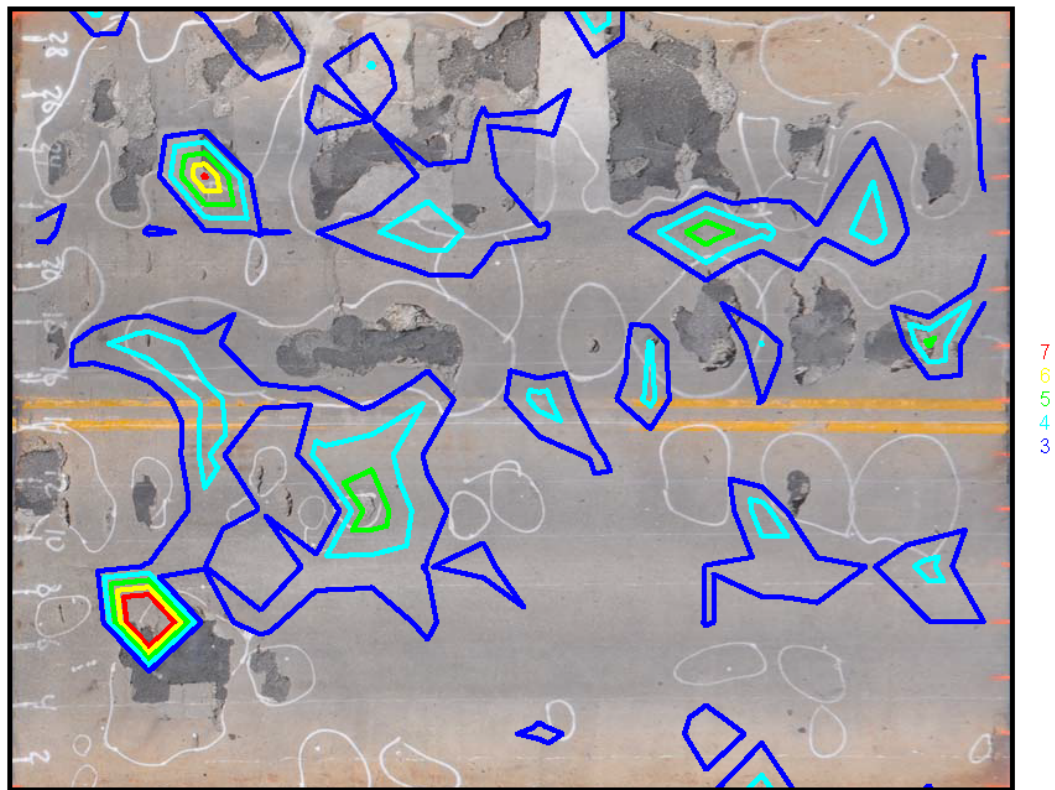


Branchport Bridge; Deck #1  
Mobility Slope (m/N)



5E-8  
3.875E-8  
2.75E-8  
1.625E-8  
5E-9

Branchport Bridge; Deck #1  
Peak Mean Ratio

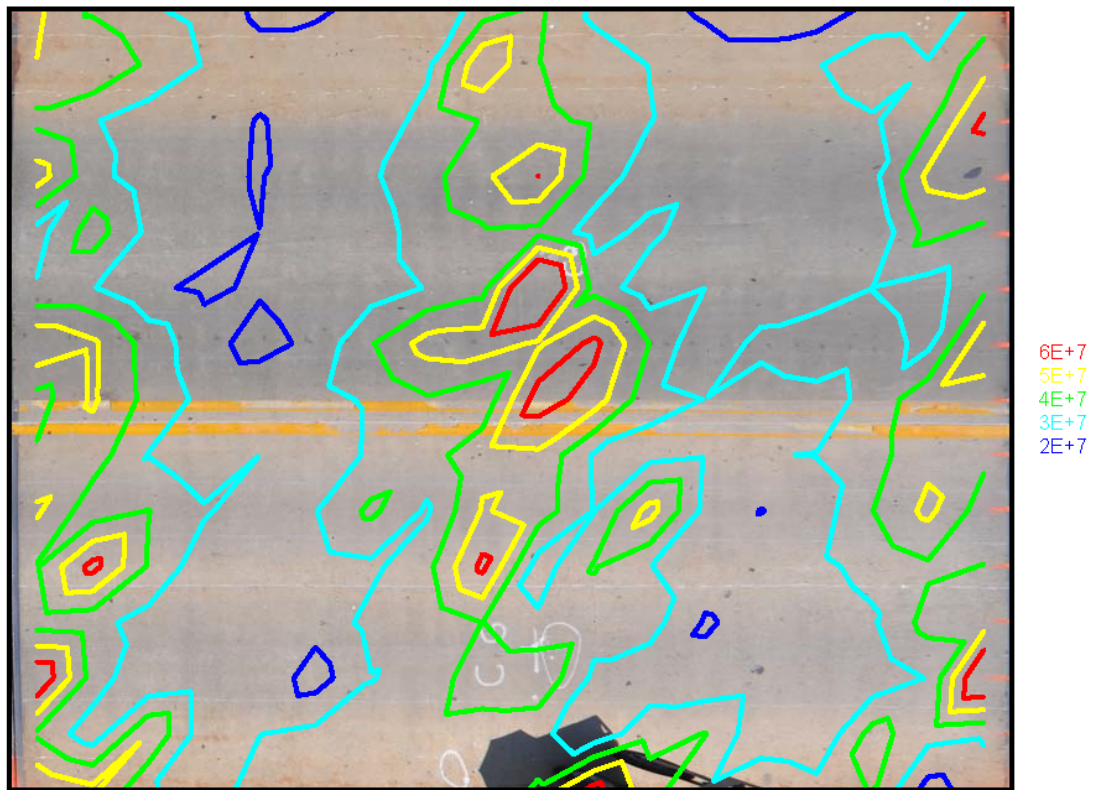


### A.1.2 Deck #2

Branchport Bridge; Deck #2  
Average Mobility ((m\*s<sup>-1</sup>)/N)



Branchport Bridge; Deck #2  
Dynamic Stiffness (N/m)



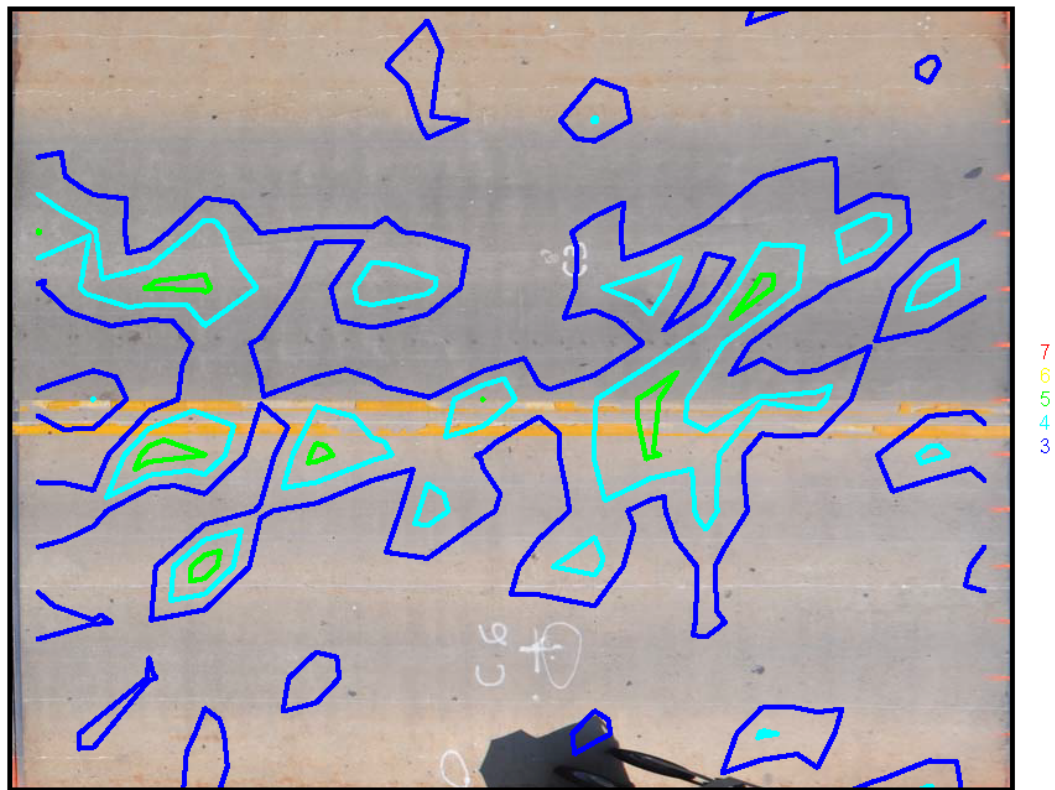
Branchport Bridge; Deck #2  
Mobility Slope (m/N)



5E-8  
3.875E-8  
2.75E-8  
1.625E-8  
5E-9

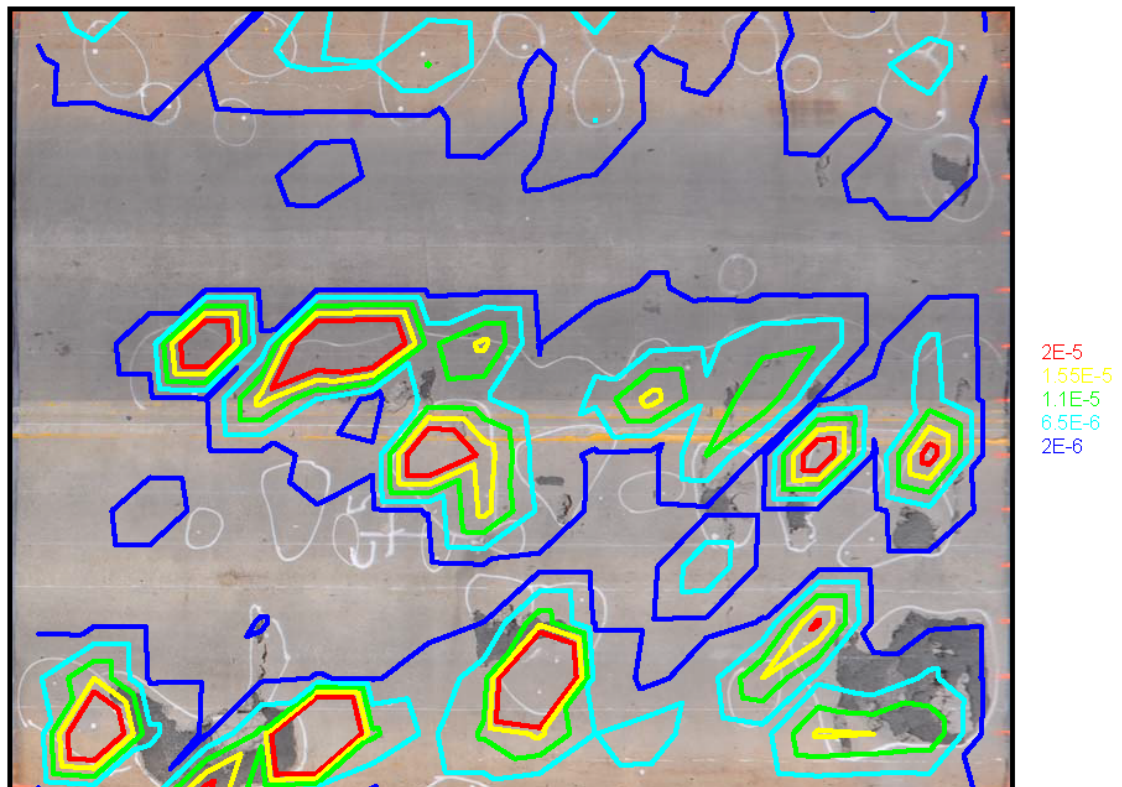


Branchport Bridge; Deck #2  
Peak Mean Ratio

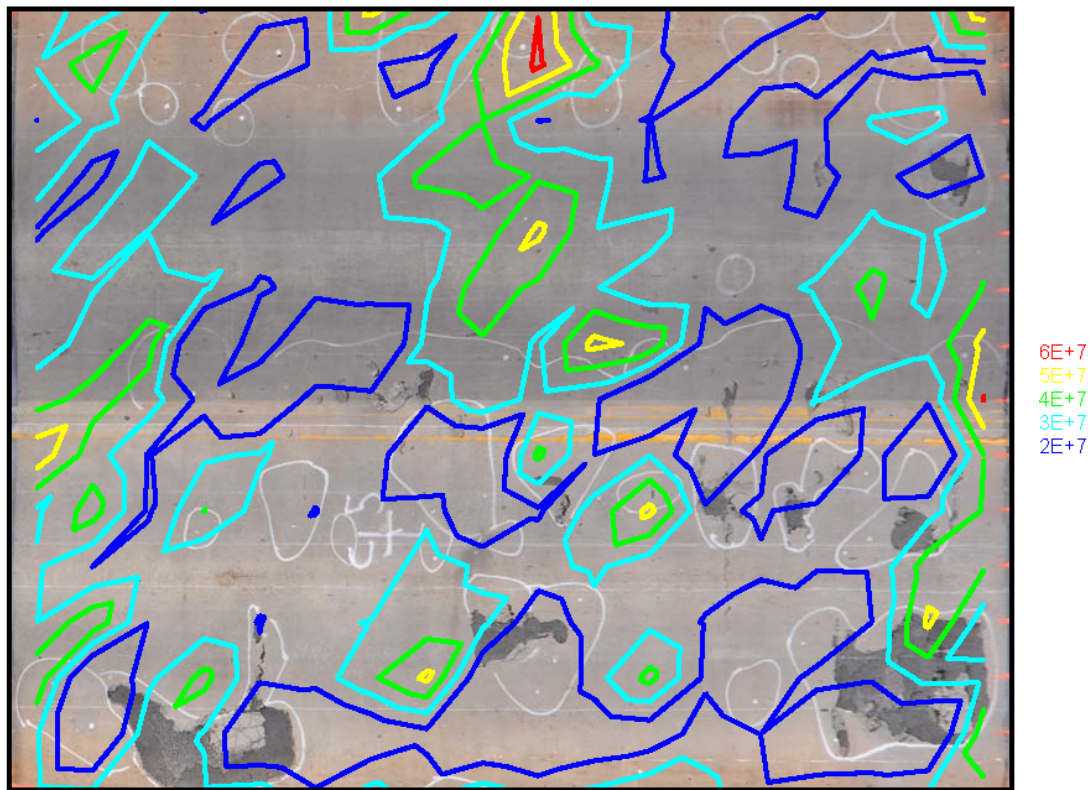


### A.1.3 Deck #3

Branchport Bridge; Deck #3  
Average Mobility ( $(\text{m} \cdot \text{s}^{-1})/\text{N}$ )

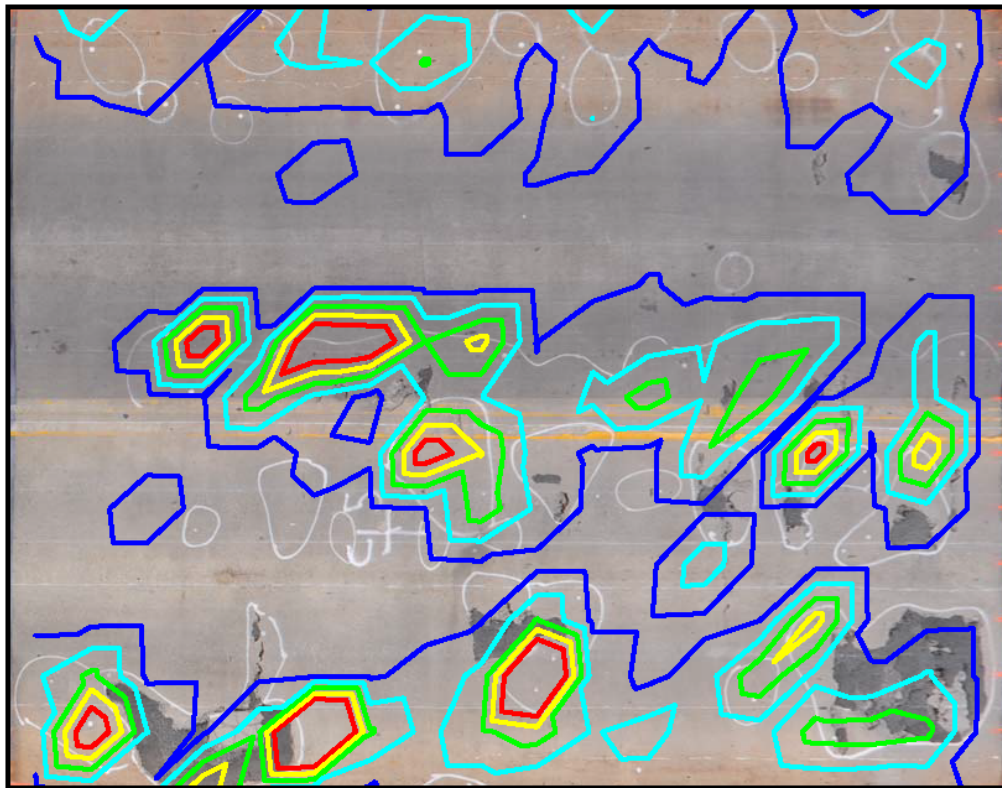


Branchport Bridge; Deck #3  
Dynamic Stiffness (N/m)

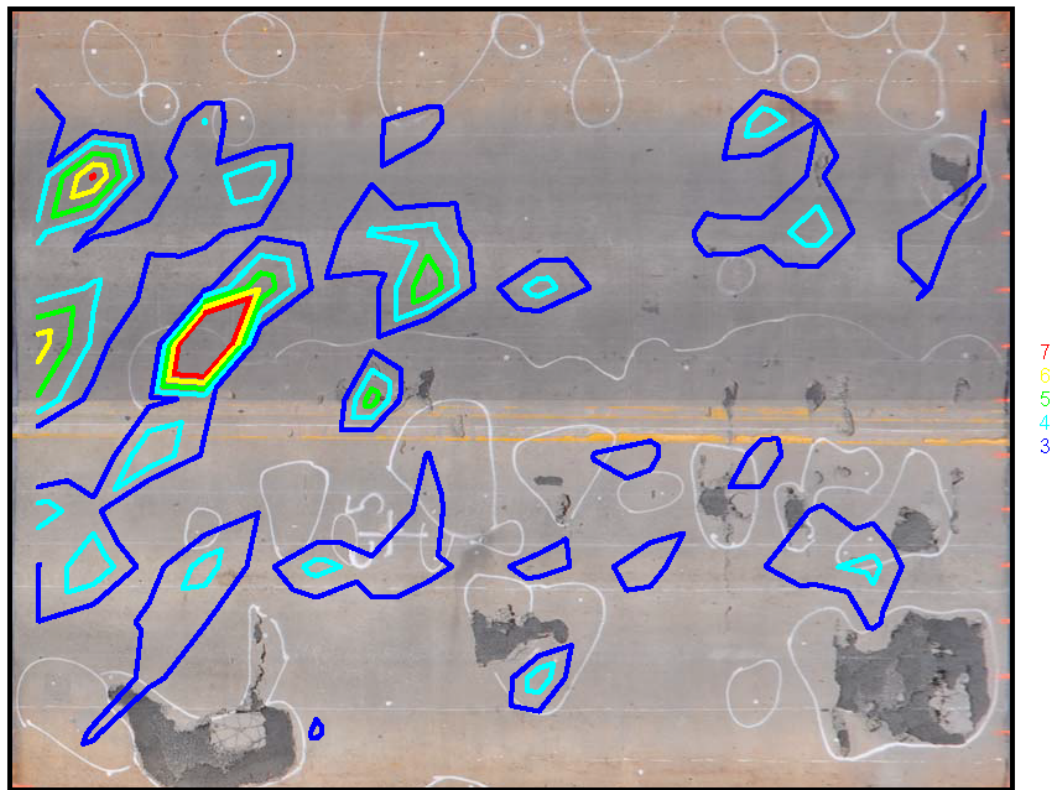




Branchport Bridge; Deck #3  
Mobility Slope (m/N)

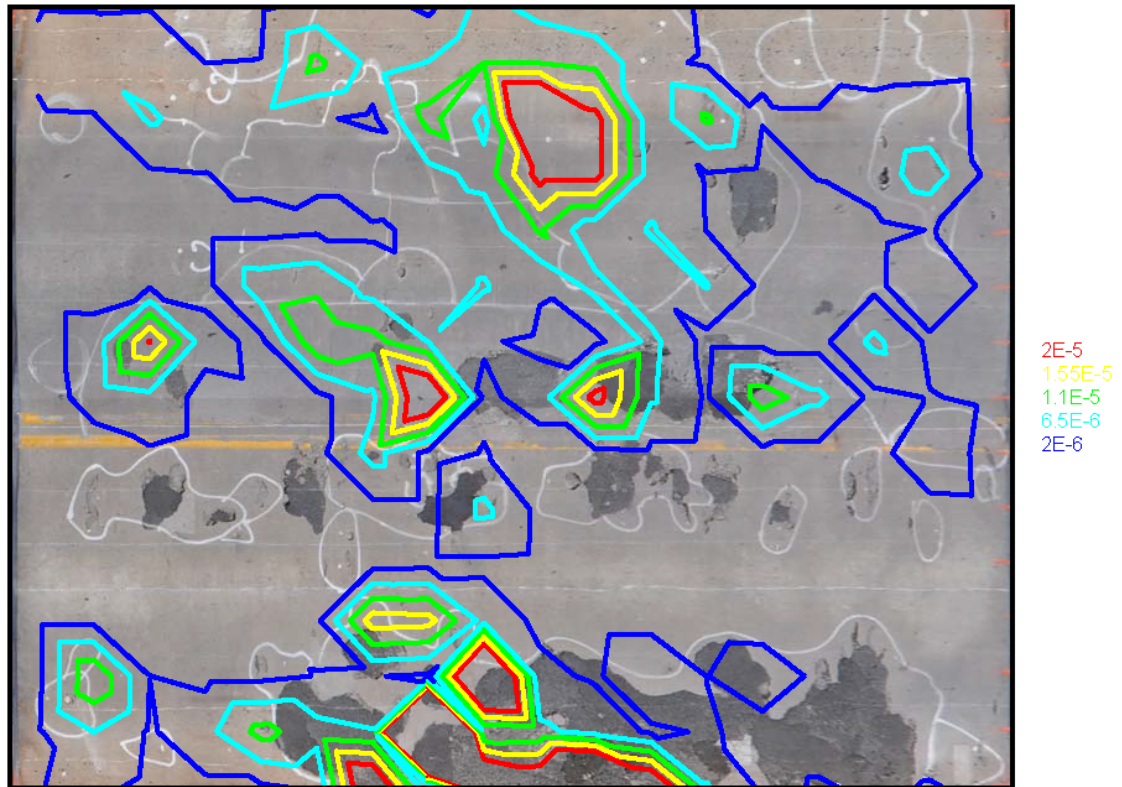


Branchport Bridge; Deck #3  
Peak Mean Ratio

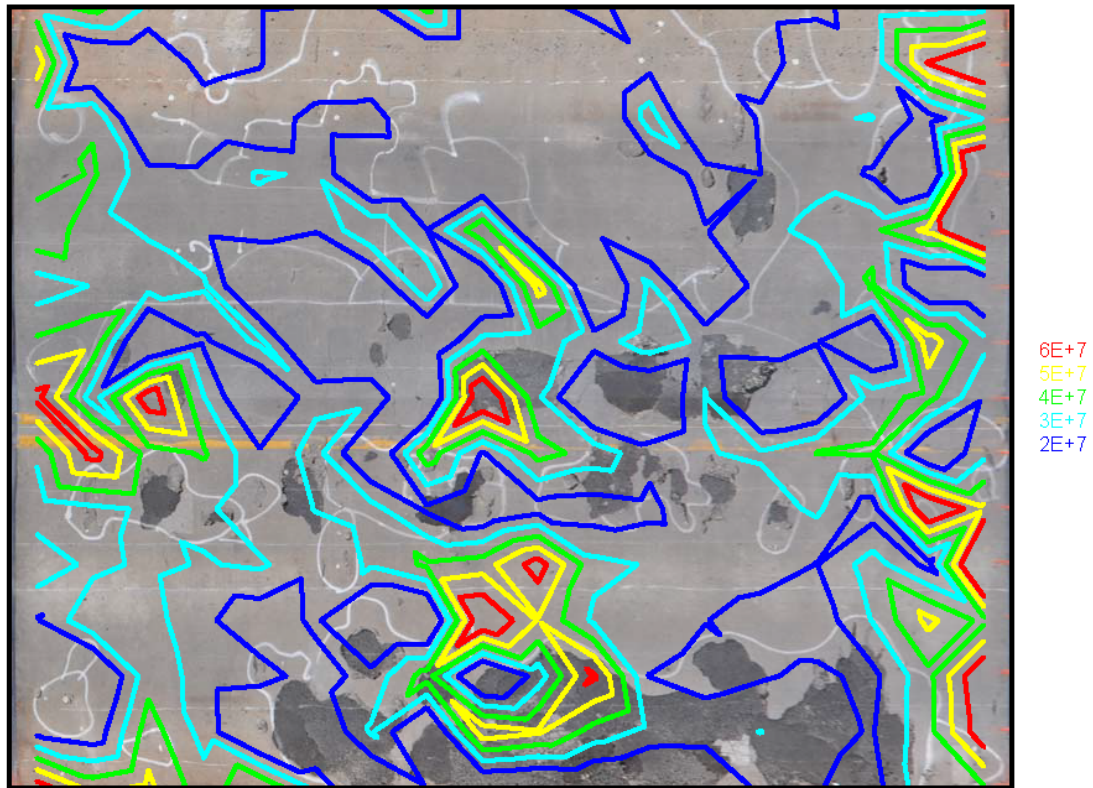


#### A.1.4 Deck #5

Branchport Bridge; Deck #5  
Average Mobility ( $(\text{m} \cdot \text{s}^{-1})/\text{N}$ )

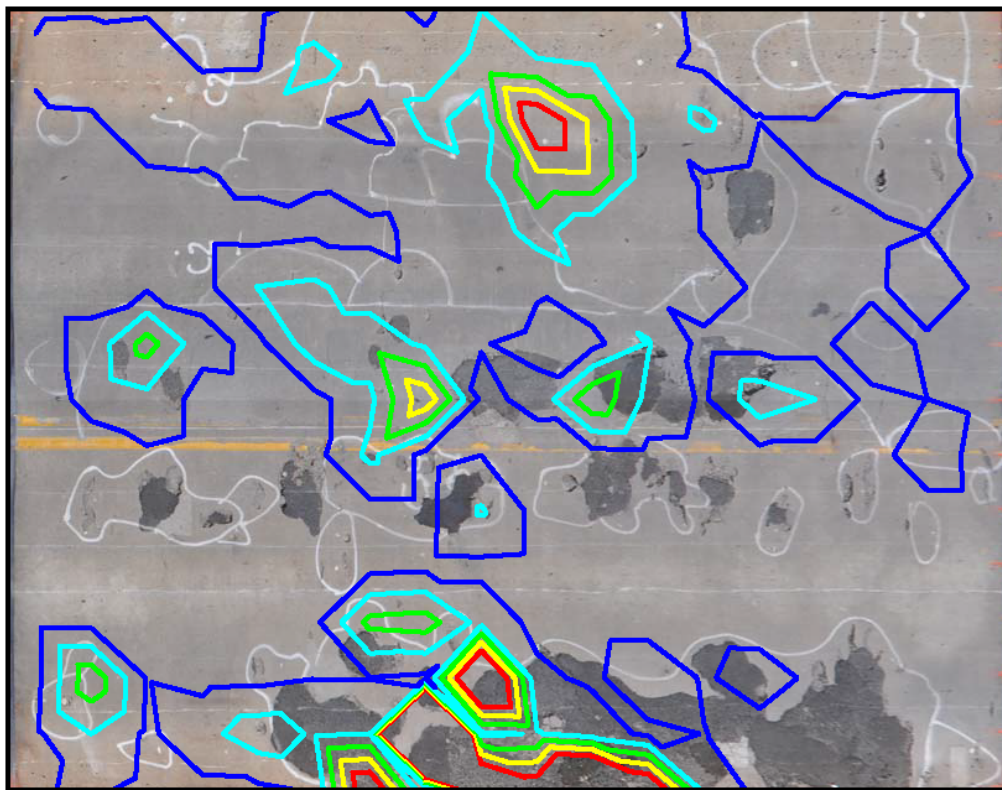


Branchport Bridge; Deck #5  
Dynamic Stiffness (N/m)

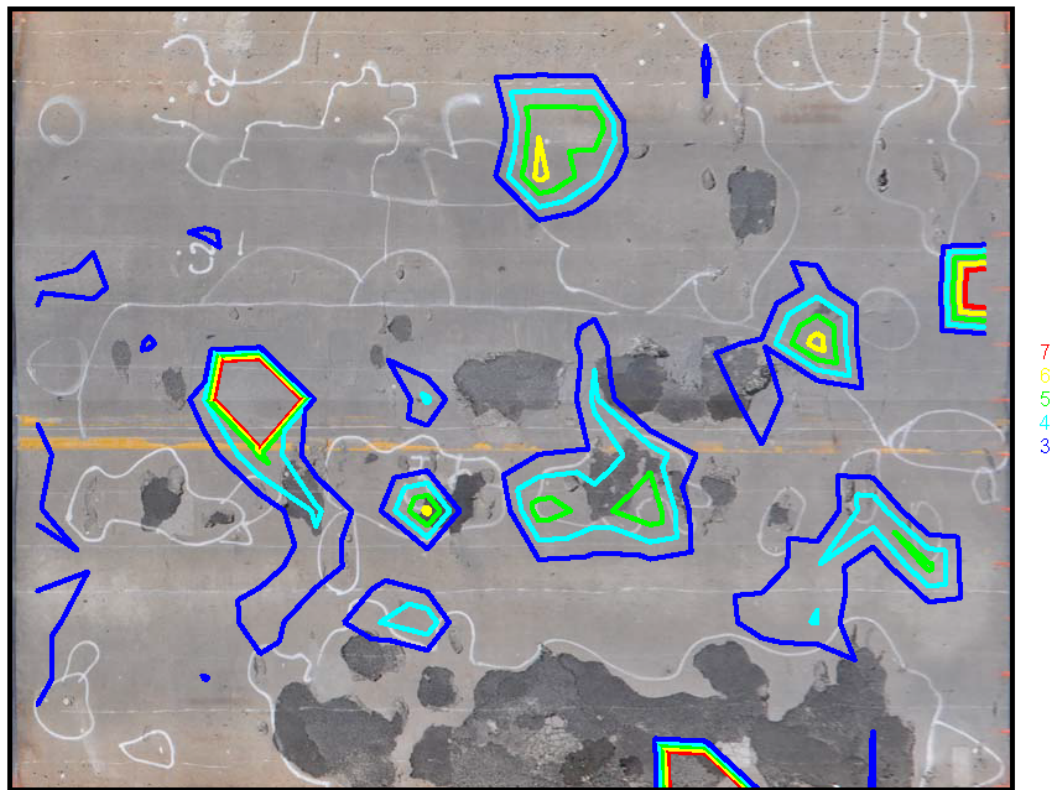




Branchport Bridge; Deck #5  
Mobility Slope (m/N)



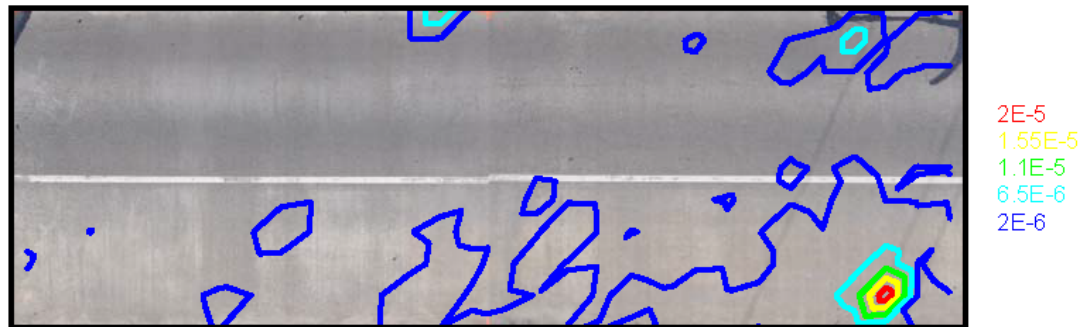
Branchport Bridge; Deck #5  
Peak Mean Ratio



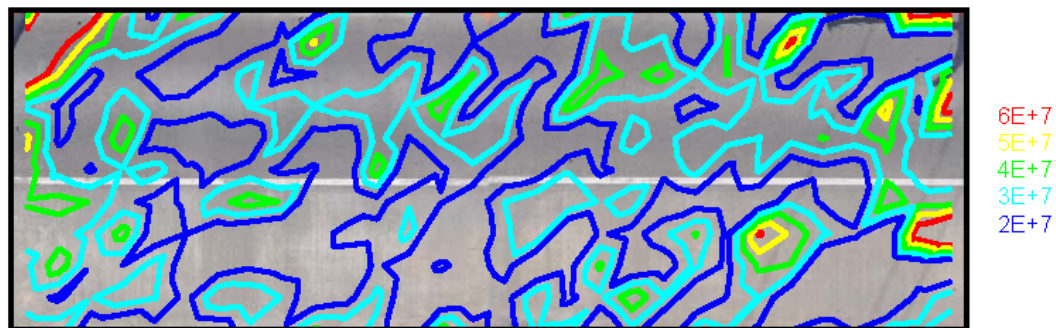
## A.2 Del-DOT Bridge 1-245

### A.2.1 Section #1 (0'-60')

Del-DOT Bridge 1-245; Section #1 (0'-60')  
Average Mobility ((m\*s<sup>-1</sup>)/N)



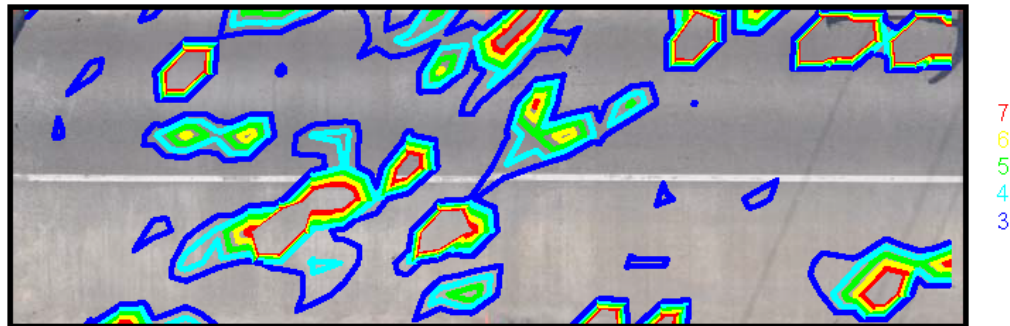
Del-DOT Bridge 1-245; Section #1 (0'-60')  
Dynamic Stiffness (N/m)



Del-DOT Bridge 1-245; Section #1 (0'-60')  
Mobility Slope (m/N)



Del-DOT Bridge 1-245; Section #1 (0'-60')  
Peak Mean Ratio



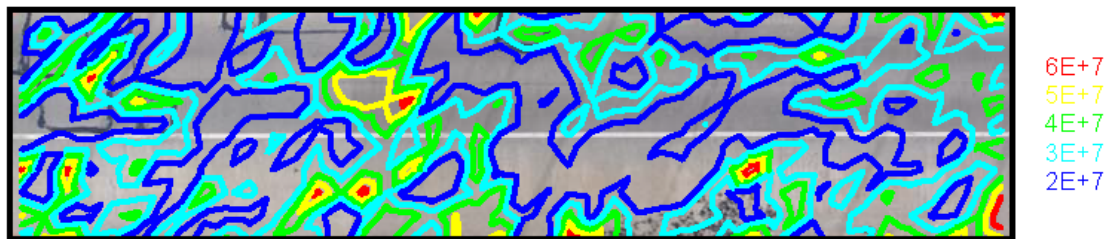


A.2.2 Section #3 (120'-208')

Del-DOT Bridge 1-245; Section #3 (120'-208')  
Average Mobility ( $(\text{m} \cdot \text{s}^{-1})/\text{N}$ )



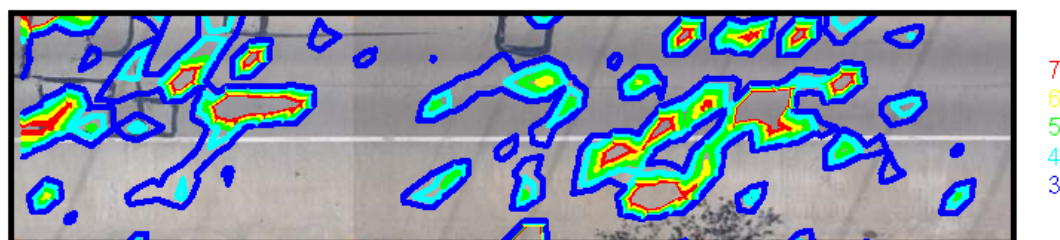
Del-DOT Bridge 1-245; Section #3 (120'-208')  
Dynamic Stiffness (N/m)



Del-DOT Bridge 1-245; Section #3 (120'-208')  
Mobility Slope (m/N)



Del-DOT Bridge 1-245; Section #3 (120'-208')  
Peak Mean Ratio



## Appendix B

### MATLAB SCRIPTS

#### B.1 Impulse Response Scripts

##### B.1.1 Acceleration

```
function [accel,time]=acceleration(filename,block_num,plot_accel)

%inports calibrated accelerations
%filename and block_num must be strings
%block_num must be 2 digits & string
%plot_force plots graph if >1

accel_bin=hdf5read(filename, strcat('/measurements/00000001/channels/0
0000002/blocks/000000',block_num,'/raw'));
%acceleration data set in binary
freq=hdf5read(filename, strcat('/measurements/00000001/channels/000000
02/blocks/000000',block_num),'sampleRateHertz');
%sampling rate
trig=str2double(num2str(hdf5read(filename, strcat('/measurements/00000
001/channels/00000002/blocks/000000',block_num),'triggerSample')));
%sample number at time of trigger
time=linspace(((trig)/freq),((length(accel_bin)-trig-
1)/freq),length(accel_bin));
%data set for time. Calculated by setting each sample to the inverse
of the
%sample rate
bin_volt_f=hdf5read(filename,'/measurements/00000001/channels/0000000
2','binToVoltFactor');
%Binary to volt conversion factor
bin_volt_c=hdf5read(filename,'/measurements/00000001/channels/0000000
2','binToVoltConstant');
%Binary to volt conversion constant
accel_volt=(str2num(num2str(accel_bin))*bin_volt_f)+bin_volt_c;
%converts binary to volts

%accel_avg=mean(accel_volt(round(trig*.5):round(trig*.9)));
%sets initial acceleration to 0
accel_avg=mean(accel_volt(round(trig*.5):round(trig*.9)));
accel=(accel_volt-accel_avg)/.04109;
```

```
%converts acceleration from volts to m/s^2 (.403V/g)*(g*/9.81m/s^2)

if plot_accel>0
    plot(time,accel)
end
end
```

## B.1.2 Force

```
function [force_m,time]=force(filename,block_num,plot_force)

%calibrates force into to volts, and then into newtons
%filename and block_num must be strings
%block_num must be 2 digits
%plot_force plots graph if >1

force_bin=hdf5read(filename, strcat('/measurements/00000001/channels/0
0000001/blocks/000000',block_num,'/raw'));
%force data set in binary
freq=hdf5read(filename, strcat('/measurements/00000001/channels/000000
01/blocks/000000',block_num), 'sampleRateHertz');
%sampling rate
trig=str2double(num2str(hdf5read(filename, strcat('/measurements/00000
001/channels/00000001/blocks/000000',block_num), 'triggerSample')));
%sample number at time of trigger
time=linspace(((trig)/freq), ((length(force_bin)-trig-
1)/freq), length(force_bin));
%data set for time. Calculated by setting each sample to the inverse
of the
%sample rate
bin_volt_f=hdf5read(filename, '/measurements/00000001/channels/0000000
1', 'binToVoltFactor');
%Binary to volt conversion factor
bin_volt_c=hdf5read(filename, '/measurements/00000001/channels/0000000
1', 'binToVoltConstant');
%Binary to volt conversion constant
force_volt=(str2num(num2str(force_bin))*bin_volt_f)+bin_volt_c;
%force in volts
force_avg=mean(force_volt(round(trig*.5):round(trig*.9))); %sets the
force equal to 0 before impact

force_volt=(force_volt-force_avg);
ind=find(force_volt>.1,1, 'first');
if ind==1
    time=NaN;
    force_volt=NaN;
else
    time=time(ind-201:length(time))-time(ind-1);
    force_volt=force_volt(ind-201:length(force_volt));
end

force_m=(force_volt)/.0002431; %converts for into newtons
(.0002431V/N)
```

```
%order_filt=5;  
%[b,a]=butter(order_filt,f_cut_low/(freq/2),'high');  
%force_m=filtfilt(b,a,force_m(:,1));  
  
if plot_force>0  
    plot(time,force_m)  
  
end  
end
```

### B.1.3 Mobility at a Specific Test Point

```
function [Mob,freq]=Mobility(filename,block_num,plot_mob)

%calcs mobility of a given impact
%filename and block_num must be strings
%block_num must be 2 digits
%plot_mob plots graph if >1

[forc]=force(filename,block_num,0);
if length(forc)>1
[accel,time]=acceleration(filename,block_num,0);
    dt=time(2)-time(1);
    %sampling rate
    [~,ind_t]=min(abs(time));
    accel=accel(ind_t-200:min(length(accel),length(forc)+ind_t-201));
    %time=time(ind_t-200:min(length(time),length(forc)+ind_t-201));
    i_cut=min(round(0.2/(dt)),length(forc));
    %time=time(1:i_cut);
    accel=accel(1:i_cut);
    forc=forc(1:i_cut);
vel=cumtrapz(accel(1:length(forc)))*dt;
    %integration of accel to velocity

fs=1/dt;
df=fs/length(vel);
fc=fs/2;
Ncut=floor(fc/df+1);
freq=0:df:(Ncut-1)*df;
%frequncy

Mob=abs(fft(vel))./abs(fft(forc));
Mob=Mob(1:Ncut);

else
    Mob=NaN;
    freq=NaN;
end
if plot_mob>0
    plot(freq,Mob)
    xlim([0 800])
end
end
```

### B.1.4 System Response at Specific Test Point

```
function [mob,time]=mobility_time(filename,block_num,plot_mob)

%Calculates the system response at a specific impact

tm=.00005; %smoothing time, effectively neglects frequencies higher
than 1/tm

[forc]=force(filename,block_num,0);
if length(forc)>1
    %to neglect signals with issues in force recording (branchport)
[accel,time]=acceleration(filename,block_num,0);
    dt=time(2)-time(1);
    [~,ind_t]=min(abs(time));
    accel=accel(ind_t-200:min(length(accel),length(forc)+ind_t-201));
    time=time(ind_t-200:min(length(time),length(forc)+ind_t-201));
    i_cut=min(round(0.2/(dt)),length(forc));
    time=time(1:i_cut);
    accel=accel(1:i_cut);
    forc=forc(1:i_cut);
vel=cumtrapz(accel(1:length(forc)))*dt;

Mob=fft(vel)./fft(forc);
%same as Mobility function, but without the absolute
mob=ifft(Mob);

m=nearest(tm/(time(2)-time(1)));
b=ones(1,m)/m;
mob=filtfilt(b,1,mob);
mob=mob(m:length(vel)-m);
time=time(m:length(vel)-m);
%smoothing

else
    mob=NaN;
    time=NaN;
end
if plot_mob>0
    plot(time,mob)
    xlim([0 0.03])
end
end
```



### B.1.5 Mobility Over the Entire Bridge

```
function
mob_tot=mobility_tot(filename_prefix,number_files,impact_per_loc)
tic
%determines the mobility at each impact on the bridge
%files must be named with "filename_prefix" then the row number
%number_files are the number of rows(files) tested
%impact_per_loc is the number of impacts at each test site
for k=1:number_files
    filename=strcat(filename_prefix,num2str(k),'.tpc5');

    info=hdf5info(filename);

    num_block=length(info.GroupHierarchy.Groups.Groups.Groups(1,1)
    .Groups.Groups);

    for i=1:num_block/impact_per_loc
        for j=1:impact_per_loc
            if (i-1)*impact_per_loc+j<10
                block_num=strcat('0',num2str((i-
1)*impact_per_loc+j));
            else
                block_num=num2str((i-1)*impact_per_loc+j);
            end
            [mob1,freq]=Mobility(filename,block_num,0);
            clearvars mob
            mob(:,1)=mob1;
            mob(:,2)=freq;

            mob_tot.(strcat('row',num2str(k))).(strcat('col',num2str(i))).(strcat
('imp',num2str(j)))=mob;
        end
    end
end
toc
end
```

### B.1.6 System Response Over the Entire Bridge

```
function
mob_tot=mobility_time_tot(filename_prefix,number_files,impact_per_loc
)
tic
%determines the system response at each impact on the bridge
%files must be named with "filename_prefix" then the row number
%number_files are the number of rows(files) tested
%impact_per_loc is the number of impacts at each test site
for k=1:number_files
    filename=strcat(filename_prefix,num2str(k),'.tpc5');

    info=hdf5info(filename);

num_block=length(info.GroupHierarchy.Groups.Groups.Groups(1,1)
.Groups.Groups);

    for i=1:num_block/impact_per_loc
        for j=1:impact_per_loc
            if (i-1)*impact_per_loc+j<10
                block_num=strcat('0',num2str((i-
1)*impact_per_loc+j));
            else
                block_num=num2str((i-1)*impact_per_loc+j);
            end
            [mob1,time1]=mobility_time(filename,block_num,0);
            clearvars mob
            mob(:,1)=mob1;
            mob(:,2)=time1;

mob_tot.(strcat('row',num2str(k))).(strcat('col',num2str(i))).(strcat
('imp',num2str(j)))=mob;
            end
        end
    end
toc
end
```

### B.1.7 Average Mobility

```
function
avg_mob_3d=avgerage_mobility_3d(mobtot,number_files,impact_per_loc,spacing)
%creates a matrix with x,y,avagemobility for impact 1,impact
%2,...,average of all impacts)
%mobility_tot function must be run before this.
%mobtot is the structure created from mobility_tot function
%spacing is the spacing between test points.
k=1;
avg_mob_3d=zeros(number_files*length(fieldnames(mobtot.(strcat('row',
num2str(1))))),impact_per_loc+3);
for i=1:number_files
    for j=1:length(fieldnames(mobtot.(strcat('row',num2str(i))))
        avg_mob_3d(k,2)=-i*spacing;
        avg_mob_3d(k,1)=j*spacing;
        for q=1:impact_per_loc

mobatot=mobtot.(strcat('row',num2str(i))).(strcat('col',num2str(j))).
(strcat('imp',num2str(q)))(:,1);

f=mobtot.(strcat('row',num2str(i))).(strcat('col',num2str(j))).(strcat('imp',num2str(q)))(:,2);

            if length(f)>1
                df=f(2)-f(1);
                i_100Hz=nearest(100/df)+1;
                i_800Hz=nearest(800/df)+1;

                am=mean(mobatot(i_100Hz:i_800Hz));

            else
                am=NaN;
            end

            avg_mob_3d(k,q+2)=am;
        end
    end
    avg_mob_3d(k,impact_per_loc+3)=nanmean(avg_mob_3d(k,3:impact_per_loc+
2));
    k=k+1;
end
end
end
```

### B.1.8 Dynamic Stiffness

```
function
d_stiff_3d=d_stiffness_3d(mobtot,number_files,impact_per_loc,spacing)
%creates a matrix with x,y,dynamicstiffness for impact 1,impact
%2,...,average of all impacts)
%mobility_tot function must be run before this.
%mobtot is the structure created from mobility_tot function
%spacing is the spacing between test points.
k=1;
d_stiff_3d=zeros(number_files*length(fieldnames(mobtot.(strcat('row',
num2str(1))))),impact_per_loc+3);
for i=1:number_files
    for j=1:length(fieldnames(mobtot.(strcat('row',num2str(i))))
        d_stiff_3d(k,2)=-i*spacing;
        d_stiff_3d(k,1)=j*spacing;
        for q=1:impact_per_loc

mobatot=mobtot.(strcat('row',num2str(i))).(strcat('col',num2str(j))).
(strcat('imp',num2str(q)))(:,1);

f=mobtot.(strcat('row',num2str(i))).(strcat('col',num2str(j))).(strca
t('imp',num2str(q)))(:,2);

            if length(f)>1
                df=f(2)-f(1);
                i_10Hz=nearest(10/df)+1;
                i_40Hz=nearest(40/df)+1;

                x=f(i_10Hz:i_40Hz);
                y=mobatot(i_10Hz:i_40Hz);

                if length(x)>2

s=fitoptions('Method','LinearLeastSquares','Lower',[-
Inf,0],'Upper',[Inf,0]);
                dkcoeff=coeffvalues(fit(x,y,'poly1',s));
                d_stiff=1/dkcoeff(1);
            else
                d_stiff=NaN;
            end
        else
            d_stiff=NaN;
        end

        d_stiff_3d(k,q+2)=d_stiff;
    end
end
```

```
d_stiff_3d(k,impact_per_loc+3)=nanmean(d_stiff_3d(k,3:impact_per_loc+
2));
    k=k+1;
end
end
end
```

### B.1.9 Mobility Slope

```
function
mob_slo_3d=mob_slope_3d(mobtot,number_files,impact_per_loc,spacing)
%creates a matrix with x,y,mobilityslope for impact 1,impact
%2,...,average of all impacts)
%mobility_tot function must be run before this.
%mobtot is the structure created from mobility_tot function
%spacing is the spacing between test points.
k=1;
mob_slo_3d=zeros(number_files*length(fieldnames(mobtot.(strcat('row',
num2str(1))))),impact_per_loc+3);
for i=1:number_files
    for j=1:length(fieldnames(mobtot.(strcat('row',num2str(i))))
        mob_slo_3d(k,2)=-i*spacing;
        mob_slo_3d(k,1)=j*spacing;
        for q=1:impact_per_loc

mobatot=mobtot.(strcat('row',num2str(i))).(strcat('col',num2str(j))).
(strcat('imp',num2str(q)))(:,1);

f=mobtot.(strcat('row',num2str(i))).(strcat('col',num2str(j))).(strca
t('imp',num2str(q)))(:,2);

            if length(f)>1
                df=f(2)-f(1);
                i_100Hz=nearest(100/df)+1;
                i_800Hz=nearest(800/df)+1;

                x=f(i_100Hz:i_800Hz);
                y=mobatot(i_100Hz:i_800Hz);

                s=fitoptions('Method','LinearLeastSquares','Lower',[-
Inf,0],'Upper',[Inf,0]);
                mscoeff=coeffvalues(fit(x,y,'poly1',s));
                ms=mscoeff(1);
            else
                ms=NaN;
            end

            mob_slo_3d(k,q+2)=ms;
        end

mob_slo_3d(k,impact_per_loc+3)=nanmean(mob_slo_3d(k,3:impact_per_loc+
2));
        k=k+1;
    end
end end
```

### B.1.10 Peak Mean Mobility

```
function
pea_mea_3d=peak_mean_3d(mobtot,number_files,impact_per_loc,spacing)
%creates a matrix with x,y,peak_mean for impact 1,impact
%2,...,average of all impacts)
%mobility_tot function must be run before this.
%mobtot is the structure created from mobility_tot function
%spacing is the spacing between test points.
k=1;
pea_mea_3d=zeros(number_files*length(fieldnames(mobtot.(strcat('row',
num2str(1))))),impact_per_loc+3);
for i=1:number_files
    for j=1:length(fieldnames(mobtot.(strcat('row',num2str(i))))
        pea_mea_3d(k,2)=-i*spacing;
        pea_mea_3d(k,1)=j*spacing;
        for q=1:impact_per_loc

mobatot=mobtot.(strcat('row',num2str(i))).(strcat('col',num2str(j))).
(strcat('imp',num2str(q)))(:,1);

f=mobtot.(strcat('row',num2str(i))).(strcat('col',num2str(j))).(strca
t('imp',num2str(q)))(:,2);

            if length(f)>1
                df=f(2)-f(1);
                i_10Hz=nearest(10/df)+1;
                i_100Hz=nearest(100/df)+1;
                i_800Hz=nearest(800/df)+1;

                am=mean(mobatot(i_100Hz:i_800Hz));
                peak=max(abs(mobatot(i_10Hz:i_100Hz)));
                pea_mea=peak/am;

            else
                pea_mea=NaN;
            end

            pea_mea_3d(k,q+2)=pea_mea;
        end

pea_mea_3d(k,impact_per_loc+3)=nanmean(pea_mea_3d(k,3:impact_per_loc+
2));
        k=k+1;
    end
end
end
```

### B.1.11 Maximum System Response

```
function max3d=max_3d(mobtot,number_files,impact_per_loc,spacing)
%creates a matrix with x,y,maxresponse for impact 1,impact
%2,...,average of all impacts)
%mobility_tot_time function must be run before this.
%mobtot is the structure created from mobility_tot_time function
%spacing is the spacing between test points.
k=1;
exp3d=zeros(number_files*length(fieldnames(mobtot.(strcat('row',num2s
tr(1))))),impact_per_loc+3);
for i=1:number_files
    for j=1:length(fieldnames(mobtot.(strcat('row',num2str(i))))))
        max3d(k,2)=-i*spacing;
        max3d(k,1)=j*spacing;
        for q=1:impact_per_loc

mobatot=mobtot.(strcat('row',num2str(i))).(strcat('col',num2str(j))).
(strcat('imp',num2str(q)))(:,1);

t=mobtot.(strcat('row',num2str(i))).(strcat('col',num2str(j))).(strca
t('imp',num2str(q)))(:,2);

            if length(t)>1
                mx=max(abs(mobatot));
            else
                mx=NaN;
            end

            max3d(k,q+2)=mx;
        end
    end
    max3d(k,impact_per_loc+3)=nanmean(max3d(k,3:impact_per_loc+2));
    k=k+1;
end
end
end
```



### B.1.12 Peak Finder

```
function [peak,mob,time]=peakfinder(mob,time,plot_peak)
%finds peaks in the time domain

if length(mob)>1
tw=.0001; %windowing span; frequencies above 1/tw effectively
neglected
w=nearest(tw/(time(2)-time(1)));
k=1;
mob_max=0;

for i=0:floor(length(mob)/w-1);
    if abs(mob_max)<max(abs(mob(w*i+1:w*(i+1))))
        [mob_max,i_mobmax]=max(abs(mob(w*i+1:w*(i+1))));
        peak(k,1)=time(i*w+i_mobmax);
        peak(k,2)=mob(i*w+i_mobmax);
    else
        [mob_max,i_mobmax]=max(abs(mob(w*i+1:w*(i+1))));
        if abs(peak(k,1))>0
            k=k+1;
            peak(k,1:2)=0;
        end
    end
end
else
    mob=NaN;
    time=NaN;
end
if plot_peak>0
    plot(peak(:,1),peak(:,2),'*r',time,mob)
end
end
```

### B.1.13 System Response Damping

```
function exp3d=exp_3d(mobtot,number_files,impact_per_loc,spacing)
%creates a matrix with x,y,maxresponse for impact 1,impact
%2,...,average of all impacts)
%mobility_tot_time function must be run before this.
%mobtot is the structure created from mobility_tot_time function
%spacing is the spacing between test points.
k=1;
exp3d=zeros(number_files*length(fieldnames(mobtot.(strcat('row',num2s
tr(1))))),impact_per_loc+3);
for i=1:number_files
    for j=1:length(fieldnames(mobtot.(strcat('row',num2str(i))))
        exp3d(k,2)=-i*spacing;
        exp3d(k,1)=j*spacing;
        for q=1:impact_per_loc

mobatot=mobtot.(strcat('row',num2str(i))).(strcat('col',num2str(j))).
(strcat('imp',num2str(q)))(:,1);

t=mobtot.(strcat('row',num2str(i))).(strcat('col',num2str(j))).(strca
t('imp',num2str(q)))(:,2);

            if length(t)>1
                [peak,~,~]=peakfinder(mobatot,t,0);

expb=fit(peak(1:min(50,length(peak(:,1)))),1),abs(peak(1:min(50,length
(peak(:,1))),2)), 'exp1');
                expr=coeffvalues(expb);

            else
                expr(2)=NaN;
            end

            exp3d(k,q+2)=expr(2);
        end

exp3d(k,impact_per_loc+3)=nanmean(exp3d(k,3:impact_per_loc+2));
        k=k+1;
    end
end
end
```

## B.2 Ground-Penetrating Radar Scripts

### B.2.1 Data Extraction

```
function data=extract(filename)

%extracts data from file to vector

fid=fopen(filename);
hm=textscan(fid,'%s');
fclose('all');

n=(length(hm{1})-73)/769;
data=zeros(512,n);

for j=1:n

    for i=1:2:511
        data(i,j)=hex2dec(strcat(hm{1}{(j-
1)*769+73.5+i*1.5}(1),hm{1}{(j-1)*769+74.5+i*1.5}));
        data(i+1,j)=hex2dec(strcat(hm{1}{(j-
1)*769+73.5+i*1.5}(2),hm{1}{(j-1)*769+75.5+i*1.5}));
    end
end
```

### B.2.2 Attenuation

```
function attn=atten(data,mag)
%Linear attenuation correction
sz=size(data);
len=sz(2);
f=1:(mag-1)/512:mag-(mag-1)/512;
attn=zeros(512,len);
for i=1:len
    attn(:,i)=data(:,i).*f';
end
end
```

### B.2.3 Cross-correlation Algorithm

```
function focus=focusingf(data)
%cross-correlation function
s=12;
t=-256:256;
r=(2/(sqrt(3*s)*pi^(1/4)))*(1-t.^2/s^2).*exp(-t.^2/(2*s^2));
dr=diff(r)./diff(t);
focus=zeros(1,512);

for j=1:length(data(1,:))
    avg(j,:)=data(:,j)';
    %    avgcut(j-2,:)=avg(j-2,:);
    %    avgcut(j-2,1:120)=0;
    clearvars avgrepl;
    %    avgrepl(1,:)=avgcut(j-2,:);
    avgrepl(1,:)=avg(j,:);

    for i=1:10
        clearvars repl cross xpeak i_xpeak peak i_peak sn;
        cross=xcorr(avgrepl(i,:),dr);
        cross=cross(512-256:512*2-257);
        [xpeak,i_xpeak]=max(abs(cross));
        [peak,i_peak]=max(abs(avgrepl(i,max(2,i_xpeak-
55):min(56+i_xpeak,512)))));
        sn=(55-i_peak)/abs((55-i_peak));
        focus(j,i_peak+max(i_xpeak-56,0))=avg(j,i_peak+max(i_xpeak-
56,0));
        repl=sn*dr(256-(i_xpeak-max(2,i_xpeak-
55)):(256+min(512,i_xpeak+56))-i_xpeak)*max(avgrepl(i,256-(i_xpeak-
max(2,i_xpeak-55)):(256+min(512,i_xpeak+56))-i_xpeak))/max(dr(256-
(i_xpeak-max(2,i_xpeak-55)):(256+min(512,i_xpeak+56))-i_xpeak));
        avgrepl(i+1,:)=avgrepl(i,:);
        avgrepl(i+1,max(2,i_xpeak-
55):min(56+i_xpeak,512))=avgrepl(i,max(2,i_xpeak-
55):min(56+i_xpeak,512))-repl;
    end
end
surf(0:2.5:(length(data(1,:))-1)*2.5,0:1/64:511/64,focus')
end
```

## B.2.4 Migration Algorithm

```
function [SAFT1,num,G]=SAFT(data,x_s,t_r,er,do)
%Migration algorithm
%x_s is spacing between a scans (.0025 for wide settings, .005 for
normal)
%t_r is spacing between transducer and reciever (.04)
%er is dielectric concstant
%do is offset from surface to bottom of sensor
x=x_s:x_s:x_s*length(data(1,:,1));
t_s=1/64;
t=(t_s:t_s:t_s*length(data(:,1,1)))';
v=.3/(er)^(1/2);
y=t*v;
y_s=t_s*v;

SAFT1=zeros(length(y),length(x));
num=zeros(length(y),length(x));
for i=1:length(x)
    send=x(i)-t_r/2;
    rec=x(i)+t_r/2;
    for ii=max(1,i-
round(max(t)*v/(2*x_s))):min(length(x),i+round(max(t)*v/(2*x_s)))
        for j=1:length(y)
            d=((ii*x_s)-send)^2+(j*y_s)^2)^(1/2)+(((ii*x_s)-
rec)^2+(j*y_s)^2)^(1/2);
            d_i=round((d/v-2*do/.3)/t_s);
            if d_i<length(y)
                SAFT1(j,ii)=SAFT1(j,ii)+(sum(data(d_i,i,1)));
                %SAFT1(j,ii)=SAFT1(j,ii)+(sum(data(d_i,i,1))-129);
                num(j,ii)=num(j,ii)+1;
            end
        end
    end
end
G=SAFT1./num;
figure1 = figure;
colormap('gray');

% Create axes
axes1 = axes('Parent',figure1);
grid(axes1,'on');
hold(axes1,'all');

% Create surf
surf(x*1000,y*1000,G,'parent',axes1,'EdgeColor','none')
```

## Appendix C

### PERMISSION LETTER FOR FIGURE 1.1

1/25/13

Gmail - Picture Approval



Daniel Clem <daniel.j.clem@gmail.com>

---

#### Picture Approval

2 messages

---

**Daniel Clem** <clemd@udel.edu>  
To: Ralf Amdt <ralf.w.amdt@gmail.com>

Thu, Jan 24, 2013 at 11:09 AM

Ralf,

I hope all is well in South Florida!

I am finally seeing the light at the end of the tunnel on my thesis. Thomas has given me a photo to use in my thesis that he has from your "Strategies for maintenance of highway bridges in the US." paper the two of you worked on together (see attached). It turns out that in order to use this picture, I need authorization from the owner of the photo. I was wondering if you remember who took this photo? Any help would be appreciated!

Thanks,

Daniel Clem  
Graduate Student  
University of Delaware  
CMI and Environmental Engineering  
DuPont Hall 314



**Picture3.tif**  
432K

---

**Ralf Amdt** <ralf.w.amdt@gmail.com>  
To: Daniel Clem <clemd@udel.edu>

Thu, Jan 24, 2013 at 3:06 PM

Dan,

everything is good!

The photo I made myself with my camera. You can have it.

Good luck!  
Ralf